INVESTIGATION OF THE RELATIONSHIPS BETWEEN SUPERCONDUCTING PROPERTIES AND Nb_3Sn REACTION CONDITIONS IN POWDER-IN-TUBE NB_3SN CONDUCTORS

by

CHAD MATTHEW FISCHER

A thesis submitted in partial fulfillment

of the requirements for the degree of

Master of Science

(Materials Science)

University of Wisconsin-Madison

2002

ACKNOWLEDGEMENTS

I have numerous people to thank for making my time at the Applied Superconductivity Center a pleasant and productive one. First off, I would like to express a great deal of thanks to my advisor, David Larbalestier, for his guidance and support of this thesis work, along with his cheerful personality, which made for a comfortable work environment. I am deeply indebted to Peter Lee for the countless hours of state of the art microscopy he has provided towards this work. I would also like to express a big thanks to Bill Starch for lending a great deal of ingenuity to my sample preparation and for keeping order in the fabrication facility. I am very appreciative of Alex Squitieri for maintaining the SQUID and VSM equipment and for providing assistance during my numerous bouts with misbehaving computers. I would like to extend my gratitude to Lance Cooley for offering his many insights concerning my research. My time at ASC would have been significantly different were it not for Mike Naus, who not only helped make Room 602 an enjoyable place to work, but also served as a true graduate student mentor, and for this I thank him. I must also extend thanks to Matt Jewell for his discussions and good cheer. Many thanks to Jan Lindenhovius of ShapeMetal Innovation, Holland, for donating the wire that served as the basis for this study. Lastly, I would like to thank my roommates Cal, Dave and Jack and my family for being supportive throughout my graduate years.

CONTENTS

1 Introduction

1.1 Motivation

A strong demand exists for high-field superconductor understanding and development in order to facilitate construction of next-generation accelerator magnets. The Very Large Hadron Collider (VLHC), scheduled for operation in 2015, is the present driving force for high-field accelerator superconductivity applications. Several magnet designs for this system require fields in excess of 12 T [1].

NbTi has been the workhorse material for accelerator magnets of the past two decades, serving as the conductor for the Tevatron [2], HERA [3] and most recently the Large Hadron Collider (LHC) [4]. NbTi's benefits are its low cost, reproducible critical current densities (J_c), long piece lengths and ductility. However, the conductor is best suited for performing at lower fields, on the order of 5 to 7 T at 4.2 K. For the LHC, NbTi supplies 8.3 T of field, however the operating temperature of the system had to be reduced to 1.9 K to achieve this. From earlier research, much of it at UW-ASC, it became clear that NbTi had reached its J_c limit at high fields, and that higher field magnets, such as those to be utilized in the VLHC, would require a new superconductor of choice [5].

The best conductor option for high field magnets is Nb_3Sn, whose upper critical field (30 T) and critical temperature (18.3 K) values are nearly double those achieved in NbTi; 15.4 T [6] and 9.3 K, respectively. Despite having superior primary superconducting properties (T_c and H_{c2}), Nb_3Sn's higher cost and significant strain sensitivity are the primary reasons as to why the material received limited industrial exposure since its discovery in 1960.

It is a goal of the superconductor community to improve the cost-effectiveness and design flexibility of Nb_3Sn. One way to reduce its cost per kA-m is to improve its J_c. To aid this goal, High Energy Physics (HEP) established a goal in 1999 of achieving 3,000 A/mm² (12 T, 4.2 K) [1], measured in the package required to permit the Nb_3Sn A15 phase formation. At the outset of this work, J_c values of ~2,000 A/mm² had been achieved in relatively inhomogenous conductor designs which did not permit an easy understanding of the local J_c within only the A15 component of the conductor. At the time of this writing (2002), Nb_3Sn conductors have now achieved J_c (12 T, 4.2 K) values as high as 2,900 A/mm² [7], although in conductors which still remain much less understood than NbTi. The motivation behind this research is to obtain a clearer understanding of the relation between Nb_3Sn superconducting properties and the governing microstructure using a specific design of conductor, powder-in-tube (PIT), which has recently been effectively optimized by the Dutch company SMI (ShapeMetal Innovation).

1.2 Superconductivity Principles

In 1911, Kamerlingh Onnes discovered an interesting property of mercury, namely that its electrical resistance fell sharply at approximately 4 K and below this temperature was immeasurable. Onnes recognized that he had come across a previously undiscovered material state, and termed his new state the "superconducting state." The temperature at which this phenomenon occurs is the critical temperature (T_c), and is one of the three critical properties of superconducting materials.

Twenty-two years later in 1933 Meissner and Ochsenfeld made the second major discovery in superconductivity. They discovered that materials in the superconducting state

exclude magnetic flux from their interior, exhibiting perfect diamagnetism under certain conditions. Prior to this discovery, it was known, through principles of electromagnetism, that for a resistanceless material, a magnetic field applied above T_c would be excluded when the material was cooled below T_c (provided that the field did not exceed a critical value). However, superconductors were found to be more than just perfect conductors. Magnetic field is excluded from a superconductor independent of whether an applied field is present in the material prior to it being cooled below the transition temperature. This difference between a merely resistanceless, perfect conductor and a superconductor is depicted in Figure 1.1. The property of magnetic flux exclusion in the presence of a magnetic field is called the Meissner effect.

A superconductor is able to exclude magnetic field by developing shielding currents at the surface of the conductor. The currents flow in a direction such that they create an opposing magnetic field that cancels the applied field in the superconductor. Naturally, these shielding currents are not confined entirely to the surface, since the resulting current density would be infinite. The currents flow within a very thin surface layer, on the order of 100 nm, depending on the superconducting material. The depth of this surface layer is known as the penetration depth (λ).

As the applied magnetic field is increased, the shielding currents increase to maintain perfect diamagnetism up to a limit defined by the depairing current density (J_d), at which the energy imparted to the supercurrent equals the energy gap of the superconducting state. The applied field at which superconductivity is destroyed in type-I superconductors (the class of superconductivity described up to this point) is known as the critical field (H_c).

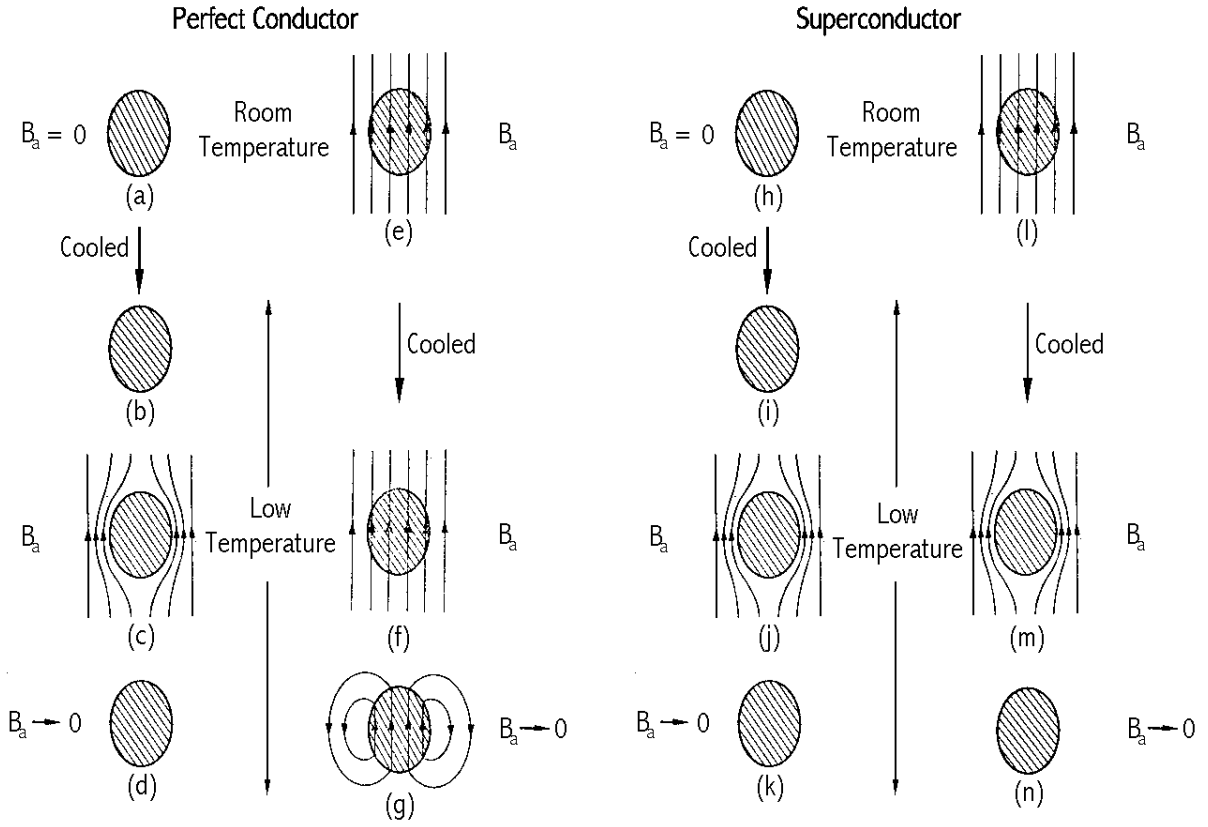

Figure 1.1. Comparison of the magnetic behavior of a perfect conductor and a superconductor. For both the perfect conductor (a, b, c and d) and the superconductor (h, i, j and k) magnetic flux exclusion occurs when the materials are first cooled and then exposed to a magnetic field. When the materials are exposed to a magnetic field and then cooled, the perfect conductor traps the magnetic flux (e, f and g), while the superconductor excludes the magnetic flux (l, m and n) [8].

Understanding of the details of how magnetic fields penetrate superconductors, particularly alloyed superconductors and compounds, developed very slowly from about 1930 to 1960. Shubnikov performed the first experiments revealing properties of the second class of superconductors (type-II) in the mid 1930s, but the significance of his experiment was not generally appreciated. Some 20 years later Abrikosov wrote a theoretical paper proposing flux quantizaton in very high critical field materials. However, Goodman was the first to link Abrikosov's theory with previously observed high magnetic field properties of superconductors such as Mo_3Re, Nb_3Sn and NbZr. Finally, Kunzler et al. [9] showed in

1961 that Nb_3Sn could sustain critical current densities (J_c) exceeding 10^3 A/mm² even in fields of 8.8 T. It all became suddenly clear that a second class of superconductor with an upper critical field (H_{c2}) much higher than H_c existed. For this reason, most of the superconducting materials used in engineering applications today exhibit type-II superconductivity.

In both type-I and type-II superconductors, the free energy per unit volume in the normal region is higher than that in the superconducting region. The surface energy (E_s) between the normal and superconducting regions is approximately defined as

$$E_s = \frac{1}{2}\mu_0 H_c^2(\xi - \lambda), \tag{1.1}$$

where ξ is the coherence length over which the superconducting order parameter decays. ξ is effectively the thickness of the boundary between the two regions. Thus, a positive or negative E_s is dependent on the relative magnitudes of ξ and λ. In type-I superconductivity, the Ginzberg-Landau parameter $\kappa = \lambda/\xi < 1/\sqrt{2}$ and there is a positive surface energy at the boundary between normal and superconducting regions, making it thermodynamically unfavorable for a type-I superconductor to allow normal regions within superconducting regions when the applied field is lower than H_c. In type-II superconductors, $\lambda/\xi > 1/\sqrt{2}$ and there is a negative surface energy associated with the boundary between normal and superconducting regions. Therefore, when the increase in free energy due to the bulk of the normal region is outweighed by the decrease in free energy due to the surface of the region, it becomes thermodynamically favorable for normal regions to develop within superconducting regions. This is known as mixed-state superconductivity and occurs at an applied field H_{c1}.

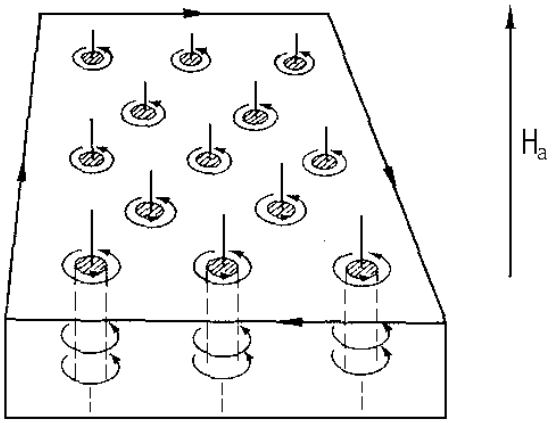

Figure 1.2. Mixed-state superconductivity found in type-II superconductors. Normal cores are penetrated by magnetic flux and encircled by supercurrent vortices. Surface current opposes the applied magnetic field [8].

Mixed-state superconductivity is depicted in Figure 1.2. As in type-I superconductivity, a shielding current opposes the applied magnetic field. Within the superconducting material exist normal cores, of radius ξ. Each core is penetrated by a quantum of magnetic flux, called a fluxon, having the same direction as that of the applied magnetic field and a value of $\phi_0 = hc/2e \sim 2.07 \text{ X } 10^{-15}$ Wb. The fluxon is generated by a vortex of supercurrent, of radius λ, circulating in a direction opposite that of the shielding current. The fluxons repel one another and arrange themselves in a close-packed hexagonal array called a flux line lattice. As the applied magnetic field increases, more and more fluxons of fixed magnetic field penetrate the superconductor. The upper critical field (H_{c2}) occurs in type-II superconductors when the cores of magnetic flux overlap. H-T phase diagrams of the two types of superconductors are compared in Figure 1.3.

In Figure 1.4, the magnetization curves for ideal type-I and type-II superconductors are compared. In type-I superconductivity, perfect diamagnetism exists for fields lower than H_c where the magnetization is equal in magnitude to the applied field. Above H_c, full-flux

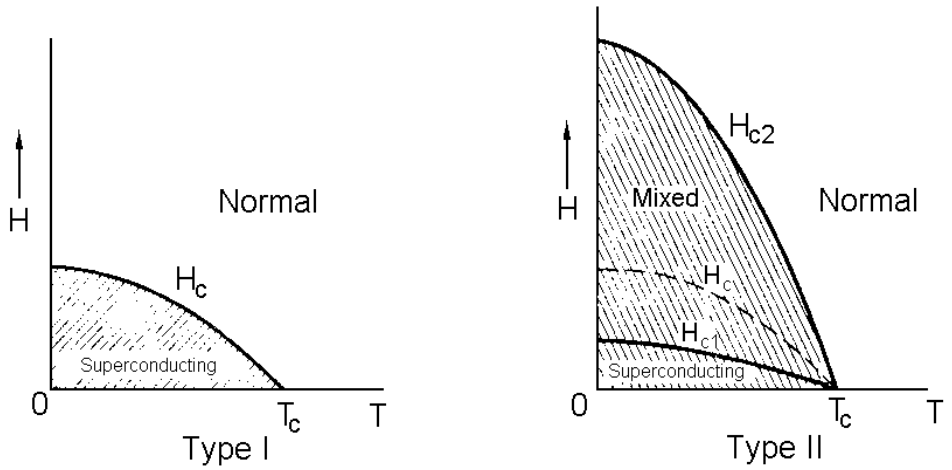

Figure 1.3. H-T phase diagrams of type-I and type-II superconductors [8]. H_{c1} is the field at which the onset of mixed-state superconductivity occurs in type-II superconductors. H_{c2} in type II is significantly larger than H_c in type I superconductors.

penetration occurs and the conductor becomes normal. In type-II superconductivity, the behavior is exactly like a type-I superconductor for fields less than $H_{c1} = H_c / \kappa$. As fluxons penetrate a type-II superconductor, the magnetization decreases until becoming zero at $H_{c2} = \phi_0 / 2\pi\xi^2$, at which point the sample is fully penetrated by field.

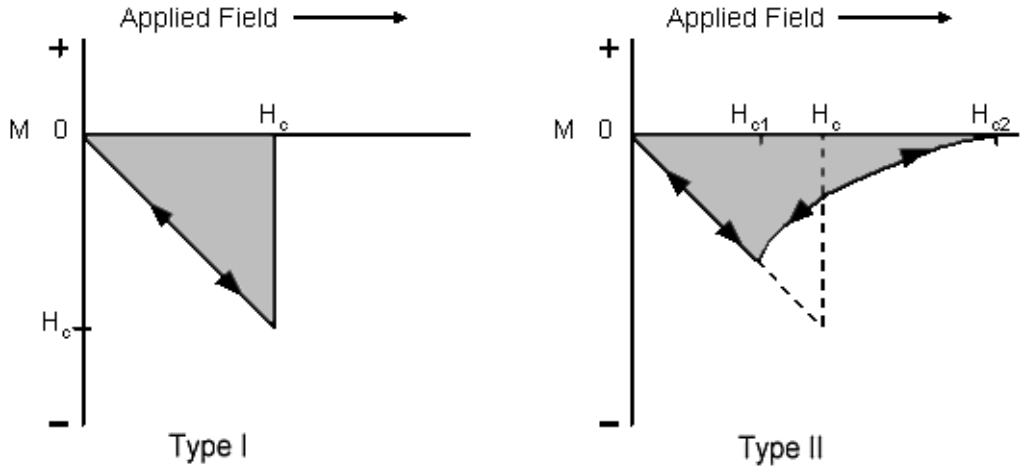

Figure 1.4. Ideal magnetization curves of type-I and type-II superconductors at a constant temperature below T_c. In the ideal case the curves are completely reversible. The shaded areas for both magnetization curves are equal to the free energy difference between the superconducting state and the normal state ($\frac{1}{2}\mu_0 H_c^2$). Thus, H_c of the type-II superconductor can be approximated as the value that makes the area under the dashed curve equivalent to the area under the shaded curve.

As current is introduced into a type-II superconductor, a Lorentz force ($F_L = J \times B$), perpendicular to the applied current and field, acts on the fluxons. Imperfections in the superconductor, such as dislocations, normal phases, grain boundaries and voids, lower the free energy of fluxons and serve as a pinning sites. These pinning sites offer an opposing force to F_L known as the flux pinning force (F_p). The critical current density (J_c) is defined by the condition $F_L = F_p$, thus $F_p = J_c \times B$. If the applied field or current is great enough, F_L exceeds F_p and flux motion occurs. Flux motion results in a flux flow resisitivity that produces a dissipative superconducting state.

The three critical superconducting properties, critical temperature (T_c), upper critical field (H_{c2}) and critical current density (J_c), create a three-dimensional space within which

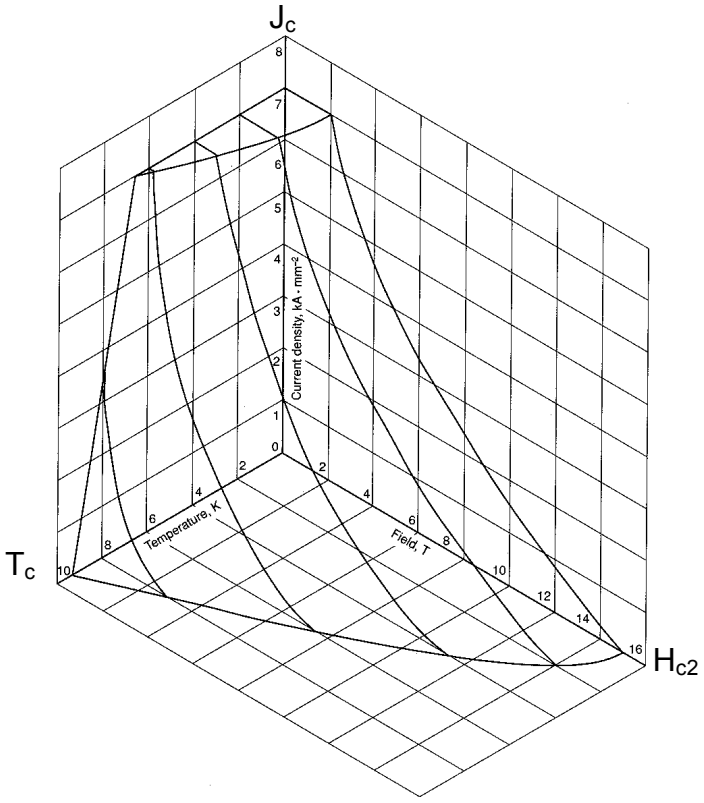

Figure 1.5. The three-dimensional space for which an ideal superconductor is in the superconducting state [10].

lossless bulk supercurrents can flow in type-II superconductors (Figure 1.5). The three properties are interdependent with each other.

Material imperfections (grain boundaries, compositional inhomogeneities, normal phases, etc.) found in all "real world" superconductors don't allow for ideally exhibited type-II superconducting behavior. As illustrated in Figure 1.6, a significant portion of the magnetization curve for real superconductors is irreversible. This behavior results from the fact that the fluxons are "pinned" to imperfections in the material and prevented from moving freely. Thus, as the applied field is increased above H_{c1}, the entry of fluxons into the superconductor is inhibited. Likewise, as the applied field is reduced from a value greater than H_{c2} the exiting of fluxons from the superconductor is hindered. Therefore, in the irreversible regime the number of fluxons at a given applied field while the magnetic field is being increased is smaller than the number of fluxons at the same field when the magnetic field is being decreased (Figure 1.6). This difference in magnetization for increasing and

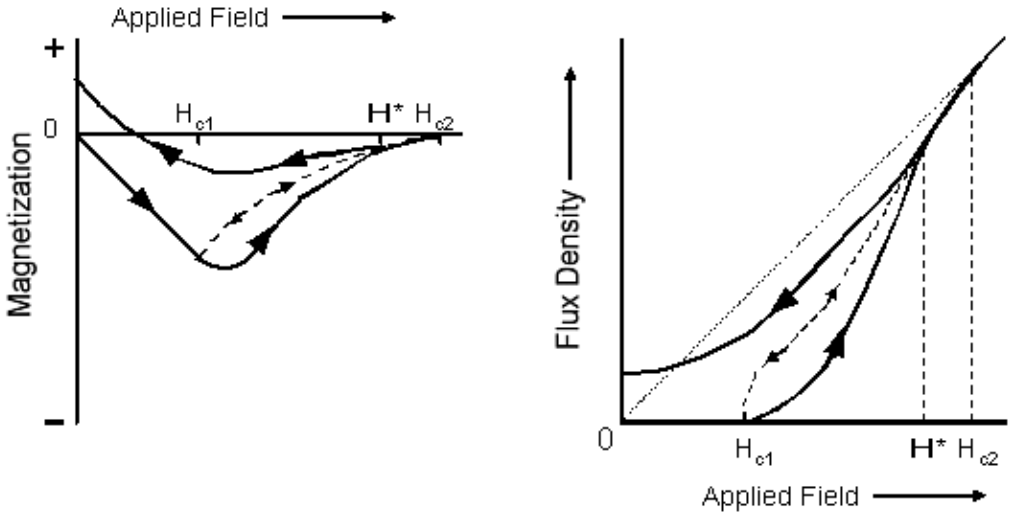

Figure 1.6. Irreversible type-II magnetization curves (solid lines) [Adapted from 8]. The dashed lines illustrate reversible magnetization. H* marks the transition between reversible and irreversible behavior. At H_{c2} the superconductor is fully paramagnetic.

decreasing applied fields is directly related to the flux pinning properties of the superconductor. It was first realized after the discovery of high temperature superconductivity that the irreversible behavior can be destroyed at a field below H_{c2}. The field marking the irreversible-reversible transition is commonly referred to as the irreversibility field, (H_{irr} or H*). Above this field, dissipation-free bulk supercurrents do not exist.

1.3 Nb_3Sn Properties

Nb_3Sn is one of 76 known A15 compounds [11]. For the generic A15 compound A_3B, the crystal structure is formed by a body centered cubic arrangement of B atoms and two A atoms centered at every face (Figure 1.8). Forty-six A15 compounds are known to be superconducting, niobium and vanadium compounds generating the highest T_c values. The excellent superconducting properties found in A15's are attributed to the close distance of approach of the Nb or V atoms and to the high degree of order in stoichiometric compositions. Mathias observed that the electron-to-atom ratio of 4.75, common in many Nb

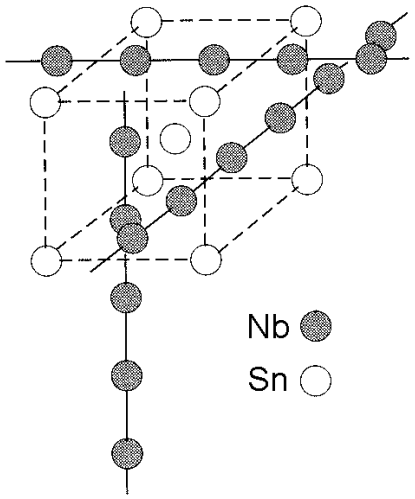

Figure 1.7. Atomic arrangement of a generic A15 compound (A_3B) [11].

and V compounds, produces high T_c values [12]. The A atoms are atomically spaced 10-15% closer than in pure A, creating a high d-band density of states. A correlation between superconductivity and d-band density of states has been established in V_3X compounds [13].

The Nb-Sn phase diagram, as determined by Charlesworth [14] is shown in Figure 1.8. The Nb-Sn system consists of 3 intermediate phases: $NbSn_2$, Nb_6Sn_5 and Nb_3Sn, where Nb_3Sn is the lone superconducting phase. Unlike $NbSn_2$ and Nb_6Sn_5, Nb_3Sn is not a line compound and exists over the range of compositions from 18-25 at% Sn. Stoichiometric Nb_3Sn has a T_c of 18.3 K, however T_c diminishes with decreasing Sn composition, to a value of 6 K at the Sn-poor side of the Nb_3Sn phase (Figure 1.9). A cubic to tetragonal phase transformation occurs at 43 K [15] for compositions from 24.5-25 at% Sn [16].

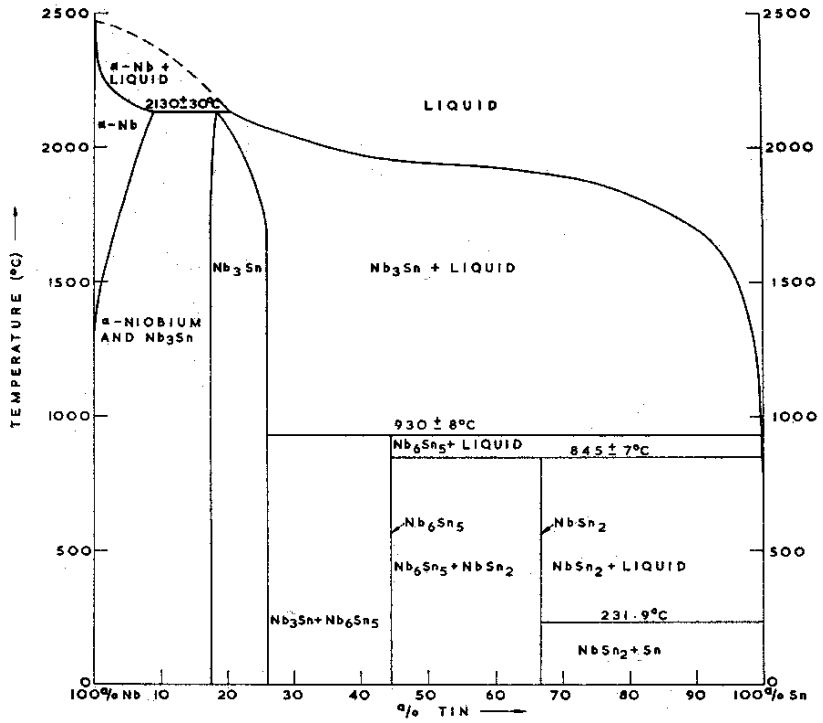

Figure 1.8. The Nb-Sn phase diagram [14]. The Nb_3Sn phase exists from 18-25 at% Sn.

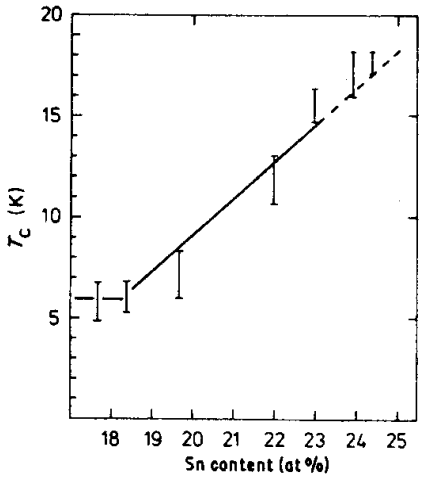

Figure 1.9. T_c increases with increasing Sn content in A15 Nb_3Sn [16].

Nb_3Sn is a classically brittle intermetallic, a property that presents significant challenges in manufacturing the conductor for large superconducting magnets. For this reason, Nb_3Sn conductors are processed into wire prior to the formation of the brittle Nb_3Sn phase, as will be highlighted in section 1.4. The superconducting properties T_c, H_{c2} and J_c exhibit a high degree of strain sensitivity as shown in Figure 1.10, Figure 1.11 and Figure 1.12, respectively. Not only does the strain sensitivity introduce handling concerns, but residual strains (typically compressive) can be retained in the Nb_3Sn upon processing. For example, in Nb_3Sn conductors reinforced with stainless steel prior to reaction, compressive prestrains of 0.6-0.9% can be developed due to the differential in thermal contraction between the steel and Nb_3Sn [17]. Residual pre-compressions are highly beneficial in that they increase the fracture tolerance of the conductor, although this benefit is obtained only by a depression of the superconducting properties. In solenoidal magnets with significant hoop strain, the electromagnetic self-stress can potentially relieve this pre-compression.

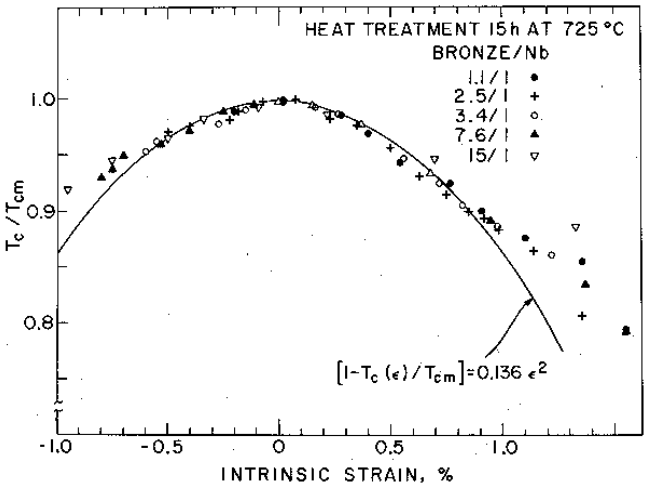

Figure 1.10. Strain dependence of T_c for Nb_3Sn bronze-processed monofilament conductors [18].

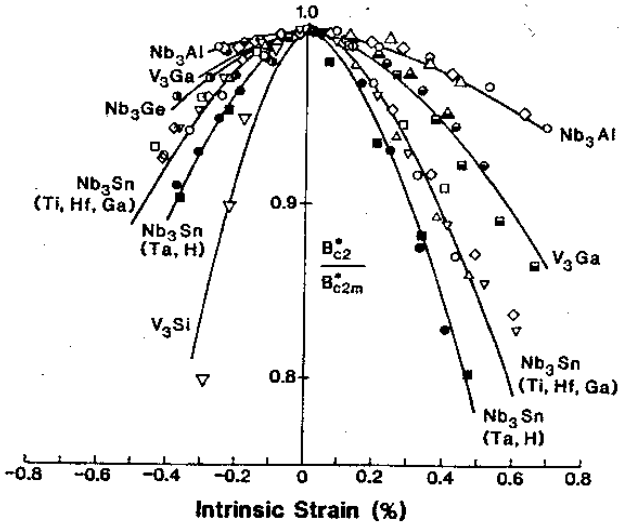

Figure 1.11. Strain dependence of the upper critical field for various A15 compounds [17].

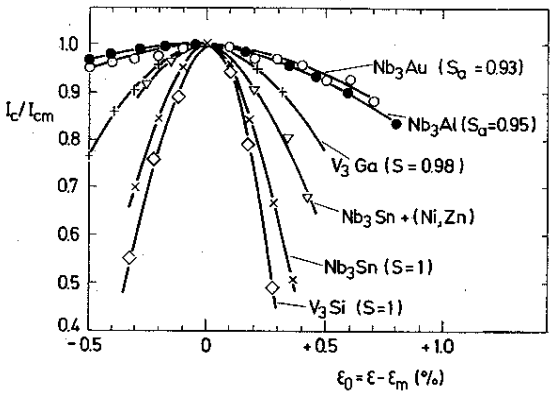

Figure 1.12. Strain dependence of critical current for various A15 compounds [19].

It is well established that the most important magnetic flux pinning centers in Nb_3Sn compounds are the grain boundaries [20, 21, 22]. Pinning force (F_p) evaluated at its maximum, generally ~5 T at 4.2 K, versus inverse grain size is shown in Figure 1.13. F_p is seen to be proportional to 1/d at larger grain sizes, which corresponds to F_p being directly

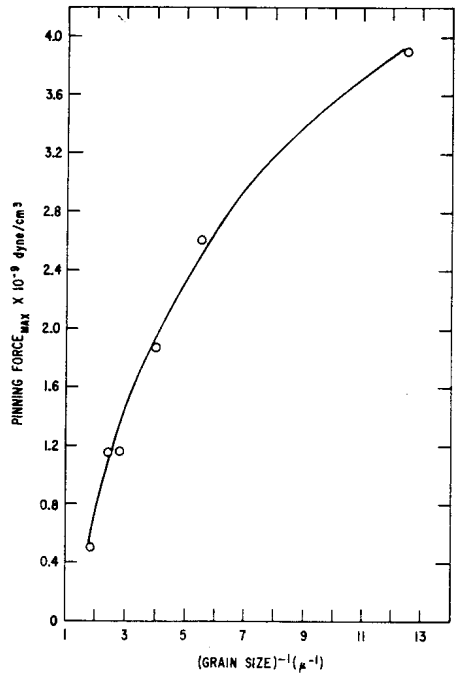

Figure 1.13. Maximum pinning force versus inverse grain size for multifilamentary Nb_3Sn [20].

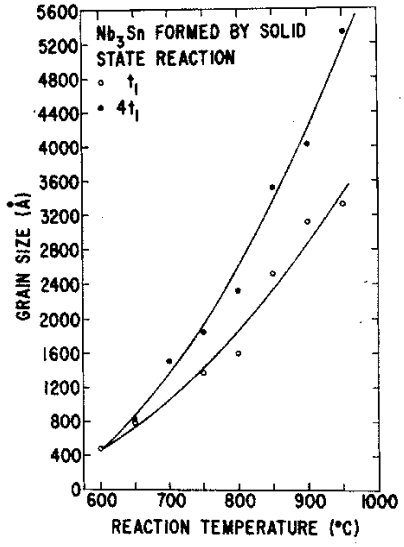

Figure 1.14. Grain Size versus reaction temperature for multifilamentary Nb_3Sn. Reaction time t_1 was the amount of time required to produce a 1μm thick layer, and reaction time $4t_1$ was the amount of time required for full reaction of the filaments [20].

proportional to grain boundary area per unit volume. Therefore, achieving a high critical current density (J_c) requires that grain size be kept small, approximately less than 200 nm. A small grain size requires a low Nb_3Sn reaction temperature (Figure 1.14), however a sufficient temperature is required to permit solid-state diffusion of Sn into Nb. Scanlan, Fietz and Koch [20] observed that a 2 μm layer formed after 500 hours when reacted at 600°C. Industrially applications require much shorter processing times (~100 hrs max); therefore, typical processing temperatures are on the order of 650°C. The problem with keeping the reaction temperature low is that lower Sn-content, A15 phase may form, resulting in depressed H_{c2} [23] and T_c values. Growing large, stoichiometric Nb_3Sn layers and at the same time maintaining a fine grain size has been an inherent challenge in processing Nb_3Sn superconductors, and this is a significant theme of this thesis.

The compromise between high Sn-content and fine grain size Nb_3Sn becomes smaller with the addition of alloying elements to the Nb_3Sn matrix. Primary functions of alloy

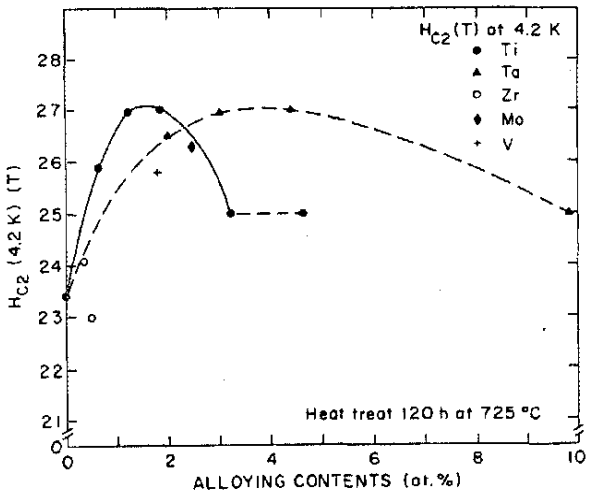

Figure 1.15. H_{c2} (4.2 K) as a function of alloying content for various alloying element additions. Ti and Ta show the largest effects [26].

additions include enhancing the primary superconducting properties (T_c and H_{c2}), inhibiting Nb_3Sn grain growth and increasing Nb_3Sn reaction kinetics. The best alloying elements are capable of performing at least one of these tasks without adversely affecting the others. Three of the most influential alloying elements are Ti, Ta and Mg, and for this reason are employed in nearly all commercially fabricated Nb_3Sn conductors. It has been observed in literature that Ti and Mg increase Nb_3Sn layer growth rate [24,25], Mg inhibits grain growth [25], Ta improves T_c [26] and Ti and Ta help enhance H_{c2} (Figure 1.15) [26]. As a result, all three elements have been shown to improve J_c properties [24,27,28,29].

Cu is also a common alloy addition to Nb_3Sn composites. While its presence has little effect on the primary superconducting properties, it is required to facilitate Nb_3Sn formation. Nb_6Sn_5 and $NbSn_2$ are not stable in the presence of Cu, allowing Nb_3Sn formation at lower temperatures. Without Cu, Nb_3Sn formation below 700°C is not possible, however with as little as 5at.% Cu, Nb_3Sn formation has been observed as low as 450°C [30]. Cu has a very low solubility in Nb_3Sn (~0.3 at.% [31]) and the majority of Cu is found to localize at voids

and grain boundaries [32]. It is unknown whether Cu at the grain boundaries affects the flux pinning mechanism in Nb_3Sn.

1.4 Multifilamentary Wire Fabrication Methods

Numerous methods of A15 wire formation have been developed [33], and the primary multifilamentary fabrication methods currently utilized in industry will be described in this section. These processes include the bronze, internal-Sn and powder-in-tube processes. The advantages and disadvantages of these conductor designs are also discussed.

First however, it is necessary to discuss the critical current density (J_c), the main parameter by which superconducting wires are typically compared. J_c is defined by a normalization of the critical current (I_c) to a defined area. Typically, this area is not the entire cross-sectional area of the wire (engineering critical current density, J_e), but rather the cross-sectional area excluding that made up by the stabilizing Cu. The normalization of current in this manner is referred to as the "non-Cu J_c" or the "package J_c". Non-Cu J_c is more indicative of the superconducting properties of the conductor compared to J_e since the stabilizing Cu does not carry current while the wire is superconducting. In this section the various manufacturing processes are compared by their non-Cu J_c values.

A major step in Nb_3Sn wire fabrication was achieved when it was realized that solid-state diffusion between Nb and a Cu-Sn alloy could be used to form Nb_3Sn. Thus, the formation of the brittle Nb_3Sn compound could be postponed until the desired dimensions of the multifilamentary conductor were produced. The first multifilamentary Nb_3Sn wire fabrication method to take advantage of this was the bronze process [34]. In this method, Nb

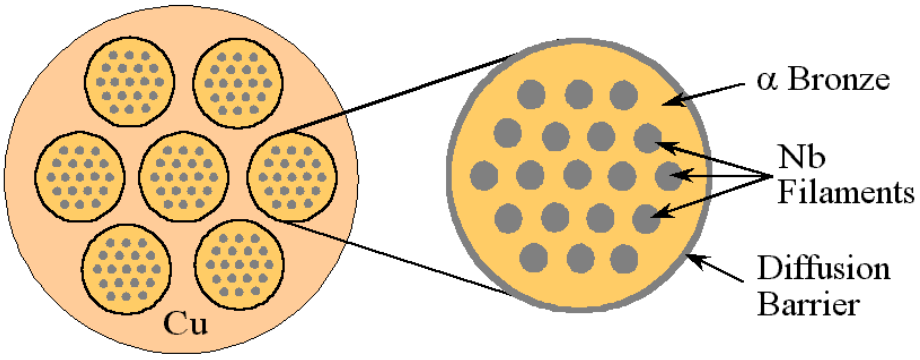

Figure 1.16. Schematic of bronze process conductor [35].

rods are inserted into an α-bronze matrix, extruded and drawn to a final wire size. A schematic of the resulting wire is depicted in Figure 1.16.

There are a few difficulties characteristic of this fabrication method. One is that the bronze work-hardens quickly, and as a result, frequent annealing steps (~50% area reduction) are required during the drawing process. These are labor intensive and run the risk of premature Nb_3Sn formation during the bronze anneals at ~450°C. Another difficulty is that the amount of Sn available for reaction is limited to the solubility of Sn in Cu (15.8wt.%). Furthermore, to avoid formation of the hard δ phase, which is strongly detrimental to the cold forming properties of bronze, the Sn content was limited for many years to about 13 wt.%. Recently however, fine powder spray casting methods have been developed to increase the Sn content to ~15 wt.% Sn, close to the solubility limit [36].

The bronze process is the most developed multifilamentary Nb_3Sn fabrication method and still accounts for much of the Nb_3Sn strand produced. Most bronze-type conductor is used for NMR spectroscopy magnets, with a fair amount used in research fabrication magnets [37]. The advantages of the conductor are its long piece lengths (>2 km), excellent filament quality (effective filament diameters of ~5 μm are very close to the actual A15

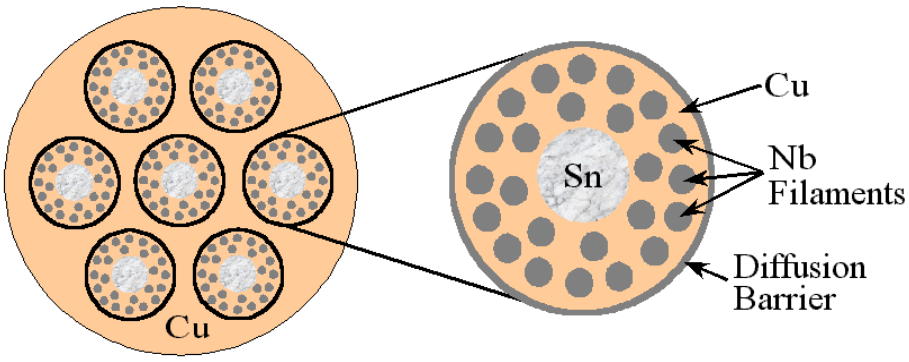

Figure 1.17. Schematic of internal-Sn type conductor [35].

filament diameters) and low hysteretic losses (190 mJ/cm³±3T [38]). Bronze processed wires, however have low non-Cu J_c values (<1000 A/mm²) compared to those produced by other fabrication methods. The primary reason is that the low solubility of Sn in its "carrier" Cu greatly dilutes the overall quantity of A15 phase in the total package.

The internal-Sn process is a second multifilamentary Nb_3Sn wire fabrication method [39]. In this process, a Sn-source is surrounded by Cu-clad, Nb rods in a pure Cu matrix. Typically the Sn-source is alloyed with Cu, Mg or Ti to render the Sn harder so as to make the composite suitable for drawing and to help facilitate Nb_3Sn reaction (as discussed earlier). Such packages can be cold drawn to final size and heat treated to form Nb_3Sn at the site of the Nb rods. A Ta diffusion boundary layer is placed on the outside of the Nb rod sub-elements to keep the Sn from diffusing into the stabilizing Cu matrix. A schematic of an internal-Sn conductor is illustrated in Figure 1.17.

Several advantages exist for the internal-Sn process as compared to the bronze process. One is that the Sn:Cu ratio can be made much higher than in bronze, resulting in much less dilution of the package with "carrier" Cu. Another is that no intermediate annealing steps are necessary since the composite does not appreciably work-harden. A drawback of this method is that hot-extrusion is not possible due to the low melting point of the Sn. This

creates additional labor-intensive drawing steps and limits the degree of bonding obtained during hot working. Recently however, Oxford Superconducting Technology developed a modified internal-Sn method known as the single-stack process [40], which allows for hot extrusion. In this process, NaCl fillers replace Sn during extrusion. After extrusion is complete, the NaCl is dissolved, creating longitudinal holes into which Sn rods are placed.

Currently some of the best internal-Sn conductors are fabricated by a specific technique known as the Modified Jelly Roll method [41], which is a variation of the internal-Sn process. In this method, interleaved layers of Nb expanded metal and Cu are wrapped around a Sn core to form a billet. Non-Cu J_c (12 T, 4.2 K) values of 2,900 A/mm² [7] obtained in these conductors are some of the highest reported for Nb_3Sn multifilamentary wire to date.

Despite the high non-Cu J_c values, the internal-Sn method has inherent disadvantages. Hysteretic losses in these conductors are high due to their large effective filament diameters (~100 μm) resulting from the tendency of the Nb filaments to bridge together. This contrasts strongly with bronze conductors, for which the greater Cu content separates the Nb filaments. Low RRR values in the stabilizing Cu have also been measured, resulting from Sn poisoning of the Cu matrix [42]. Nevertheless, internal-Sn processed conductors are leading candidates for all high-field magnets where high J_c is required.

The most recent multifilamentary Nb_3Sn fabrication method (and the focus of this masters thesis) is the Powder-In-Tube (PIT) technique [43]. In this process, $NbSn_2$ and Cu powder are encapsulated and compacted into a Nb tube. The tubes are stacked into a Cu matrix, which is drawn down to final size. A heat treatment is applied that initiates diffusion of Sn from the $NbSn_2$ and Cu powder core into the Nb tube to form Nb_3Sn. The unreacted

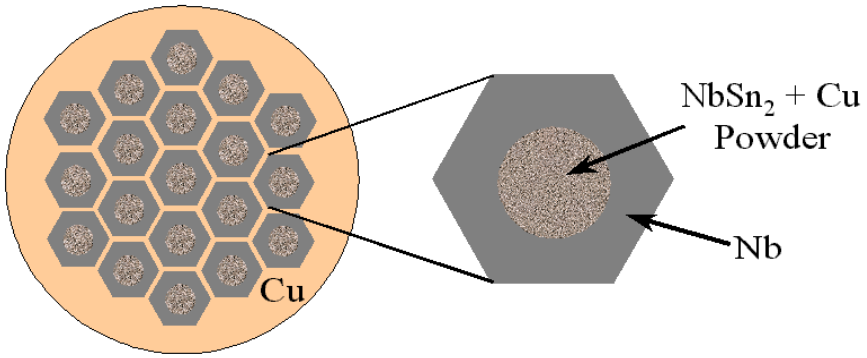

Figure 1.18. Schematic of Powder-in-Tube type conductor [35].

portion of the Nb tube serves as a natural diffusion barrier, protecting the high purity Cu stabilizer from Sn poisoning. A schematic of a PIT conductor is illustrated in Figure 1.18.

There are numerous benefits to this wire design. The high Sn content source in the PIT conductor is capable of producing large areas of Nb_3Sn with compositions close to stoichiometry over the majority of the A15 layer [33]. The heat treatment processing times required in the PIT method are significantly shorter; on the order of days, compared to weeks for the other processes. Effective filament diameters are the tube diameters and thus remain small (<50 μm [43]), resulting in lower hysteretic losses compared to the internal-Sn process where filament bridging occurs. The Nb tube deforms more uniformly with the $NbSn_2$ powder than the Cu tube does in the internal-Sn method; furthermore, PIT wires suffer less pre-compression than other wire designs due to the similar thermal expansion coefficients of Nb and Nb_3Sn. As a result, PIT wires exhibit excellent strain resistance compared to the other fabrication methods (Table 1.1) [44]. Also, a clear T_c advantage for the PIT conductors exists as compared with other conductor designs. Hawes et al. [33] observed a small T_c variation from 18 K to 16.5 K over the majority of the A15 layer in a PIT conductor, whereas

Table 1.1

Critical Current Reduction For Applied Transverse Strain

Conductor	**100 MPa**	**200 MPa**
Powder-in-Tube	2%-4%	5%-8%
Bronze	7%-10%	18%-22%
Modified Jelly Roll	10%-12%	40%-45%

Critical Current measured at 4.2 K and 11 T [44]

bronze and internal-Sn conductors seldom achieve midpoint T_c values greater than 17 K [35,45]. The best PIT conductors have a non-Cu J_c (12 T, 4.2 K) of 2150 A/mm² [42].

One of the major disadvantages in the PIT design may be cost. The fabrication techniques required to produce the Nb tubing and the powder core materials are expensive. Great difficulties have also been experienced in fabricating $NbSn_2$ and Cu powder small enough such that the integrity of the Nb tube remains through the entire drawing process [46] and Sn diffusion isn't inhibited during reaction. The best PIT non-Cu J_c (12 T, 4.2 K) values to date (2150 A/mm² [42]) remain lower than those observed in internal-Sn (2,900 A/mm² [7]). However, this manufacturing method has been the least researched of the three and is far from being optimized. In competition with internal-Sn conductors, PIT conductors offer the solid advantages of small and well-defined effective filament diameters, short reactions times (~2 days) and high critical properties. PIT conductors are major contenders for next generation high field magnet applications.

Aside from the PIT conductor's industrial potential, its inherent design makes it an excellent candidate for the study of compositional dependencies of various superconducting properties. Unlike bronze and internal-Sn type conductors which result in variable composition and variable grain size Nb_3Sn layers less than 2 μm thick, the A15 layers

produced from the PIT design are 5-10 μm thick (depending on filament size) with fairly uniform grain size over a majority of the layer [47]. Their thicker layers permit chemical analysis as a function of position within the layer and their higher degree of compositional and grain size uniformity [47,33] may permit a clearer understanding of the relationships between microstructure, the primary superconducting properties (T_c, H* and H_{c2}) and flux pinning in the A15 phase.

Hawes et al. [33] utilized the magnetically transparent design of PIT conductors to deconvolute the radial dependence of T_c from the temperature-dependent magnetization transition and compared this to the measured composition gradient associated with the formation of the A15 phase. Both data sets show that the Sn-gradient in the A15 phase is non-uniform, the composition remaining close to stoichiometric over most of the A15 layer, falling steeply to the Sn-poor, phase-boundary value of ~18at.% Sn [33] only very close to the A15-Nb interface. Thus, most of the A15 layer had only a small T_c variation from 18 K to 16.5 K. These results suggest why even incompletely reacted PIT conductors can have excellent superconducting properties.

The purpose of this work is to extend the earlier studies of Hawes et al. [33] on the transition temperature (T_c) and composition gradients found in a modern PIT wire to explore how $J_c(B)$, H*, H_{c2} and F_p change with reaction conditions. New binary and ternary (Ta) PIT strands covering the same range of heat treatments at 675°C and 750°C were studied. Additionally, higher temperature reactions up to 850°C were also investigated. The goal was to investigate a large spectrum of Nb_3Sn reacted filaments; from those containing a large Sn composition gradient where very incomplete A15 reaction had occurred, to those in which the A15 reaction had been driven as close to completion as reaction kinetics would allow.

2 Nb_3Sn Formation

2.1 PIT Wire Characteristics

The wires analyzed in this study were manufactured via the powder-in-tube (PIT) approach by ShapeMetal Innovation (SMI), Holland. Two different wires were examined. One contained Nb-7.5 wt.%Ta tubes and the other contained pure Nb tubes. Hereafter, the former wire will be referred to as the ternary wire and the latter as the binary wire. The only other difference between the two wires is that the binary composite has a diameter of 0.98 mm, while that of the ternary is 1.0 mm. The wires contain 192 hexagonal tubular Nb filaments, ~52 μm across flats, each containing a $NbSn_2$ and Cu powder core, themselves embedded in a stabilizing Cu matrix (Figure 2.1). The Nb tubes serve both as the source for the Nb_3Sn reaction and as a diffusion barrier, protecting the stabilizing Cu from poisoning by the Sn-source.

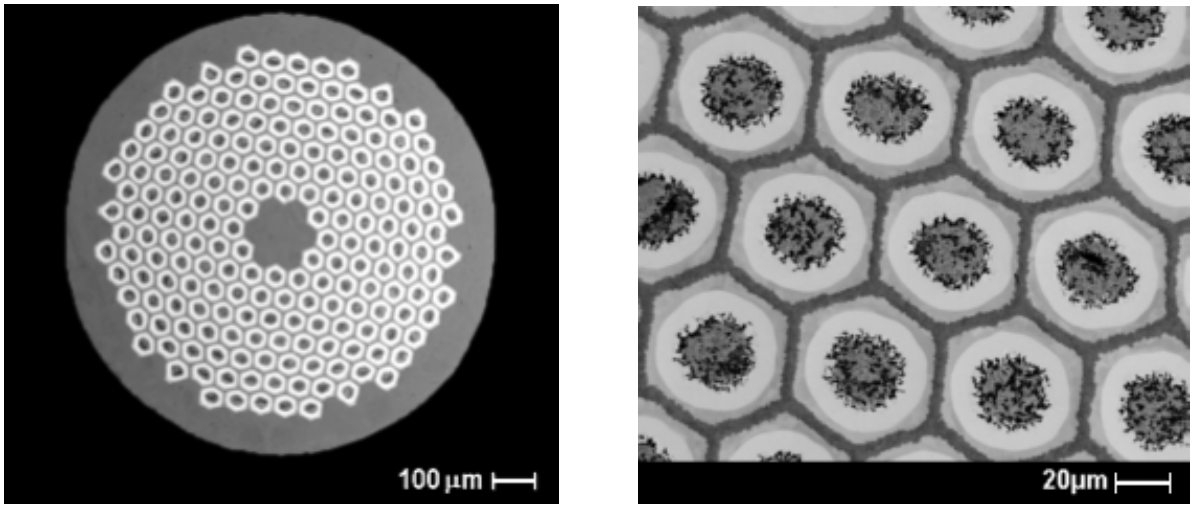

Figure 2.1. Backscattered scanning electron microscope (SEM) images of 192-filament PIT binary composite wire from ShapeMetal Innovation, Holland. The filament diameter is approximately 52 μm. In the right image, the dark circular regions are the filament cores, the light cylindrical regions are the reacted Nb_3Sn layers, the outer regions of the filaments contain unreacted Nb and the matrix is Cu. Both images depict a 47h/675°C reaction in the binary composite.

2.2 Experimental Approach

Table 2.1

Heat Treatment Matrix of Binary and Ternary Reactions

Temp\Time(h)	4	8	16	32	47	64	128	312	512	768
675°C	B T	B T	B T	B T	B T	B T	B T	B T	B T	B T
750°C		B T	B T	B T		B T	B T			
800°C			T	T						
850°C		T								
Two-Step Heat Treatments (Ternary Only)										
850°C	16h/750°C + 24h/850°C									
900°C	16h/750°C + 24h/900°C									
950°C	16h/750°C + 24h/950°C									
1000°C	16h/750°C + 24h/1000°C									

B = Binary
T = Ternary

The ends of ~10 cm long samples were flattened with a ball peen hammer to prevent Sn leakage, sealed in evacuated quartz tubes and heat treated. The binary and ternary strand heat treatments analyzed in this study are shown in Table 2.1. Two-step, elevated temperature reactions were performed to facilitate heat treatments at temperatures greater than 850°C. The initial, lower temperature reaction at 750°C was instituted to transform the $NbSn_2$ powder into Nb_6Sn_5 and finally Nb_3Sn prior to the start of the elevated-temperature reaction. $NbSn_2$ and Nb_6Sn_5 have melting points of approximately 850°C and 930°C, respectively. As a result, large amounts of Sn leakage occurred from the ends of the heat treated specimens when the initial, lower temperature reaction was not performed. While noticeable improvements were observed for the two-step reactions, it is unclear whether the heat treatments completely inhibited Sn leakage from the ends of the reacted specimens.

It should be noted that the thermocouple used to control the reaction temperature of the furnace was discovered to read ~4°C low after completion of the study, and it is unclear what heat treatments were affected by this error.

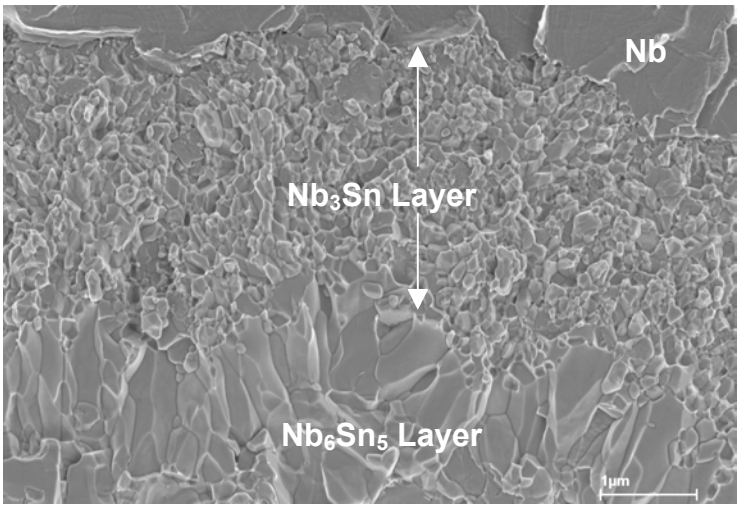

Figure 2.2. FESEM fractograph of the Nb_3Sn layer in a binary wire reaction of 8h/675°C. Grain size and grain boundary density measurements were conducted on the Nb_3Sn region. The large grained Nb_6Sn_5 region and the unreacted Nb region are also visible. The core, which is not shown, lies below the Nb_6Sn_5 layer. After longer reaction times, the Nb_6Sn_5 region transforms into large grained Nb_3Sn. The grain characterization measurements were limited to the small grained Nb_3Sn region in all cases.

Backscattered electron images of transverse cross-sections were obtained with a LEO-1530 field emission scanning electron microscope (FESEM). For each heat treatment, the transverse cross-sectional area of the Nb_3Sn layer and the effective circular diameter of the Nb tube for five representative filaments were measured and averaged. A more detailed explanation of this procedure is provided in Appendix A.

Grain size and grain boundary density values of the Nb_3Sn layer were measured from secondary electron images of wires fractured along the transverse cross-section. The images, obtained in the FESEM, concentrated on the A15 layer within a filament (Figure 2.2). A transparent sheet was laid on top of each printed image, and the grain boundaries of the Nb_3Sn layer were traced by hand. The transparent sheet containing the resulting grain boundary sketch was then scanned, creating an electronic image. This image was processed such that the traced grain boundaries were reduced to a uniform thickness of 1 pixel. From

this image, computer software was utilized to obtain the average feret diameter of the grains and the average grain boundary density (grain boundary length per grain area).

2.3 Nb_3Sn Formation

As the Nb_3Sn PIT conductor is exposed to a reaction heat treatment, Nb_6Sn_5 is the first phase to form upon the diffusion of Sn into the Nb cylinder. It forms just to the outside of the filament core. As the reaction proceeds, Nb_3Sn forms on the outside of the Nb_6Sn_5 layer through the combined processes of Nb_6Sn_5 dissociation and Sn diffusion from the core. The Nb_6Sn_5 phase is easily distinguishable by its larger grain size, as compared to that of Nb_3Sn (Figure 2.3). This initial phase can only be seen after short reaction times, and is no longer visible after the 32h/675°C reaction in the binary composite and the 16h/675°C reaction in the ternary composite. Afterwards, the original Nb_6Sn_5 phase is completely converted into

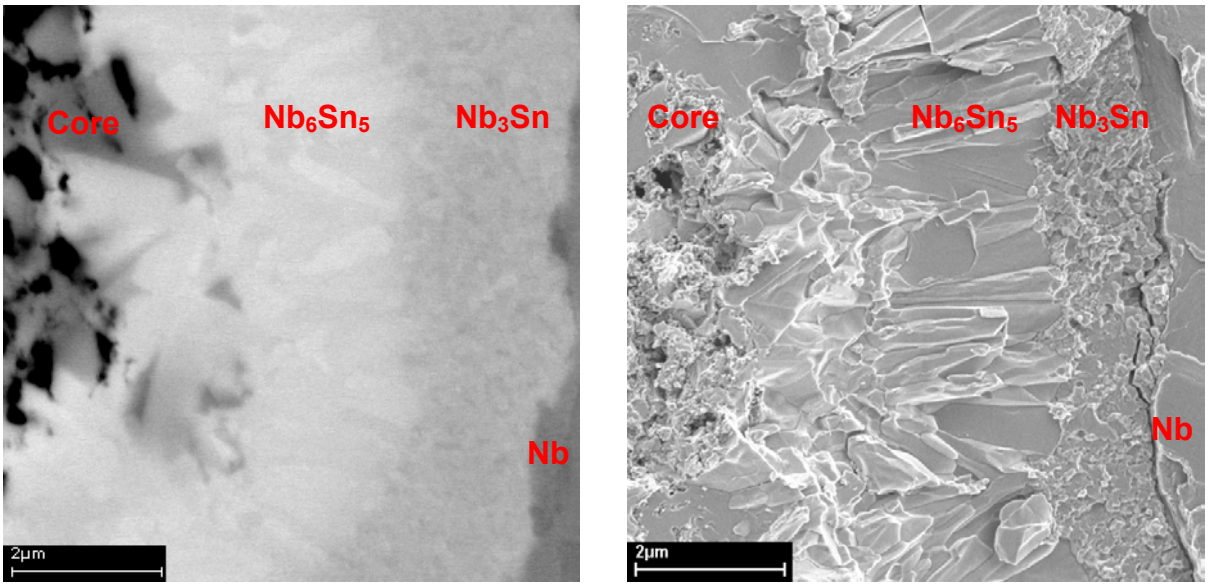

Figure 2.3. FESEM micrographs of the binary composite after 8 hours at 675°C. On the left, is a backscattered electron image of a polished surface, and on the right is a secondary electron image of a fractured surface. From left to right in both images are the filament core, the Nb_6Sn_5 layer, the Nb_3Sn layer and unreacted Nb. The grain size of the Nb_6Sn_5 phase is significantly larger than that of the Nb_3Sn phase. As the reaction continues, the Nb_3Sn layer grows further into the Nb.

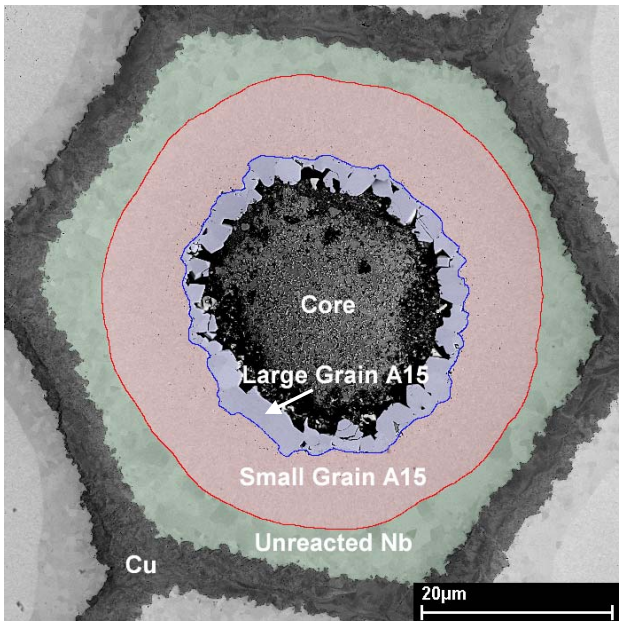

Figure 2.4. A backscattered FESEM micrograph of a single filament in the ternary composite after a 64h/675°C reaction. The image shows the various regions in the filament: unreacted Nb (green), the small grained A15 (red) and large grained A15 (purple). The image in this figure was artificially colored to depict the various regions more clearly.

Nb_3Sn; however, the Nb_3Sn retains the large grain size of the original Nb_6Sn_5 phase, which is significantly larger than the Nb_3Sn phase nucleated directly from Nb. Thus, after the Nb_6Sn_5 is transformed into Nb_3Sn there is a layer of ~2.5-3.0 μm in thickness of large grain size Nb_3Sn on the interior of the small grain size Nb_3Sn layer (Figure 2.4). The outer radius of the large-grained A15 region is non-uniform, resulting in circumferentially varying layer thicknesses for the small-grained A15 region.

Growth of the fine-grain A15 layer as a function of heat treatment time at 675°C is shown in Figure 2.5 and Figure 2.6 for the binary and ternary strand, respectively, and plotted in Figure 2.7. A15 area increases monotonically as a function of reaction time, at 675°C, in both composites although the trend is clearly flattening at long times. The manufacturer's recommended heat treatments for the binary and ternary strand were 47h/675°C and 64h/675°C, respectively. After these reactions, the filaments in both

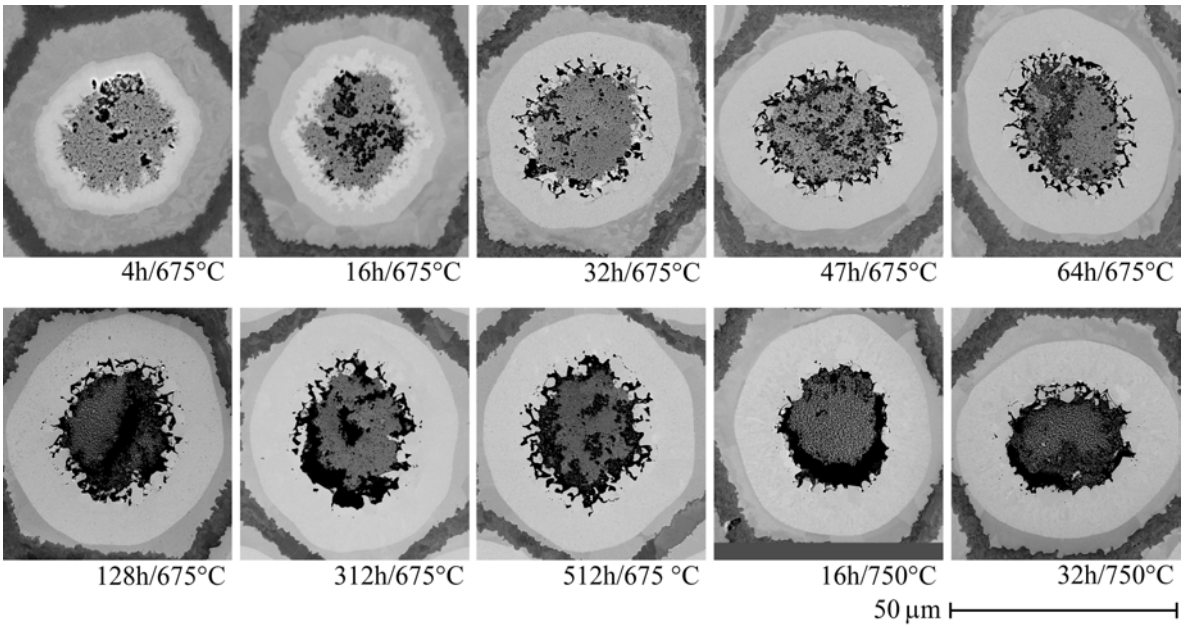

Figure 2.5. Backscatter FESEM micrographs of SMI-PIT binary composite after various heat treatment reactions, illustrating the growth of the A15 layer with time and temperature. The dark circular regions are filament cores, the light cylindrical regions are the reacted areas, the outer regions of the filaments contain unreacted Nb and the matrix is Cu. The reacted regions through 16 hours at 675°C are a mix between Nb_6Sn_5 and Nb_3Sn. By 32 hours, the entire reacted region is Nb_3Sn.

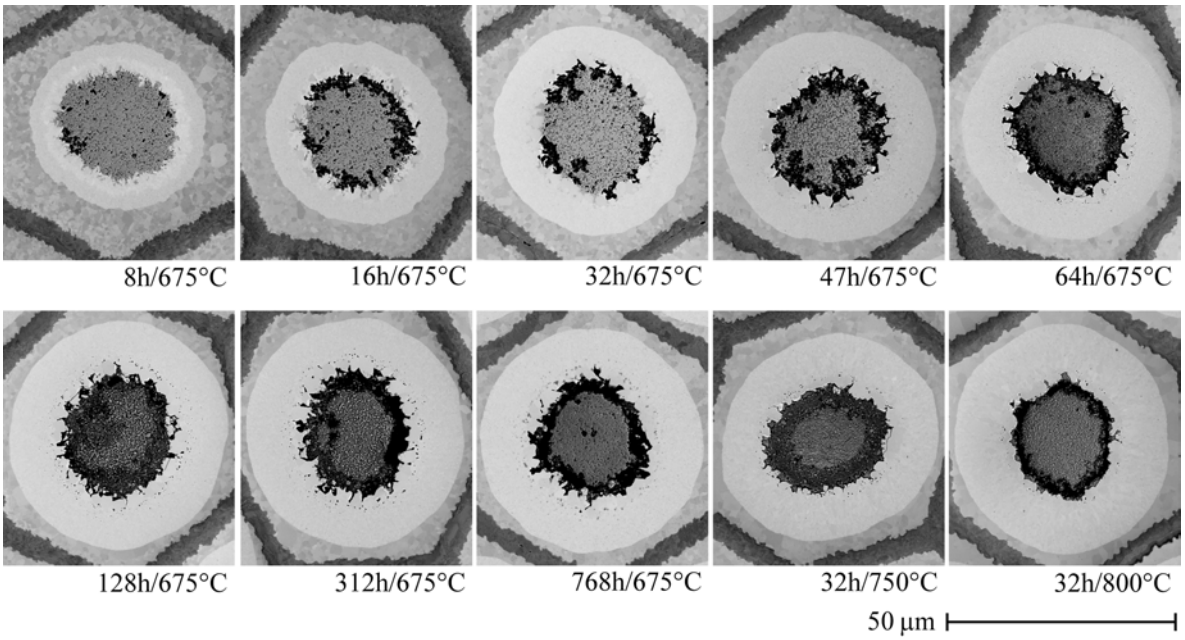

Figure 2.6. Backscatter FESEM micrographs of SMI-PIT ternary composite after various heat treatment reactions, illustrating the growth of the A15 layer with time and temperature. The dark circular regions are filament cores, the light cylindrical regions are the reacted areas, the outer regions of the filaments contain unreacted Nb and the matrix is Cu. The reacted region through 8 hours at 675°C is a mix between Nb_6Sn_5 and Nb_3Sn. By 16 hours, the entire reacted region is Nb_3Sn.

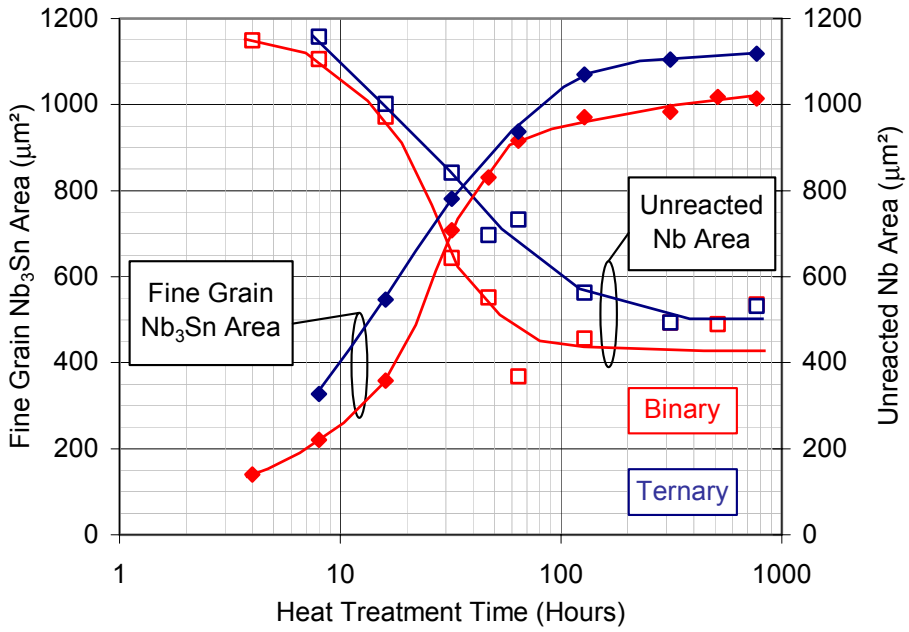

Figure 2.7. A comparison of the fine-grain Nb_3Sn area and the unreacted Nb area in a single filament as a function of time for heat treatments at 675°C in the binary and ternary composites.

composites are composed of ~25% core, ~10% large grained A15, ~40% small grained A15 and ~25% Nb. Only the amounts of small-grained A15 and Nb were found to change appreciably with increasing reaction time. As shown in Figure 2.7, the ternary alloy has a larger Nb_3Sn reacted area as compared to the binary alloy for all reactions studied at 675°C. Figure 2.5 and Figure 2.6 also illustrate the increased kinetics of the A15 reaction at temperatures greater than 675°C. In the binary composite, the A15 area after 32h/750°C is 1,160μm² as compared to 710μm² after 32h/675°C. For the ternary composite, the A15 area after 32h/800°C is 1,150μm² as compared to 940μm² after 32h/750°C and 780μm² after 32h/675°C. The filament size of both composites increases with increasing reaction time as Sn converts the Nb barrier into Nb_3Sn (Figure 2.8).

Through both microscopy and resistivity ratio (RR) (ρ_{300K}/ρ_{77K}) measurements, Sn-breakthrough of the Nb barrier into the stabilizing Cu was confirmed at 675°C for binary

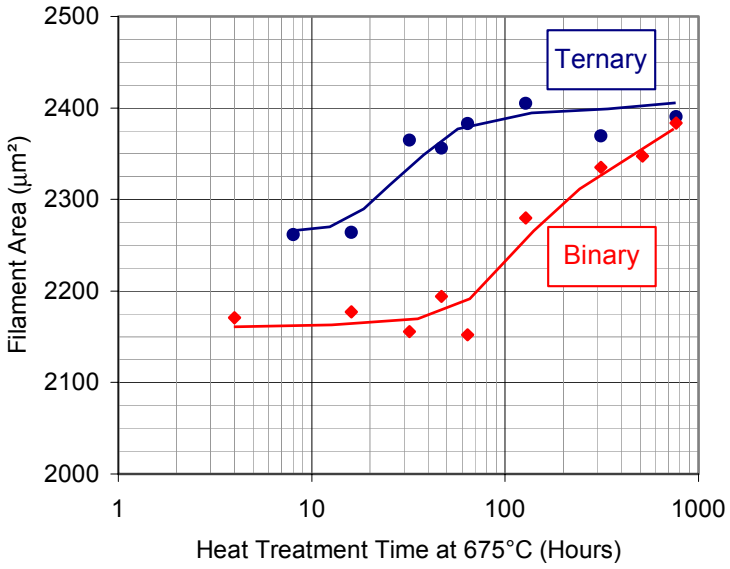

Figure 2.8. Filament area as a function of reaction time, at 675°C, for the binary and ternary composites. The filament area increases with reaction time in both composites as Sn from the core diffuses into the Nb and forms Nb_3Sn.

reactions of 64 hours and longer and ternary reactions of 128 hours and longer. Sn breakthrough was also observed for the 32h/750°C binary reaction. These reactions correspond to fine-grained A15 layers of ~45% of the total filament area. Assuming 25% of the filament area is composed of core and 10% is composed of coarse-grained A15, >20% of the non-Cu area must be composed of unreacted Nb to prevent barrier breakthrough. Over-reaction of the Nb_3Sn layer is somewhat evident in the micrographs shown in Figure 2.5 and Figure 2.6, although the filaments depicted are not necessarily the ones in which Sn breakthrough occurred.

The backscatter images in Figure 2.5 and Figure 2.6 appear to show that large amounts of Sn remain in the filament cores even for the longest and most extensive heat treatment reactions. Energy dispersive spectroscopy (EDS) conducted on the filament cores of the 64h/675°C and 768h/675°C ternary reactions measured 5.7at.%Sn and 6.8at.%Sn, respectively. Many of the filaments contain black regions in the outer most portions of the

core, immediately to the inside of the large-grain Nb_3Sn ring. An EDS measurement performed on this region in the 64h/675°C ternary strand obtained 2.0at.%Sn. The pipeline of diffusing Sn between the core and the Nb_3Sn layer appears to be starved in this region.

Montages of A15 layer grain size and morphology with reaction time and temperature are shown in Figure 2.9 and Figure 2.10 for the binary and ternary composites, respectively. Images were captured at both the center of the Nb_3Sn layer and at the interface between the Nb and Nb_3Sn layers. The grain morphology is largely equiaxed throughout, except for columnar grains occurring at the Nb-Nb_3Sn interface. Grain size remains fairly uniform for all heat treatments performed at 675°C; however, a significant increase in grain size is observed with increasing reaction temperature. Quantitative measurements of grain size and grain boundary density are shown in Table 2.2 and Table 2.3. Grain size was on the order of 150 nm at 675°C, 275 nm at 750°C, 400 nm at 800°C, 500 nm at 850°C and 1650 nm at 1000°C. The grain boundary density values are later used in section 3.5 to calculate the elementary pinning forces (Q_{GB}).

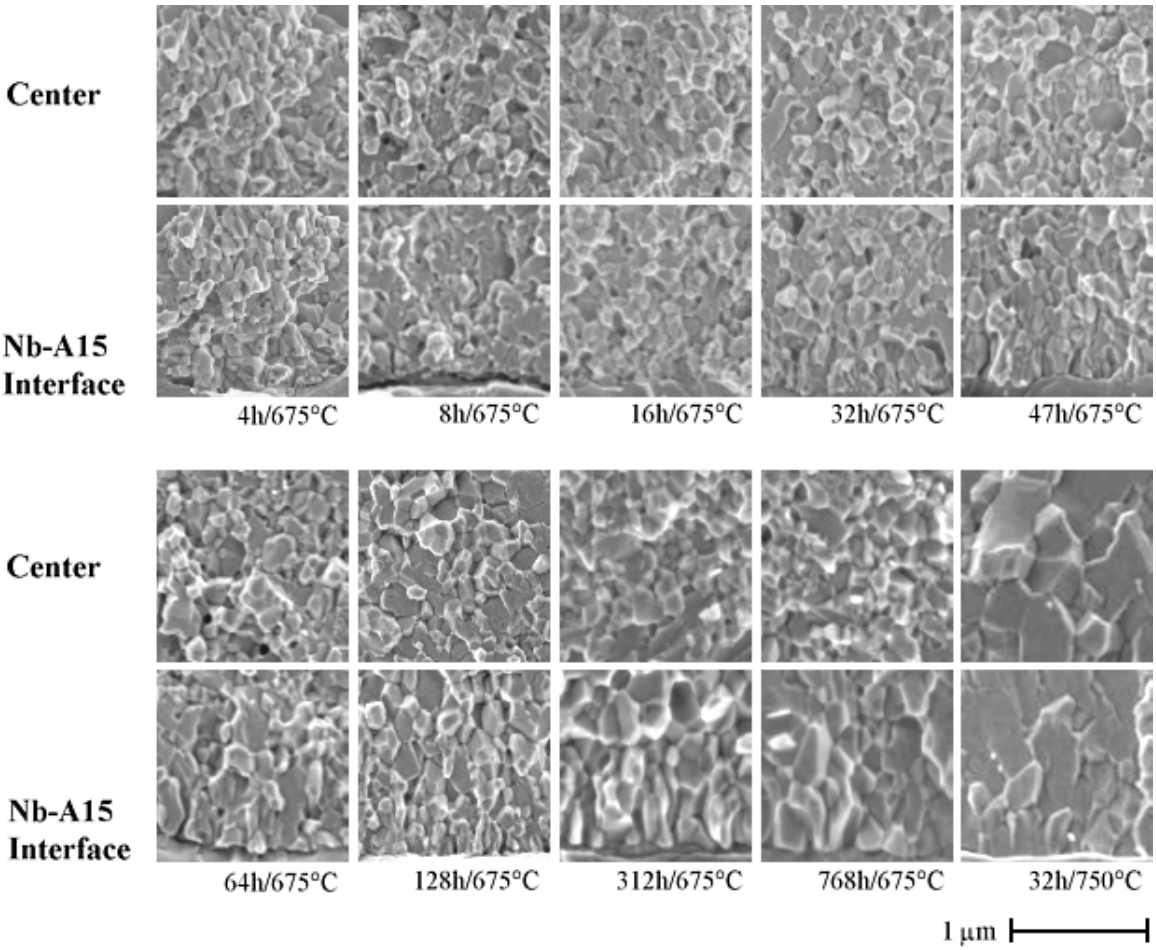

Figure 2.9. FESEM fractographs of SMI-PIT binary composite fracture surfaces after various heat treatment reactions, showing how grain size and morphology change with reaction time and temperature. Secondary electron images were captured from the center of the Nb_3Sn layer and at the Nb-Nb_3Sn growth interface. Grain size and morphology remain fairly uniform for reaction times at 675°C, with only slightly larger grains observed after 312 hours at the growth interface. Significant grain growth occurs at 750°C compared to 675°C.

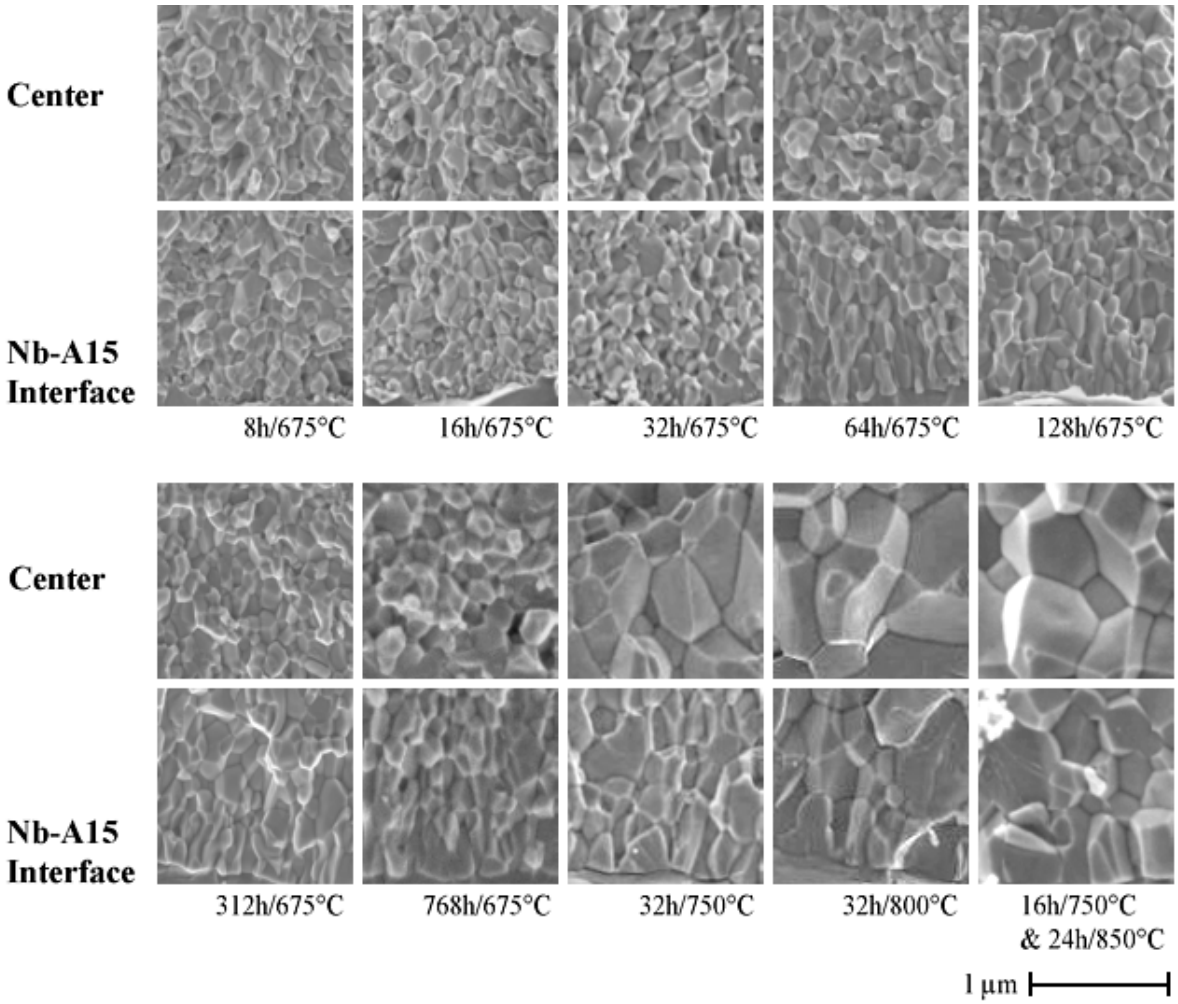

Figure 2.10. FESEM micrographs of SMI-PIT ternary composite fracture surfaces after various heat treatment reactions, showing how grain size and morphology change with reaction time and temperature. Secondary electron images were captured from the center of the Nb_3Sn layer and at the Nb-Nb_3Sn growth interface. Grain size and morphology remain fairly uniform for reaction times at 675°C, with only slightly larger grains observed after 312 hours. A significant increase in grain size as a function of increasing reaction temperature is observed by comparing images of reactions at 675°C, 750°C, 800°C and 850°C.

Table 2.2

Grain Size and Grain Boundary Density Values for Various Binary Wire Reactions

Temperature	Time (Hours)	Grain Size (nm)	Grain Boundary Density (nm/nm²)
675°C	32	134	.0160
	47	124	.0176
	64	127	.0165
	128	141	.0146
	312	160	.0135
	768	170	.0127
750°C	32	254	.00715

Table 2.3

Grain Size and Grain Boundary Density Values for Various Ternary Wire Reactions

Temperature	Time (Hours)	Grain Size (nm)	Grain Boundary Density (nm/nm²)
675°C	8	134	0.0172
	16	157	0.0131
	64	151	0.0137
	128	164	0.0124
	312	169	0.0120
	768	168	0.0130
750°C	16	295	0.00653
	32	268	0.00684
	64	273	0.00735
800°C	16	394	0.00495
	32	384	0.00507
16h/750°C & 24h/850°C		491	0.00408
16h/750°C & 24h/1000°C		1664	0.00135

2.4 Summary

Binary and ternary PIT strands were reacted at temperatures of 675°C and 750°C for times ranging from 4 to 768 hours. In addition, elevated temperature reactions were performed at temperatures of 850°C – 1000°C for 24 hours. The large grained Nb_6Sn_5 is the first phase to form upon the diffusion of Sn into Nb, and is immediately followed by the formation of Nb_3Sn, which is clearly visible after 4h/675°C. Nb_3Sn formation results from the combined processes of Nb_6Sn_5 dissociation and Sn diffusion from the core. The dissociated Nb_6Sn_5 phase results in a large-grained Nb_3Sn region just to the outside of the filament core. The Nb_3Sn reaction was observed to be more rapid in the ternary composite compared to the binary composite. As reaction increases, growth of the fine-grained Nb_3Sn area and expansion of the entire filament area occurs. After the manufacturer's recommended heat treatment time both composites are composed of ~25% core, ~10% large grained A15, ~40% fine-grained A15 and ~25% unreacted Nb. Over reaction of the Nb barrier was observed shortly after these recommended reactions, when the fine-grained A15 region exceeded ~45% of the filament, resulting in Sn poisoning of the Cu matrix. A large amount of Sn was observed to remain in the filament cores even after the longest reactions with low Sn content regions present in the outer most portions of the core, just prior to the large-grain Nb_3Sn ring. The grain size remained fairly uniform with increasing reaction time at 675°C and increased significantly with increasing reaction temperature. While the outer radii of the small-grained A15 regions are very uniform, the inner radii are not. Thus, the fine-grain A15 layers vary in thickness circumferentially. This effect introduces uncertainties to the magnetization derived J_c calculations in chapter 4.

3 Primary Superconducting Properties – T_c, H* and H_{c2}

3.1 Experimental Approach

Critical temperature was measured inductively using a superconducting quantum interference device (SQUID). Samples of ~3 mm were cooled to 6 K in zero field prior to a 50 mT field being applied. Samples were oriented parallel to the applied field. Moment measurements were obtained over 0.1 K temperature increments from 6 – 20 K. The procedure by which T_c values were determined from the resulting moment versus temperature curve is illustrated in Figure 3.1. The quoted T_c values are those measured to be at the midpoint of the critical temperature transition (50% of the baseline value as illustrated

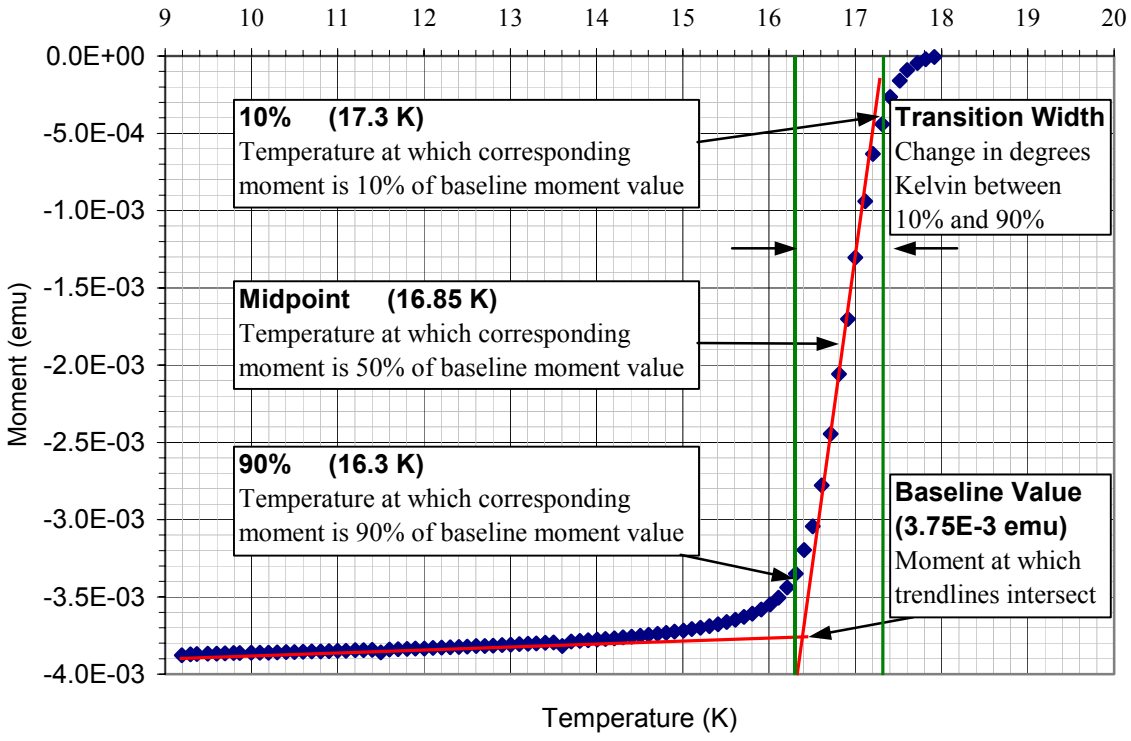

Figure 3.1. Inductive, T_c measurement of the 47h/675°C binary reaction (only the A15 transition is shown). Linear trendlines (in red) were manually fitted to the data as shown above. The intersection of these trendlines characterizes the baseline value of the transition. The quoted T_c value (16.85 K) is the temperature at which the corresponding moment is 50% of the baseline value. 10% and 90% values were identified to characterize the width of the transition. All of the Nb and A15 T_c transitions were performed in this manner.

in Figure 3.1). 10% and 90% of the baseline temperature values ($T_{c\text{-}10\%}$ and $T_{c\text{-}90\%}$, respectively) were obtained to characterize the transition width. The critical temperature transition width is the difference between $T_{c\text{-}10\%}$ and $T_{c\text{-}90\%}$.

Magnetic moment (m) versus field (B) hysteretic loops (Figure 3.2) were obtained with an Oxford Instruments 14 T vibrating sample magnetometer (VSM). Wire samples of ~3 mm in length were oriented parallel to the applied field such that the induced currents flowed circumferentially around each filament. The irreversibility field (H*) and the upper critical field (H_{c2}) were obtained by analyzing the hysteretic loops as illustrated in Figure 3.2 and Figure 3.3.

The irreversibility field (H*) is defined as the field where $J_c = 0$, and can be identified as the field at which hysteretic loop closure occurs. Extrapolation of H* is useful when hysteretic loop closure is too high to be measured. Kramer [48] developed an extrapolation function based on flux pinning of the flux line lattice, where $J_c^{1/2}B^{1/4}$ vs. B extrapolated to zero defines H*. Since the width of the hysteretic loop (Δm) is proportional to J_c, the Kramer

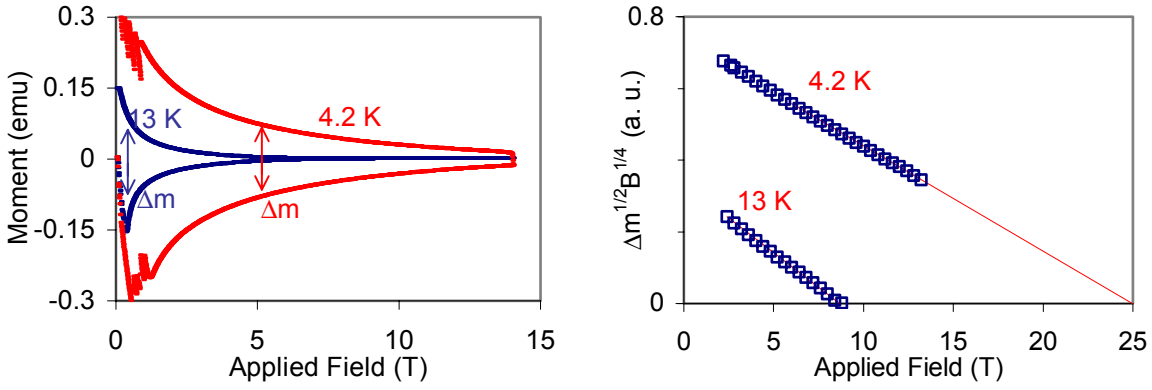

Figure 3.2. The hysteretic loops of a PIT sample measured in the VSM (left) and the resulting Kramer extrapolations (right). The two hysteretic loops were measured from 0 T to 14 T on a ternary strand reaction of 64h/675°C. One measurement was performed at 4.2 K and the other at 13 K. The lower portion of each loop was created by ramping field up and the upper portion by ramping field down. Δm is defined as the difference in moment between the upper and lower portions of the respective loops. On the right is the Kramer extrapolation of H* for the two measurements at 4.2 K and 13 K.

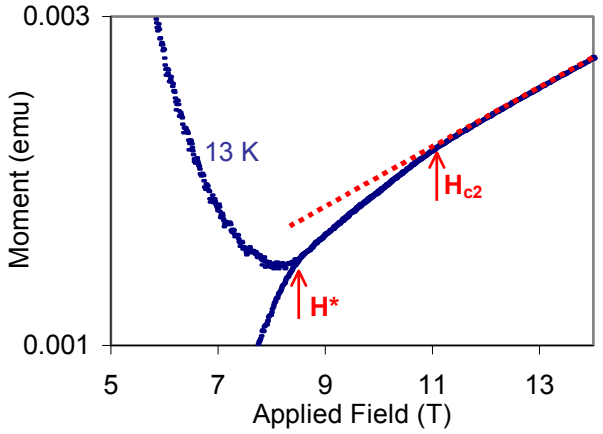

Figure 3.3. An expended view of the high field portion of the hysteretic loop in Figure 3.2 showing H* and H_{c2}. H* is the field at which the loop closes and H_{c2} is the field at which the reversible slope becomes linear, marking the superconducting to normal transition.

function can be modified such that H* is determined by extrapolating $\Delta m^{½} B^{¼}$ versus B to zero. This method has been shown to characterize H* in Nb_3Sn PIT conductors quite well [49], and all H* measurements in this study were determined through Kramer extrapolation (H^*_{Kramer}) of the hysteretic loop data as illustrated in Figure 3.2. Δm was normalized by sample length to enable a relative comparison of I_c values with heat treatment.

The upper critical field (H_{c2}) was defined as the field at which the slope of the reversible magnetization curve deviated from its paramagnetic slope as shown in Figure 3.3. H_{c2} could only be measured below ~13.5 T in the 14 T VSM, and as a result could only be obtained for magnetization measurements at temperatures of 12 K and higher.

3.2 Critical Temperature

Critical temperature curves representative of those measured in this study are shown in Figure 3.4. The two critical temperature transitions result from the two superconducting phases present, Nb and Nb_3Sn. The higher transition results entirely from the Nb_3Sn phase, as the T_c of stoichiometric Nb is 9.2 K. The lower transition initially results from Nb, but

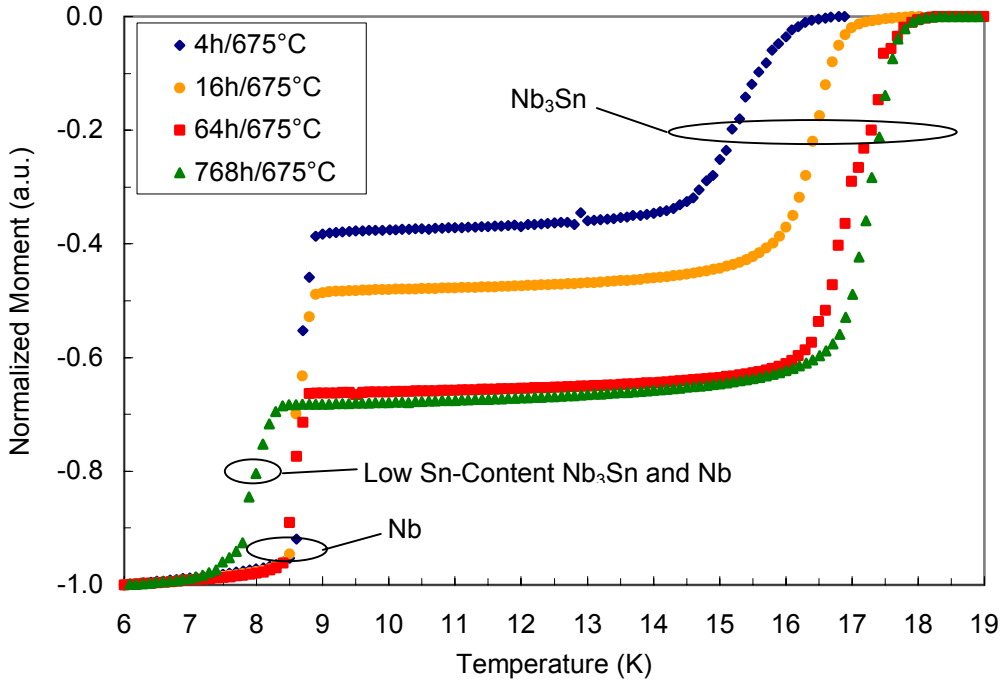

Figure 3.4. Critical temperature curves for various ternary wire reactions showing the two critical temperature transitions. Nb_3Sn creates the higher transition. Nb initially creates the lower transition prior to complete reaction of the Nb barrier, at which point the transition results from a combination of Nb and Nb_3Sn. The curves were obtained by zero-field cooling to 6 K and heating in a field of 50 mT in a SQUID magnetometer.

becomes a convolution of Nb and Nb_3Sn after the Nb barrier is completely reacted through. Prior to the Nb_3Sn phase reacting through the Nb barrier, the Nb shields low Sn-content Nb_3Sn from being observed in the lower transition. After over-reaction occurs, low Sn-content Nb_3Sn phases become represented in the lower transition as observed in the critical temperature curve for the 768h/675°C reaction (Figure 3.4).

Steady growth of the A15 layer with heat treatment time at 675°C can be inferred from Figure 3.4, where the magnitude of the normalized moment is shown to increase with reaction, and from Figure 3.5, where critical temperature (T_c) increases virtually monotonically as a function of increasing reaction time for the two composites. For shorter reaction times, higher T_c values are observed in the ternary wire as compared to the binary wire; however, for reaction times longer than 64 hours the T_c values for both wires are almost

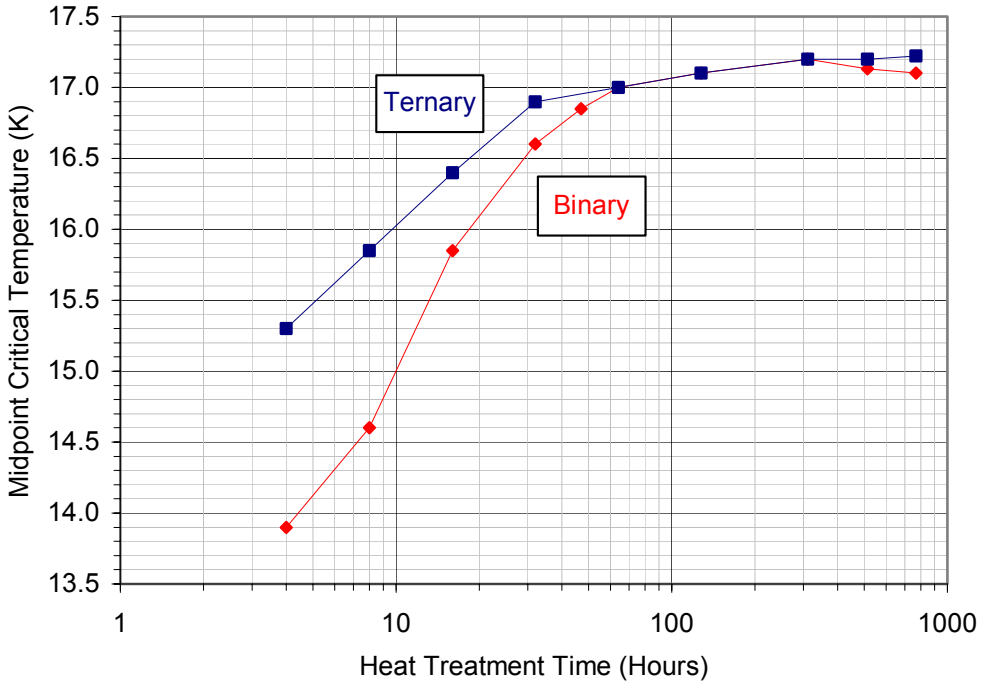

Figure 3.5. Midpoint critical temperature versus heat treatment time at 675°C for binary and ternary strand.

identical. Both strands exhibit maximum values of ~17.2 K at 675°C, compared with the stoichiometric Nb_3Sn T_c of 18.3 K.

Slight increases in Nb_3Sn T_c exist for heat treatments at elevated temperatures above 675°C for both the binary and ternary strand. In the binary wire, the maximum observed T_c was 17.55 K after a 32h/750°C reaction. The maximum measured T_c in the ternary wire was 17.34 K, which was obtained in two separate reactions; 128h/750°C and 8h/850°C. Heat treatment temperatures of 800°C and 850°C did not seem to produce significant increases in T_c, compared to values obtained at 750°C. A summary of the T_c measurements performed in this study is shown in Table 3.1 and Table 3.2.

Figure 3.6 and Figure 3.7 show how the A15 layer $T_{c\text{-}50\%}$, $T_{c\text{-}10\%}$, $T_{c\text{-}90\%}$, and transition width values change as a function of increasing heat treatment time at 675°C for the binary and ternary strand, respectively (The definitions of these parameters were provided in section 3.1). For reaction times less than ~10 hours, a decrease in A15 layer transition width with increasing time was observed in both wires. After 10 hours the transition widths remain fairly constant with increasing reaction times.

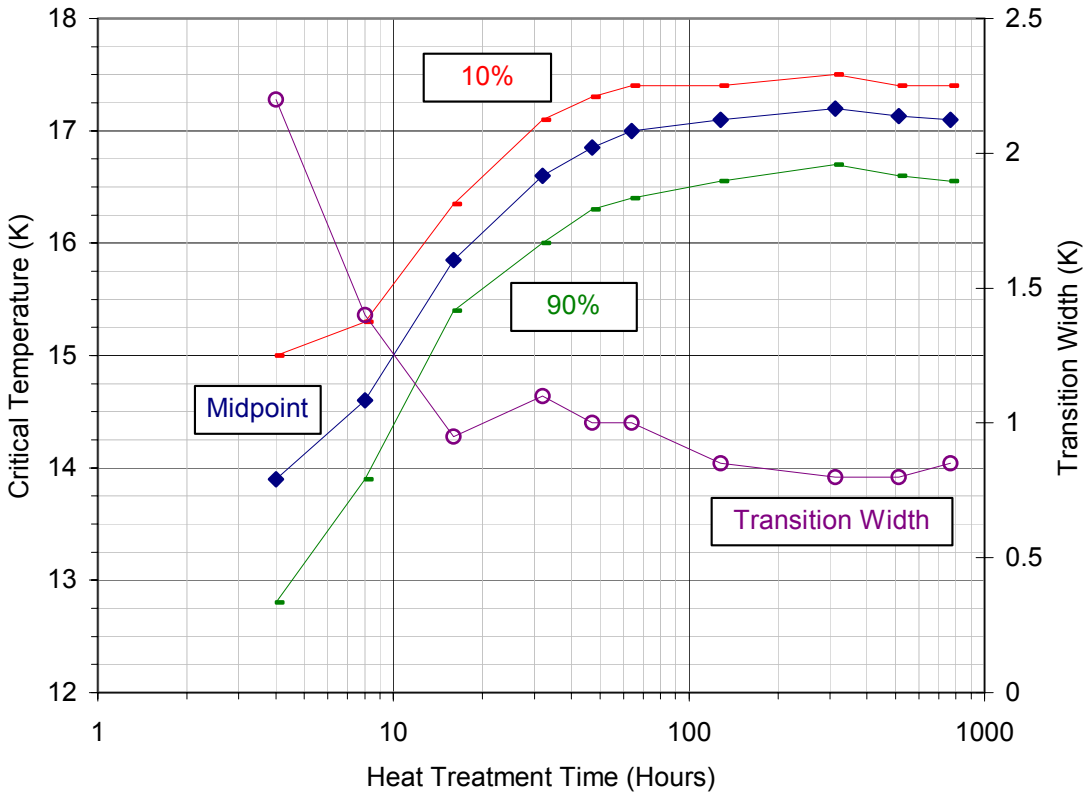

Figure 3.6. A15 layer T_c and transition width as a function of reaction time for binary strand heat treated at 675°C. The midpoint, 10% and 90% T_c values are charted on the left y-axis and the transition width is charted on the right y-axis. The transition width of the binary A15 is fairly constant after 16 hours.

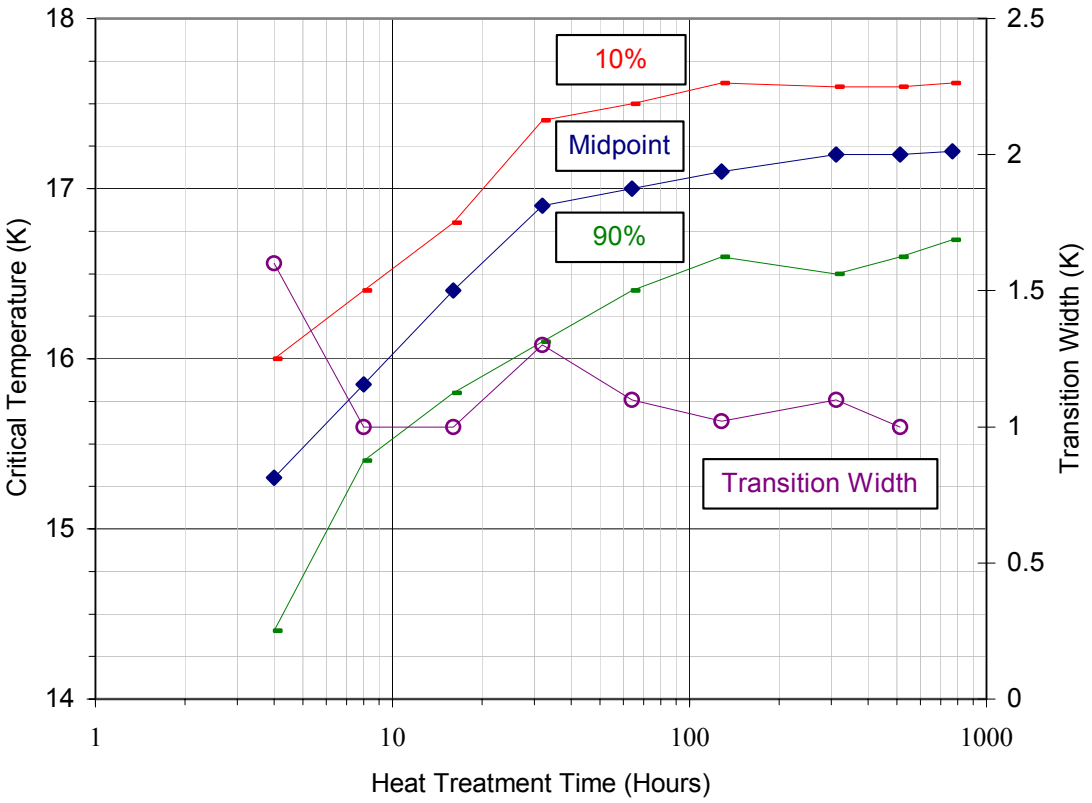

Figure 3.7. A15 layer T_c and transition width as a function of reaction time for ternary strand heat treated at 675°C. The midpoint, 10% and 90% T_c values are charted on the left y-axis and the transition width is charted on the right y-axis. The transition width of the ternary A15 is fairly constant after 8 hours.

Table 3.1

T_c, $T_{c\text{-}10\%}$ and $T_{c\text{-}90\%}$, for Various Binary Wire Reactions

Temperature	Time (Hours)	Midpoint T_c	$T_{c\text{-}10\%}$	$T_{c\text{-}90\%}$
675°C	4	13.9	15.0	12.8
	8	14.6	15.3	13.9
	16	15.85	16.35	15.4
	32	16.6	17.1	16.0
	47	16.85	17.3	16.3
	64	17.0	17.4	16.4
	128	17.1	17.4	16.55
	312	17.2	17.5	16.7
	512	17.13	17.4	16.6
	768	17.1	17.4	16.55
750°C	8	17.41	17.6	16.7
	16	17.54	17.7	16.8
	32	17.55	17.7	16.9
	64	17.41	17.65	17.0
	128	17.45	17.65	16.8

Table 3.2

T_c, $T_{c\text{-}10\%}$ and $T_{c\text{-}90\%}$, for Various Ternary Wire Reactions

Temperature	Time (Hours)	Midpoint T_c	$T_{c\text{-}10\%}$	$T_{c\text{-}90\%}$
675°C	4	15.3	16.0	14.4
	8	15.85	16.4	15.4
	16	16.4	16.8	15.8
	32	16.9	17.4	16.1
	64	17.0	17.5	16.4
	128	17.1	17.62	16.6
	312	17.2	17.6	16.5
	768	17.22	17.62	16.7
750°C	8	16.70	17.32	16.10
	16	17.30	17.53	16.60
	32	17.30	17.50	16.50
	64	17.22	17.60	16.50
	128	17.34	17.60	16.40
800°C	64	17.30	17.55	15.99
850°C	8	17.34	17.55	16.10
	48.5	17.0	17.40	15.50

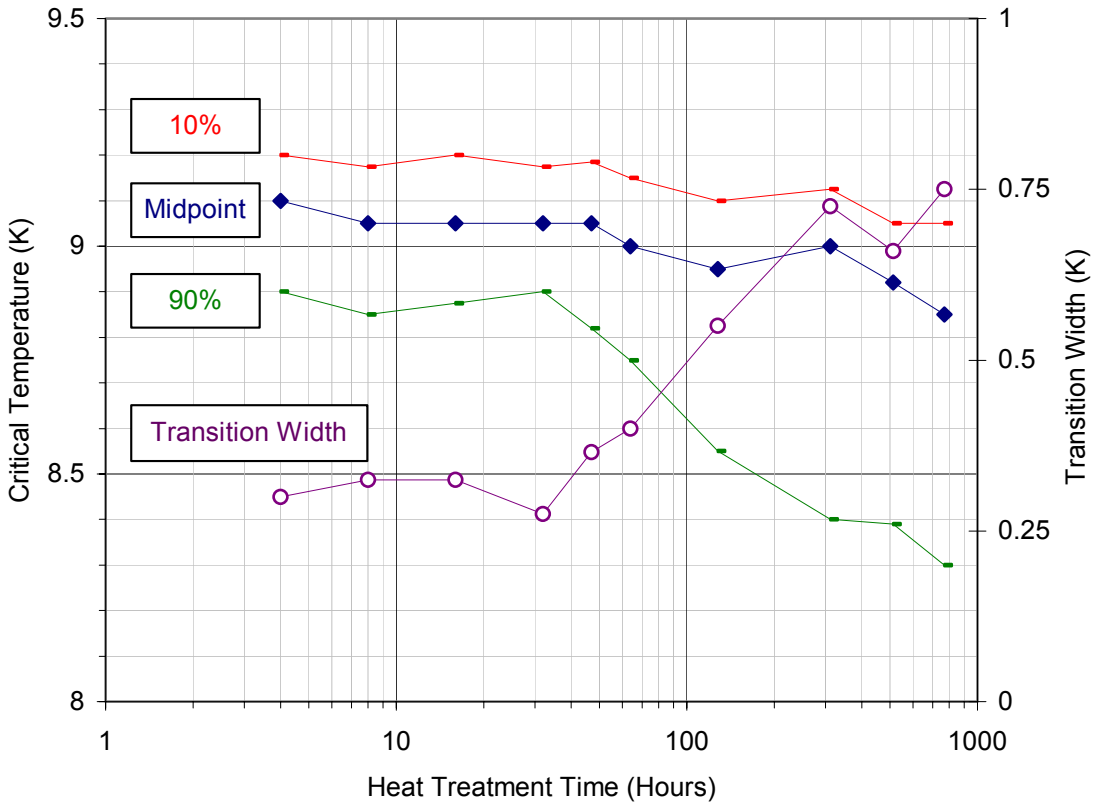

Figure 3.8. The lower critical transition and transition width as a function of reaction time for binary strand heat treated at 675°C. The midpoint, 10% and 90% transition values are charted on the left y-axis and the transition width is charted on the right y-axis. The midpoint of the transition decreases slightly with increasing heat treatment time. This decrease and the slight increase in the transition width is attributed to the moderately decreasing 90% T_c value with increasing heat treatment time after 47 hours.

The effect that increasing reaction time at 675°C has on the lower critical temperature transition is shown in Figure 3.8 and Figure 3.9 for the binary and ternary strand, respectively. The lower critical temperature transitions measured in both composites show evidence of over reaction of the Nb barrier as discussed in section 2.3. For the binary wire, a very slight decrease in the transition midpoint of approximately 0.25 K (9.1 K - 8.85 K) occurs with increasing heat treatment through 768 hours. However, the transition width increases with reaction time, and this effect is mainly attributed to a sharp decrease in $T_{c\text{-}90\%}$ ($T_{c\text{-}10\%}$ remains fairly constant). This sharp decline in $T_{c\text{-}90\%}$ represents a broadening of the

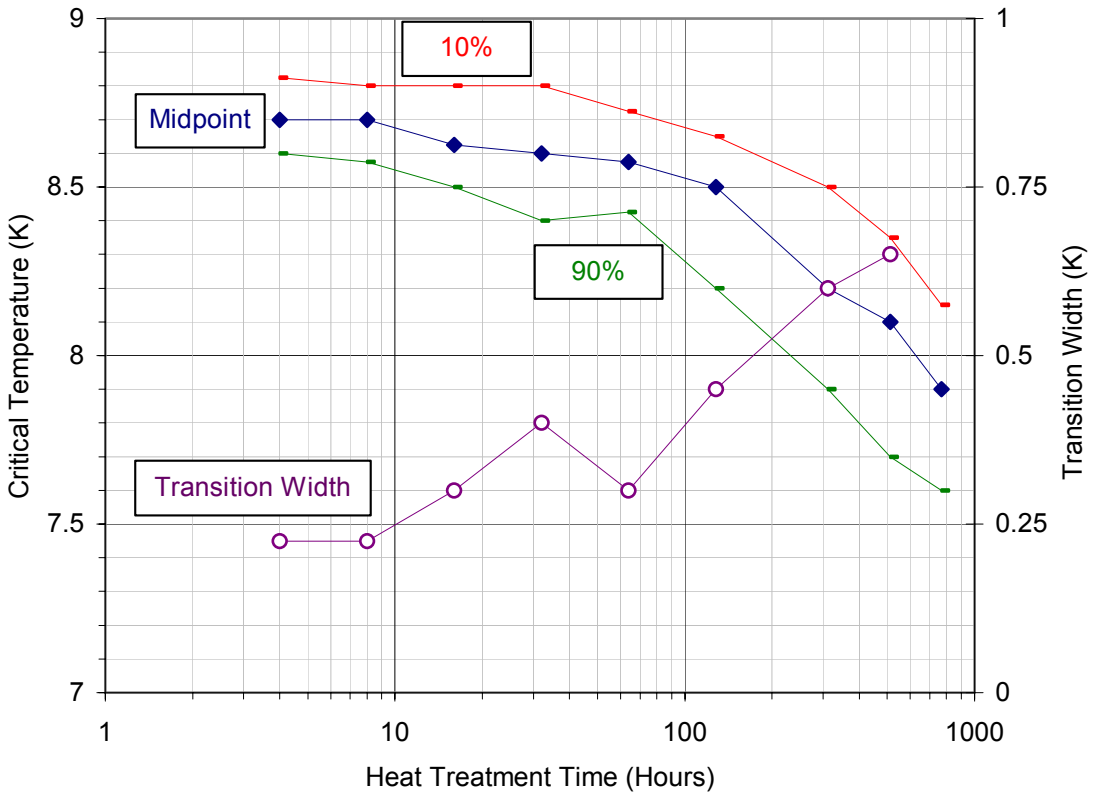

Figure 3.9. The lower critical transition and transition width as a function of reaction time for ternary strand heat treated at 675°C. The transition midpoint, 10% and 90% values are charted on the left y-axis and the transition width is charted on the right y-axis. A significant decrease in the transition midpoint and an increase in the transition width with increasing heat treatment times is observed.

lower temperature side of the transition and coincides with the onset of Nb barrier breakthrough. The ternary wire exhibits a more pronounced decrease in the transition midpoint of approximately 0.8 K (8.7 K – 7.9 K) through 768 hours, as compared to the binary wire. The sharp decline in the midpoint transition after 128 hours coincides with Nb barrier breakthrough. As observed in the binary wire, the lower critical transition of the ternary strand broadens with increasing reaction time.

3.3 Kramer Plots – Irreversibility Field

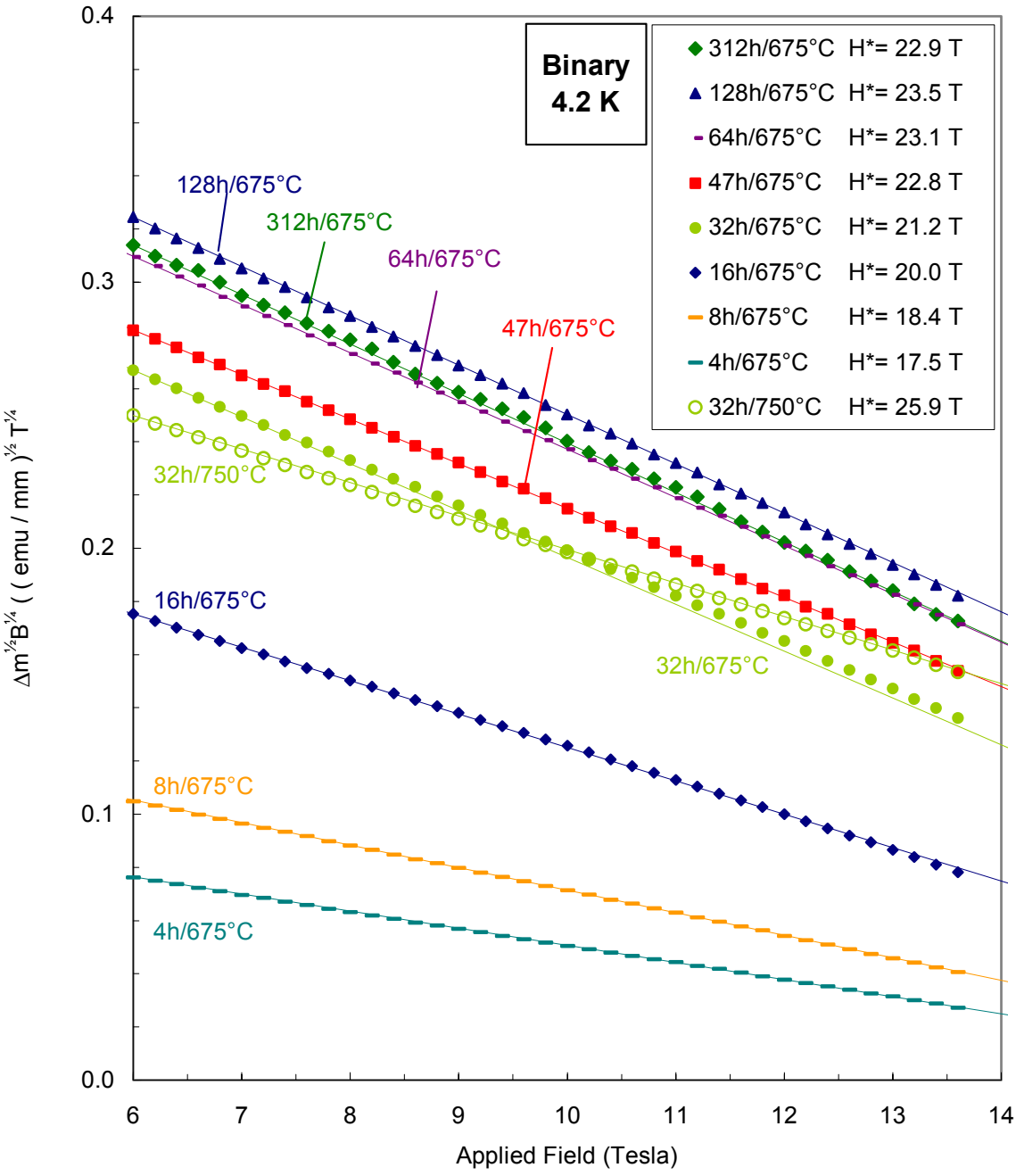

Figure 3.10. Kramer plots, derived from magnetization curves of the binary wire measured at 4.2K, for various heat treatments. H* is the extrapolated irreversibility field. Both H* and I_c ($\propto \Delta m$) increase monotonically with increasing time through 128 hours at 675°C. The Kramer function ($\Delta m^{1/2}B^{1/4}$) exhibits a virtually linear relationship with field. The lines connecting data points are the actual Kramer fits for the respective data. The magnetic moments are normalized to sample length.

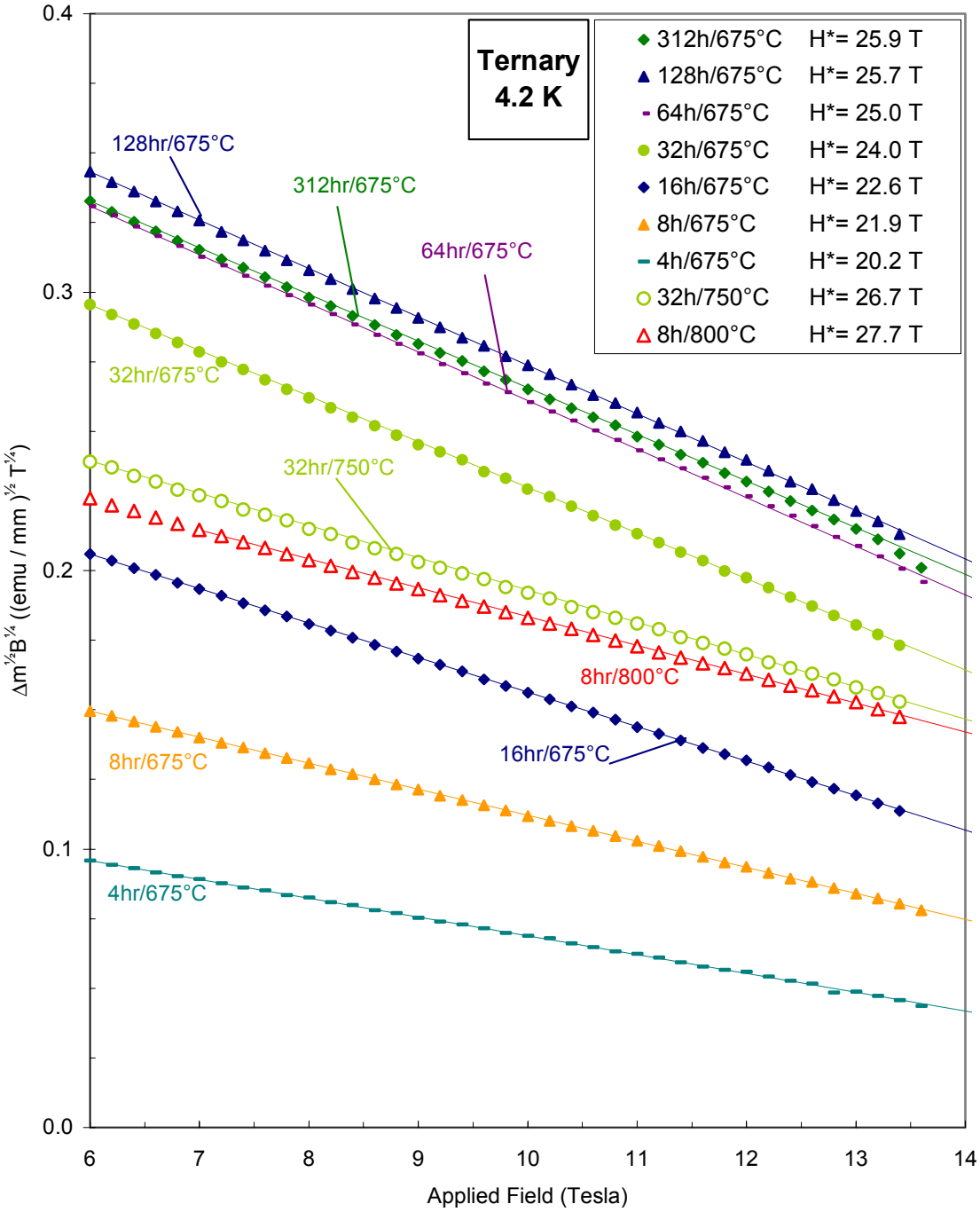

Figure 3.11. Kramer plots, derived from magnetization curves of the ternary wire measured at 4.2K, for various heat treatments. H* is the extrapolated irreversibility field. Both H* and I_c ($\propto \Delta m$) increase monotonically with increasing time through 128 hours at 675°C. The Kramer function ($\Delta m^{1/2}B^{1/4}$) exhibits a virtually linear relationship with field. The lines connecting data points are the actual Kramer fits for the respective data. The magnetic moments are normalized to sample length.

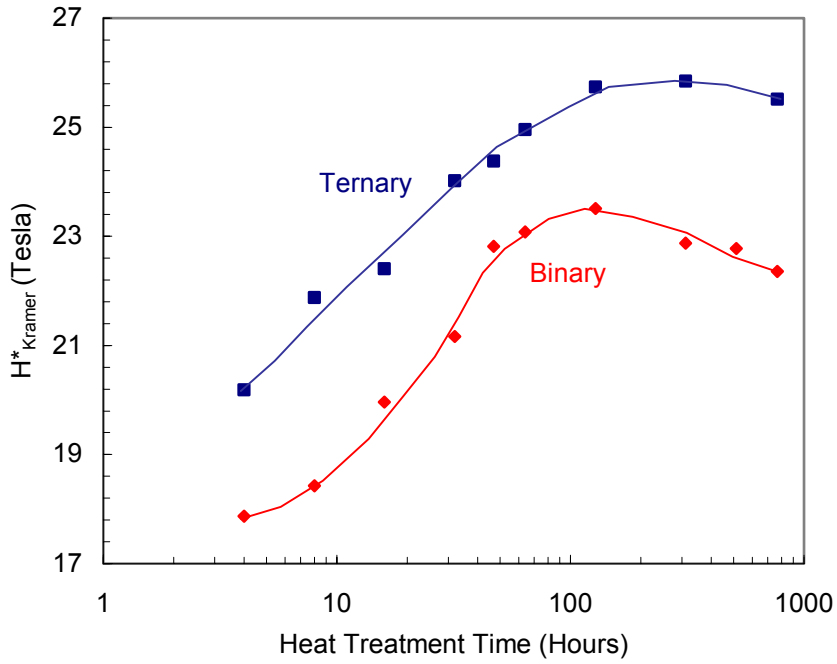

Figure 3.12. H^*_{Kramer} (4.2 K) versus heat treatment time, at 675°C, for the binary and ternary strand.

The 4.2 K Kramer plots for the binary and ternary wires are shown in Figure 3.10 and Figure 3.11, respectively. Δm was normalized by sample length (units of emu·mm^{-1}) so as to show the change of moment of the whole wire, which is proportional to the critical current (I_c) of the wire or the critical current density (J_c) of the A15 fraction produced by reaction of the whole non-Cu, Nb-tube, filament package during heat treatment. The trend lines through the data points are the actual Kramer fits. For binary reactions at 675°C, the irreversibility field (H^*_{Kramer}) increases monotonically from 17.5 to 23.5 T (4.2 K) as time increases from 4 to 128 hours, and for heat treatment times of 312, 512 and 768 hours, H^*_{Kramer} decreases to 22.9, 22.8 and 22.4 T, respectively (Figure 3.12). Binary reactions of 16h/750°C and 32h/750°C achieved H^*_{Kramer} values of 25.7 T and 25.9 T (4.2 K), respectively (Figure 3.10). Thus, a large 2.4 T increase in H^*_{Kramer} was observed when reacting at 750°C rather than 675°C for the binary wire.

It can be inferred from Figure 3.10, that a small decrease in non-Cu J_c occurs in the binary strand after the 312h/675°C reaction as its Kramer curve lies below that of the 128h/675°C reaction. Slight decreases in non-Cu J_c continue for heat treatment times of 512 and 768 hours; however the Kramer curves are not shown so as to avoid congestion in the plot. A significant decrease in the non-Cu J_c of the 32h/750°C reaction is observed compared to reactions at 675°C. The effect of A15 reaction on J_c will be illustrated further in section 4.2 where A15-layer J_c and non-Cu, package J_c values are derived from Δm.

For heat treatments at 675°C in the ternary strand, the irreversibility field (H^*_{Kramer}) increases monotonically from 20.2 T, at 4 hours to 25.9 T (4.2 K), at 312 hours (Figure 3.12). An H^*_{Kramer} value of 25.5 T was measured for the 768h/675°C reaction, indicating that H* may plateau, perhaps even decrease for times greater than 312 hours at 675°C, a similar trend to that observed in the binary strand. The ternary strand also exhibited an increase in H^*_{Kramer} as heat treatment temperature was increased beyond 675°C. Reactions of 16h/750°C, 32h/750°C and 128h/750°C all achieved H^*_{Kramer} values of approximately 26.7 T.

The relative heights of the Kramer plots for the ternary strand indicate a decrease in non-Cu J_c occurs for reaction times longer than 312 hours at 675°C, and temperatures greater than 750°C (Figure 3.11). This is a similar trend to what was observed in the binary strand. The effect of A15 reaction on J_c will be illustrated further in section 4.2, where magnetization data are converted into J_c values.

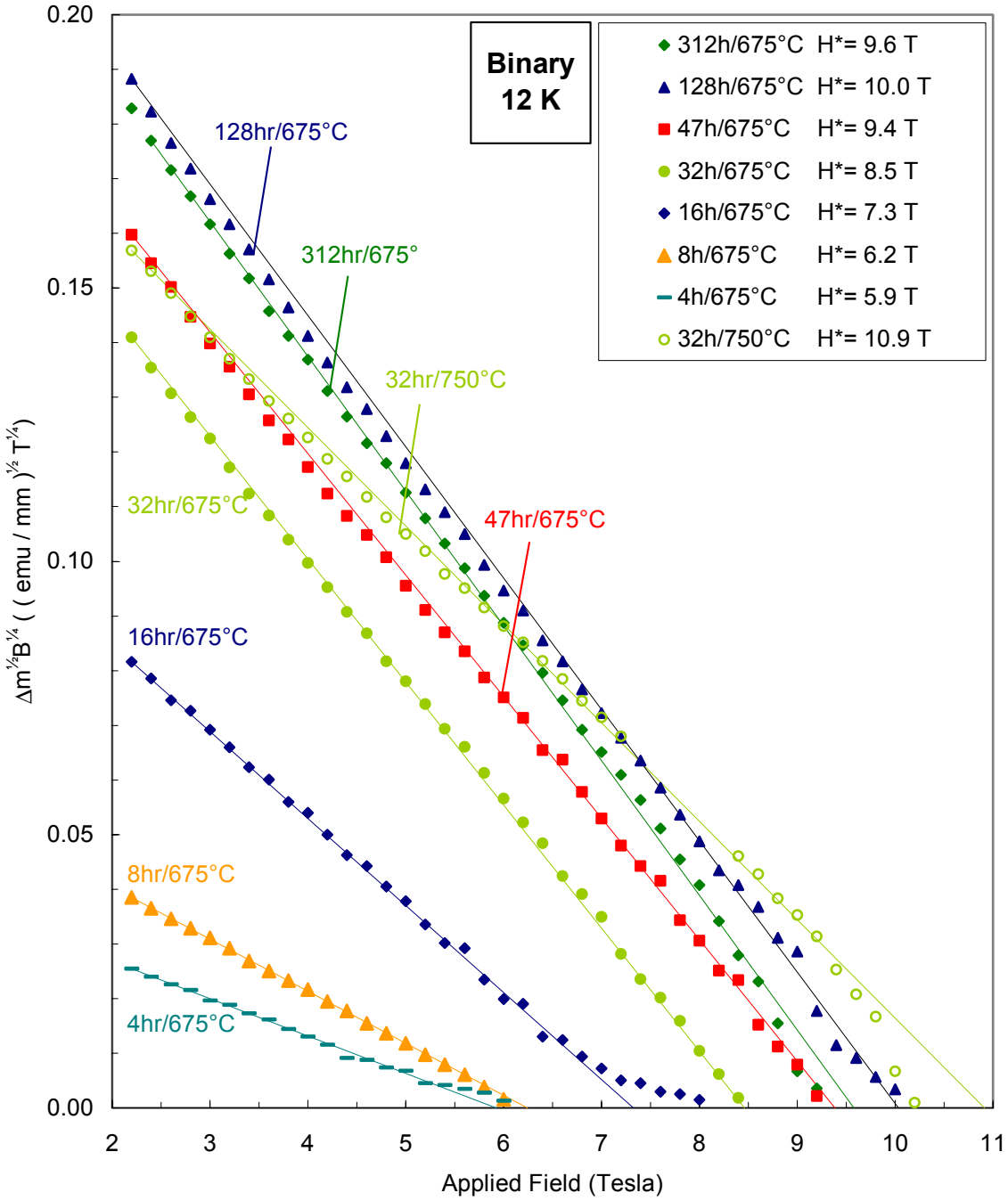

Figure 3.13. Kramer plots, derived from magnetization curves of the binary wire measured at 12K, for various heat treatments. H^*_{Kramer} is the extrapolated irreversibility field. The Kramer function ($\Delta m^{1/2}B^{1/4}$) is linear almost up to H*. The magnetic moments are normalized to sample length, as in Figure 3.10 and Figure 3.11

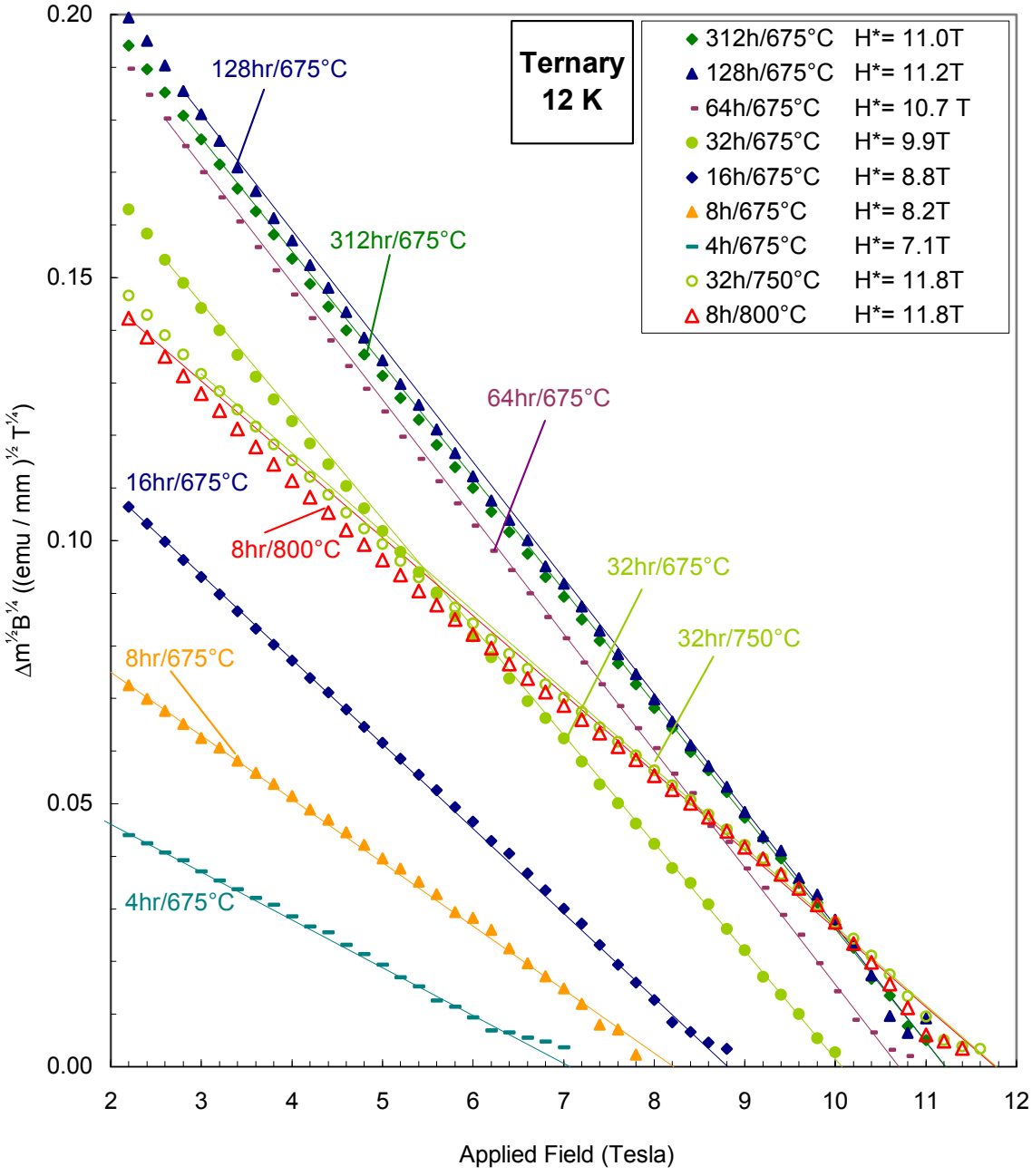

Figure 3.14. Kramer plots, derived from magnetization curves of the ternary wire measured at 12K, for various heat treatments. H^*_{Kramer} is the extrapolated irreversibility field. The Kramer function ($\Delta m^{1/2}B^{1/4}$) is linear almost up to H*. The magnetic moments are normalized to sample length.

The Kramer function fits the magnetizations of all binary and ternary heat treatments performed at 675°C and 750°C quite well; showing practically linear data fits at both 4.2 and 12 K (Figure 3.10, Figure 3.11, Figure 3.13 and Figure 3.14). For reactions at these temperatures, linearity seems to diminish only as H^*_{Kramer} is approached. Since the field of hysteretic loop closure (H_{LC}) and H^*_{Kramer} agree within a half tesla for the majority of binary and ternary reactions measured at 12 K (Table 3.3 and Table 3.4), it appears that 4.2 K H^*_{Kramer} values do indicate true H* values at 4.2 K. The maximum H* values for reactions up to 750°C in the binary and ternary strand, as estimated by H^*_{Kramer}, are approximately 25.9 T and 26.7 T, respectively. H^*_{Kramer} measurement errors are estimated to be approximately 0.2 T based on the consistency of results between individual heat treatment values and duplicated trials.

The Kramer function does not fit magnetizations of ternary reactions performed at temperatures of 800°C and greater very well (no reactions above 750°C were performed on the binary wire), and for this reason, extrapolated H^*_{Kramer} values may be higher than the true

Table 3.3

H^*_{LC} and H^*_{Kramer} (12 K) for Various Binary Wire Reactions

Temperature	Time (Hours)	H^*_{LC} (Tesla)	H^*_{Kramer} (Tesla)
675°C	4	6.5	5.9
	8	6.5	6.2
	16	7.9	7.3
	32	8.6	8.5
	47	9.3	9.4
	64	9.7	9.7
	128	10.0	10.0
	312	9.1	9.6
	512	9.1	9.5
	768	9.2	9.4
750°C	16	10.9	11.0
	32	10.4	10.9
	64	9.8	10.3
	128	9.6	10.3

Table 3.4

H^*_{LC} and H^*_{Kramer} (12 K) for Various Ternary Wire Reactions

Temperature	Time (Hours)	H^*_{LC} (Tesla)	H^*_{Kramer} (Tesla)
675°C	4	7.1	7.1
	8	7.9	8.2
	16	8.9	8.8
	32	9.9	9.9
	64	10.7	10.7
	128	10.9	11.2
	312	11.1	11.2
	768	10.8	11.0
750°C	8	11.2	11.5
	16	11.4	11.8
	32	11.4	11.8
	64	11.4	11.6
	128	11.0	11.3
800°C	8	11.2	11.8
	16	11.2	11.8
	32	11.2	11.7
850°C	8	11.3	12.1

irreversibility field for these reactions. 12 K Kramer fits to curves of ternary strand heat treated at these temperatures are less linear and extrapolate to lower relative fields than strand of the same respective reaction measured at 4.2 K. For example, H^*_{Kramer} of the 8h/800°C ternary reaction extrapolates to 27.7 T at 4.2 K (Figure 3.11), a field over 1 T greater than the H^*_{Kramer} value achieved in the 32h/750°C ternary reaction (26.6 T) at 4.2 K; however, at 12 K, the 8h/800°C and 32h/750°C reactions both extrapolate to H^*_{Kramer} values of 11.8 T (Figure 3.14). Thus, despite the linear behavior of the 4.2 K Kramer curve for the 8h/800°C reaction, it is unlikely that the true irreversibility field at 4.2 K is as high as the Kramer extrapolated value of 27.7 T.

Kramer extrapolations were also performed for the ternary strand receiving elevated temperature heat treatments of 850°C – 1000°C. These results are provided in Appendix B.

3.4 Upper Critical Field

Figure 3.15 shows H^*_{Kramer} and the upper critical field (H_{c2}), measured at 12 K, as a function of heat treatment time for samples reacted at 675°C from 4 to 768 hours. The difference between H_{c2} and H^*_{Kramer} is largest at short heat treatment times but diminishes with increasing time. H_{c2}, for both wires, appears to slightly diminish by the longest reaction times; a result which corresponds to the trend observed in H^*_{Kramer}. It became increasingly difficult to measure H_{c2} near the limits of 14 T in this study, thus results that could not be clearly identified are not shown. It is to be noted that there is always a significant gap between H* and H_{c2}, as shown in earlier studies of Nb_3Sn [50].

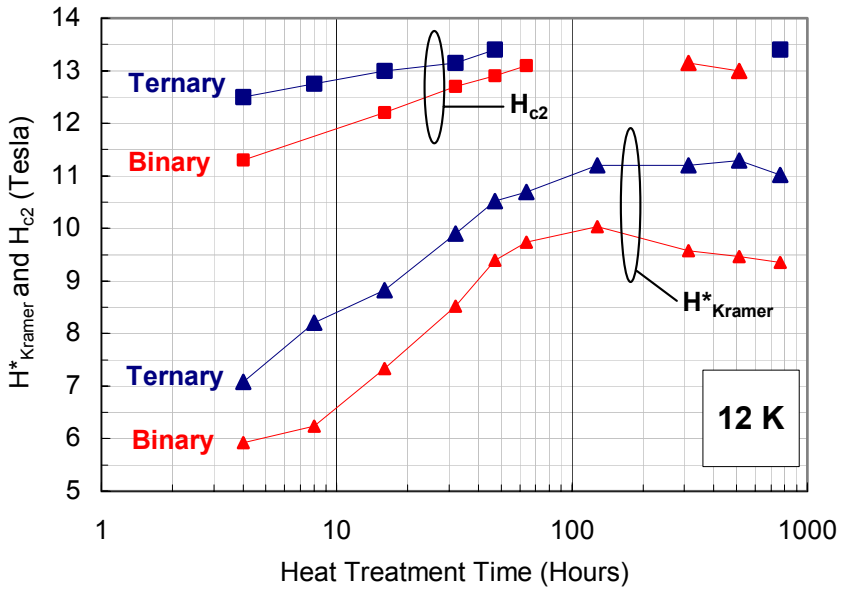

Figure 3.15. Upper critical field (H_{c2}) and irreversibility field (H^*_{Kramer}) versus heat treatment time at 675°C for the binary and ternary wire at 12 K. H_{c2} for some of the reactions could not be identified.

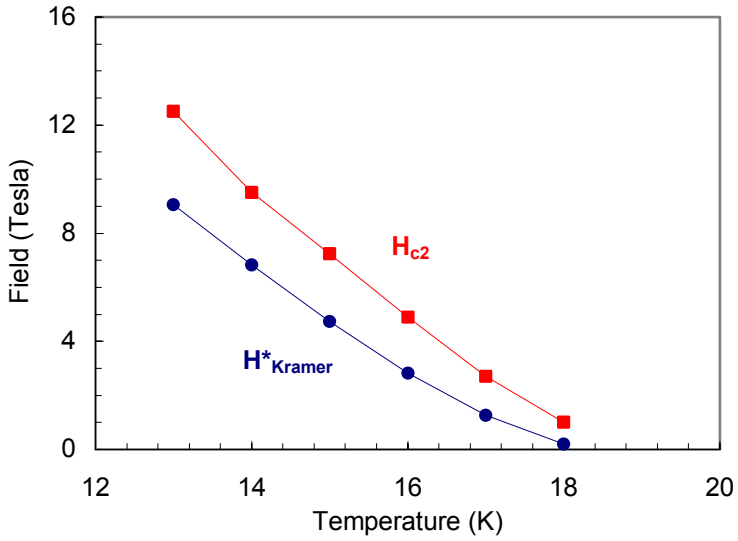

Figure 3.16. Upper critical field (H_{c2}) and irreversibility field (H^*_{Kramer}) versus temperature for the ternary wire reacted at 675°C for 128 hours.

Figure 3.16 illustrates how H_{c2} and H^*_{Kramer} vary as a function of temperature from 13 K to 18 K for a typical ternary reaction of 128h/675°C. The ratio of H_{c2}/H^*_{Kramer} is ~1.4 at 13 K and dH_{c2}/dT is ~2.4 T/K. From Hake [51],

$$H_{c2}(0) \approx 0.69 \cdot T_c \cdot \left.\frac{dH_{c2}}{dT}\right|_{T_c}, \qquad \text{(Tesla)} \qquad (3.1)$$

where T_c is in Kelvin. Assuming stoichiometric Nb_3Sn with a T_c of 18.3 K, Eq. 3.1 extrapolates H_{c2} to ~30 T at 0 K.

3.5 Summary

The critical temperature curves of the Nb_3Sn PIT strand contain two transitions. The higher transition results entirely from the Nb_3Sn phase and the lower transition results entirely from the Nb barrier prior to Nb barrier breakthrough. After Nb barrier breakthrough, the lower transition is created by a combination of Nb and low Sn-content Nb_3Sn, which is no longer shielded by the barrier. As reaction time increases and larger portions of the Nb barrier become completely reacted through, the lower transition shifts to lower temperatures. The higher transition, characteristic of the Nb_3Sn, increases with increasing reaction time and temperature as the Nb_3Sn becomes more homogeneous in composition and the composition gradient across the thickness of the Nb_3Sn layer flattens. The limiting T_c values measured in the binary (17.55 K) and ternary (17.34 K) composites are high compared to values observed in internal-Sn composites produced by the Modified Jelly Role Method, but lower than the value observed in stoichiometric Nb_3Sn (18.3 K).

The irreversibility field as measured by the Kramer function (H^*_{Kramer}) fits the magnetization data quite well showing practically linear data fits for all reactions at 675°C and 750°C. The ternary strand exhibited a significant advantage in H^*_{Kramer} compared to the binary strand for all reactions studied. H^*_{Kramer} increases monotonically with reaction time through 128 hours (23.5 T) for the binary and through 312 hours (25.9 T) for the ternary before diminishing slightly at longer times. This slight decrease at longer times correlates with the onset of Sn breakthrough of the Nb barrier. For 750°C reactions, a significant increase in H^*_{Kramer} is observed as compared to 675°C reactions (~2.4 T advantage in binary and ~1 T advantage in ternary). The relative heights of the Kramer extrapolations correspond

to the difference in J_c for the various reactions. J_c calculations derived from the magnetization data is provided in the next section.

Similarly to H^*_{Kramer}, H_{c2} increases with reaction time for the majority of reactions performed at 675°C and appears to diminish slightly at the longest times, coinciding with the onset of Sn breakthrough of the Nb barrier. A significant gap between H_{c2} and H^* is always present, and is largest at shorter reaction times and diminishes with increasing reaction time. H_{c2} data measured from 12 K through 18 K for the 128h/675°C ternary strand was used to extrapolate H_{c2} at 0 K to ~30 T.

4 Flux Pinning Properties – J_c, F_p and Q_{GB}

4.1 Experimental Approach

The J_c values given in this study were derived from magnetization measurements made with the long axis of the filaments parallel to the applied field. Under these conditions, circumferential currents flow within the Nb_3Sn layers of each filament. The derivation for how J_c was calculated from the magnetization is as follows. From Evetts et al. [52], assuming that the Bean critical state is established in the filament,

$$J_c \ cylinder = \frac{3M}{R}, \tag{4.1}$$

where M is the magnetization of the conductor and R is the filament radius. Since

$$M = \frac{\Delta m}{V}, \tag{4.2}$$

where V is the volume of the filament, approximated as a superconducting cylinder of radius R, Eq. 4.1 can be transformed into

$$J_c \ cylinder = \frac{3\Delta m}{R^3 \pi L}, \tag{4.3}$$

where L is the length of the cylinder. The reacted Nb_3Sn filaments were approximated as cylindrical shells. Thus,

$$A15 \ Layer \ J_c = \frac{3\Delta m}{2f\pi L\left(R_{outer}^3 - R_{inner}^3\right)} \tag{4.4}$$

where f is the number of filaments (in this case 192), R_{outer} is the effective radial distance from the filament core to the interface between the small-grain A15 layer and the Nb and R_{inner} is the effective radial distance from the filament core to the interface between the large-grain A15 layer and the small-grain A15 layer. R_{outer} and R_{inner} are depicted in

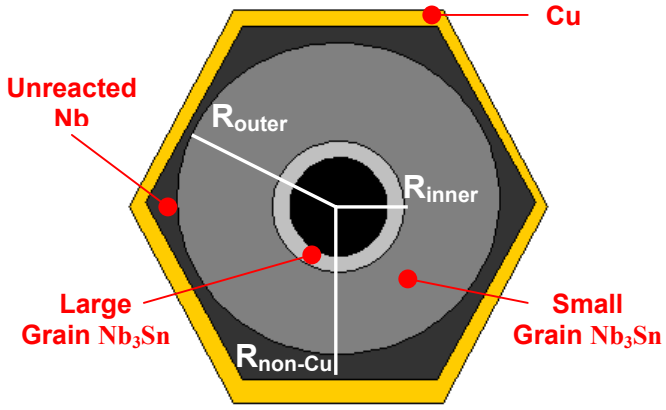

Figure 4.1. A schematic of a Nb_3Sn PIT conductor filament, illustrating the variables R_{outer}, R_{inner} and $R_{non\text{-}Cu}$, which are incorporated into equations 2.4 and 2.5. This schematic is modeled after an actual version shown in Appendix A.

Figure 4.1 and a description of the measurement of these parameters is provided in Appendix A. Thus, A15-layer J_c effectively normalizes current to the small-grain A15 region, excluding the large-grain A15 region and the filament core. The non-Cu J_c was derived from the A15-layer J_c by normalizing the conductor area to the entire Nb tube giving

$$non-Cu\ J_c = \left(\frac{3\Delta m}{2f\pi L\left(R_{outer}^3 - R_{inner}^3\right)}\right)\left(\frac{R_{outer}^2 - R_{inner}^2}{R_{non-Cu}^2}\right), \tag{4.5}$$

where $R_{non\text{-}Cu}$ is the effective radial distance from the filament core to the Cu-Nb interface. $R_{non\text{-}Cu}$ is illustrated in Figure 4.1.

It should be noted that this derivation for J_c from magnetization approximates the critical current in a circumferential direction around the Nb_3Sn filament layers. This differs from a transport measurement in which current is passed along the length of the wire. This derivation assumes that the Nb_3Sn layers are axially homogenous in composition and grain morphology.

A derivation of the voltage criterion used for the magnetization derived J_c values is provided in Appendix C.

4.2 Critical Current Density

Non-Cu critical current density, derived from magnetization measurements, as a function of applied field for the binary and ternary wires is depicted in Figure 4.2 and Figure 4.3, respectively. The trends observed for both the binary and ternary wire reactions are quite similar. At 675°C, non-Cu, package J_c (12 T, 4.2 K) increases monotonically through 128 hours where values of 1,460 A/mm² and 1,775 A/mm² were obtained for the binary and ternary strand, respectively. By the 312h/675°C reaction a decrease in non-Cu J_c is observed and continues through the longest 675°C reaction of 768 hours. Non-Cu J_c (12 T, 4.2K) as a function of heat treatment time for binary and ternary strand reacted at 675°C is shown in Figure 4.4. This figure plots the data referred to in the legends of Figure 4.2 and Figure 4.3.

A decrease in non-Cu, package J_c is also observed for increasing reaction temperatures beyond 675°C. Binary wire reactions of 16h/750°C and 32h/750°C achieved non-Cu J_c (12 T, 4.2 K) values of 1,095 A/mm² and 1,090 A/mm², respectively; while ternary wire reactions of 32h/750°C and 64h/800°C achieved non-Cu J_c (12 T 4.2 K) values of 1,040 A/mm² and 710 A/mm², respectively.

The lone transport non-Cu J_c measurement for the wires investigated in this study was performed on the 64h/675°C ternary sample [42]. The non-Cu transport J_c (12 T, 4.2 K) measurement for this specimen was ~20% higher than the magnetization derived non-Cu J_c value obtained in this study (2160 A/mm² and 1,680 A/mm², respectively). For this reason, the J_c values presented in this report are expected to be underestimates of transport J_c. It is

believed that this underestimation arose from the non-uniform thickness of the Nb_3Sn layers, which were discussed in section 2.3. Thus, the induced currents, flowing circumferentially within the Nb_3Sn layers of each filament, may be traveling in smaller Nb_3Sn regions than estimated.

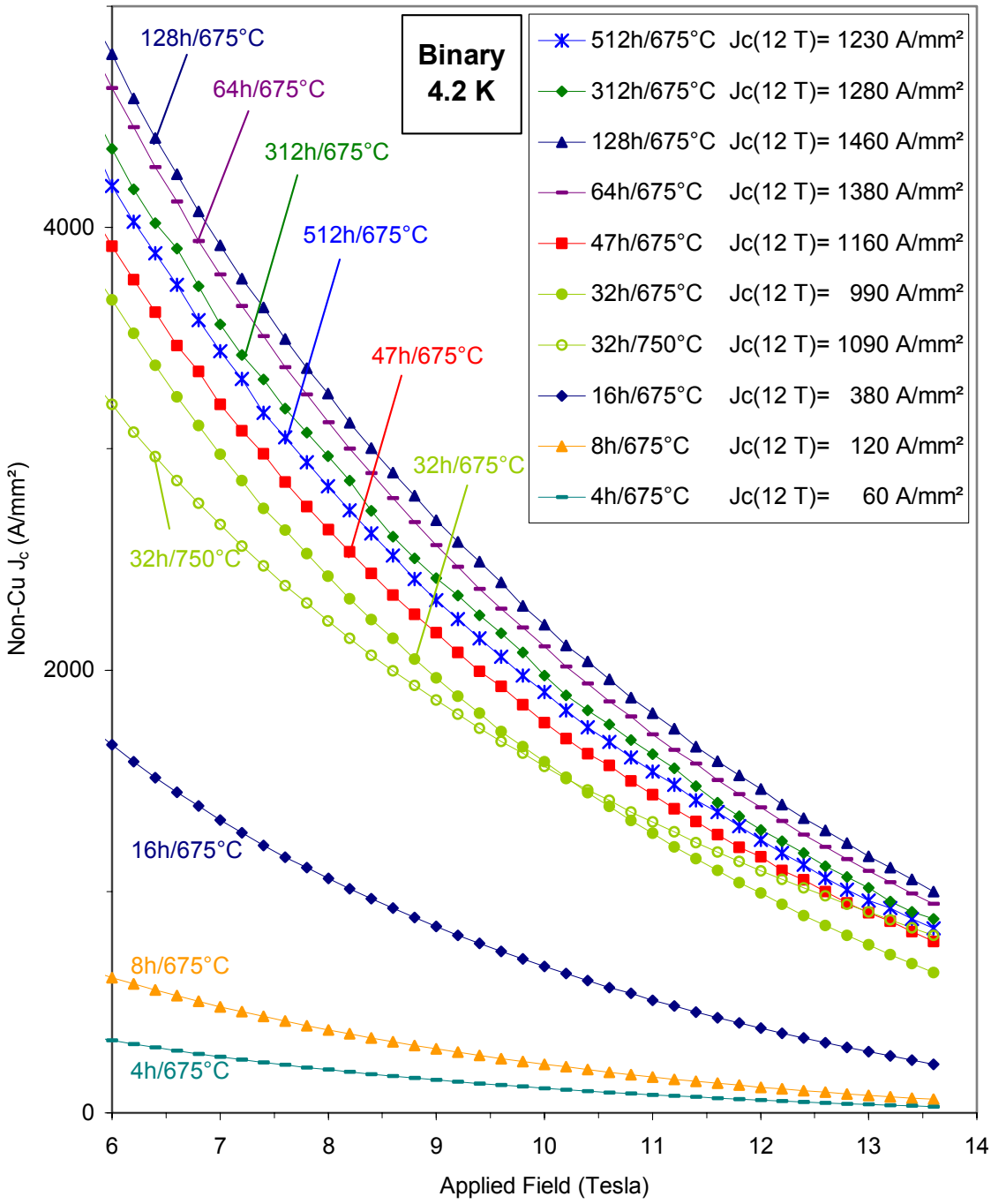

Figure 4.2. Non-Cu J_c, derived from magnetization measurements at 4.2 K of the binary wire, for various heat treatment reactions. Non-Cu J_c (12 T) increases monotonically with increasing time through 128 hours at 675°C. Non-Cu J_c (12 T) diminishes for increasing times greater than 312 hours, at 675°C, and for increasing temperatures greater than 750°C.

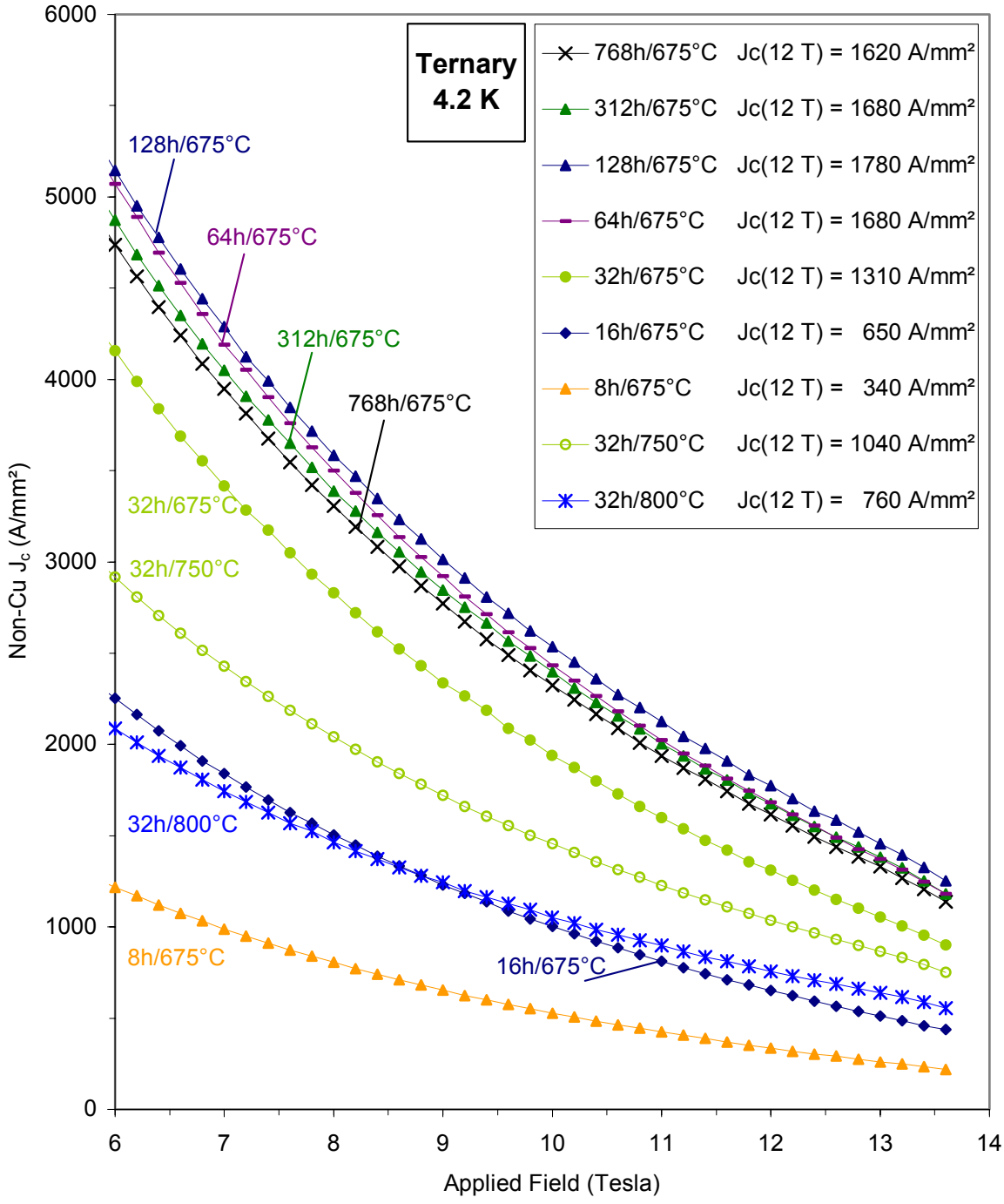

Figure 4.3. Non-Cu J_c, derived from magnetization measurements at 4.2 K of the ternary wire, for various heat treatment reactions. Non-Cu J_c (12 T) increases monotonically with increasing time through 128 hours at 675°C. Non-Cu J_c (12 T) diminishes for increasing times greater than 312 hours, at 675°C, and for increasing temperatures greater than 750°C.

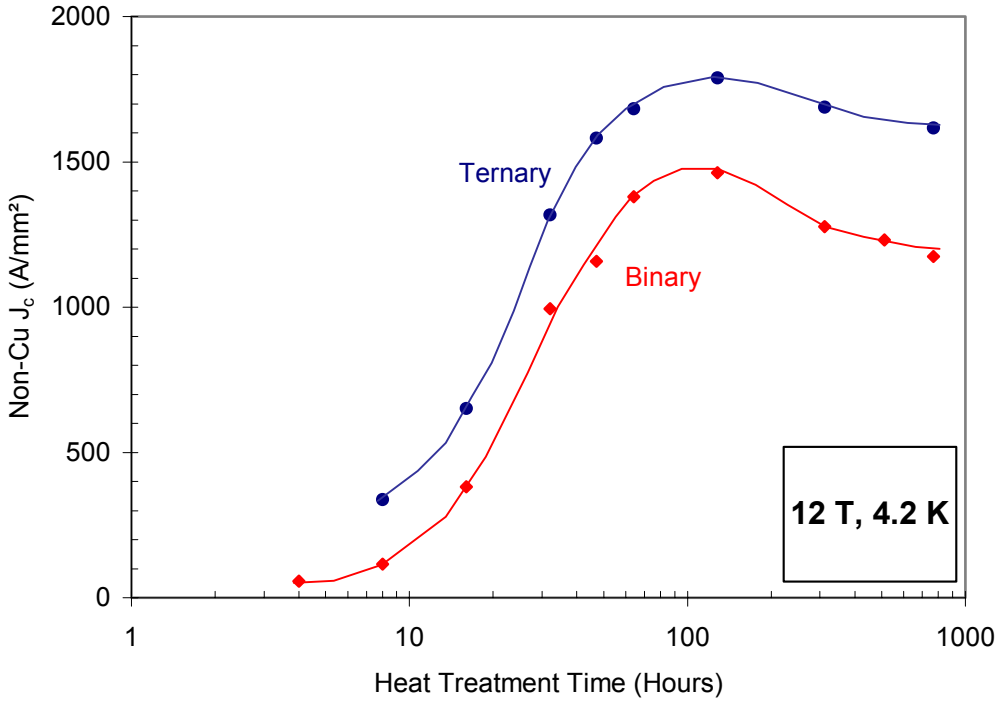

Figure 4.4. Non-Cu J_c values, derived from magnetization measurements at 12 T, 4.2 K, for binary and ternary wire versus heat treatment time at 675°C. The measurements are those referred to in the legends of Figure 4.2 and Figure 4.3.

A15-layer J_c (4.2 K), derived from magnetization measurements, as a function of applied field for the binary and ternary strand is depicted in Figure 4.5 and Figure 4.6, respectively. For the binary wire reaction at 675°C, A15-layer J_c (12 T, 4.2 K) reaches a maximum value of 3,440 A/mm² after 128 hours and declines to 2,880 A/mm² after 512 hours. The A15-layer J_c (12 T, 4.2 K) of the ternary strand exhibits a similar trend for the series of reactions at 675°C, where A15-layer J_c is maximized at 4,280 A/mm² after 64 hours and diminishes to 3,460 A/mm² after 768 hours. A15-layer J_c (12 T, 4.2K) as a function of heat treatment time for binary and ternary strands reacted at 675°C are shown in Figure 4.7. This figure is a plot of the data referred to in the legends of Figure 4.5 and Figure 4.6.

Similar to non-Cu, package J_c, a decrease in A15-layer J_c was observed for temperatures greater than 675°C. A reaction of 32h/750°C in the binary wire produced an A15-layer J_c (12 T, 4.2 K) of 2,580 A/mm², a 25% decline from the maximum at 675°C. Reactions of 32h/750°C and 64h/800°C in the ternary wire achieved A15-layer J_c (12 T, 4.2 K) values of 2,420 A/mm² and 1,860 A/mm², respectively, approximately 50% declines from the maximum at 675°C.

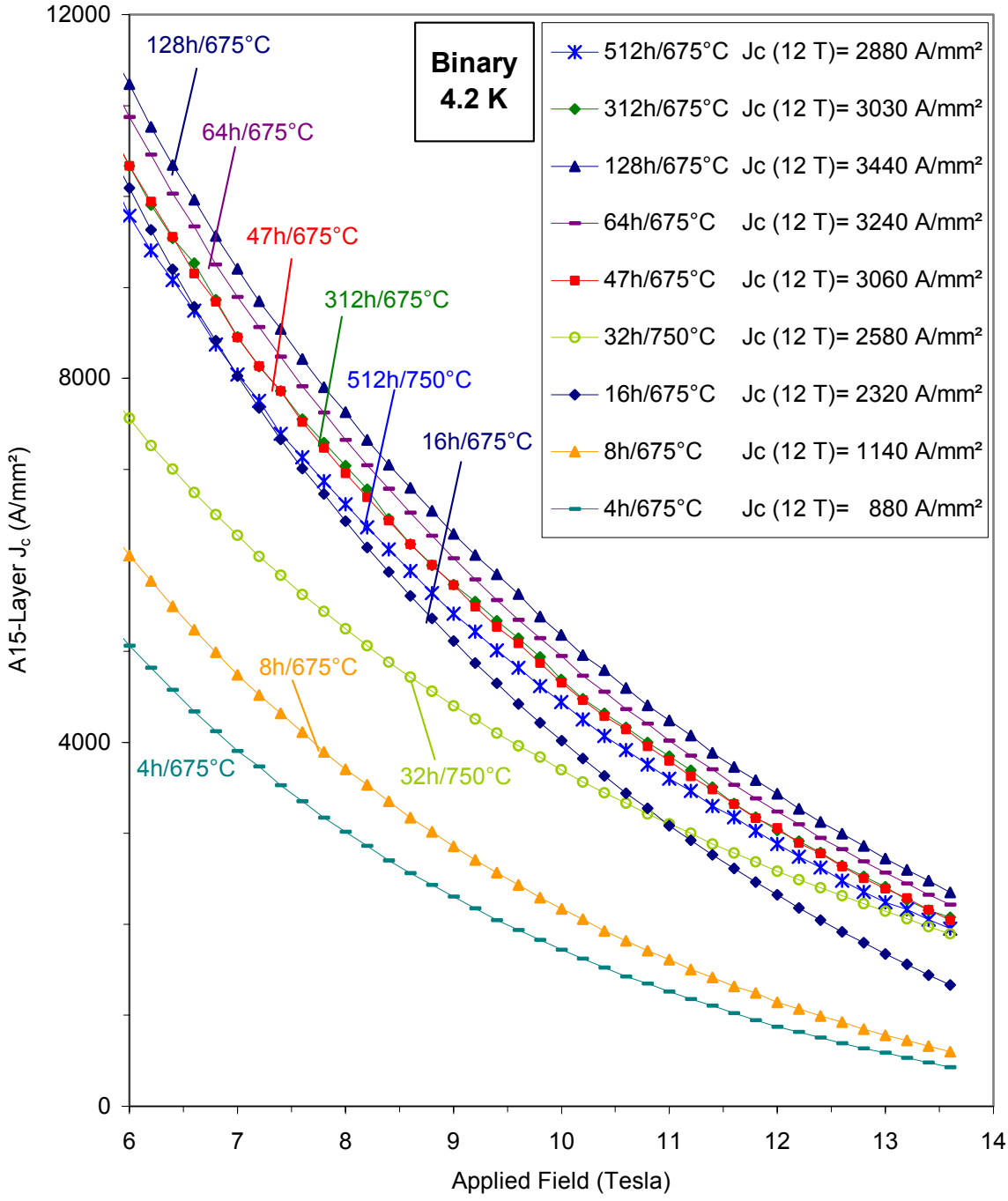

Figure 4.5. A15-Layer J_c, derived from magnetization measurements at 4.2 K of the binary wire, for various heat treatment reactions. A15-Layer J_c (12 T) increases monotonically with increasing time through 128 hours at 675°C. A15-Layer J_c (12 T) diminishes for increasing times greater than 312 hours, at 675°C, and for increasing temperatures greater than 750°C.

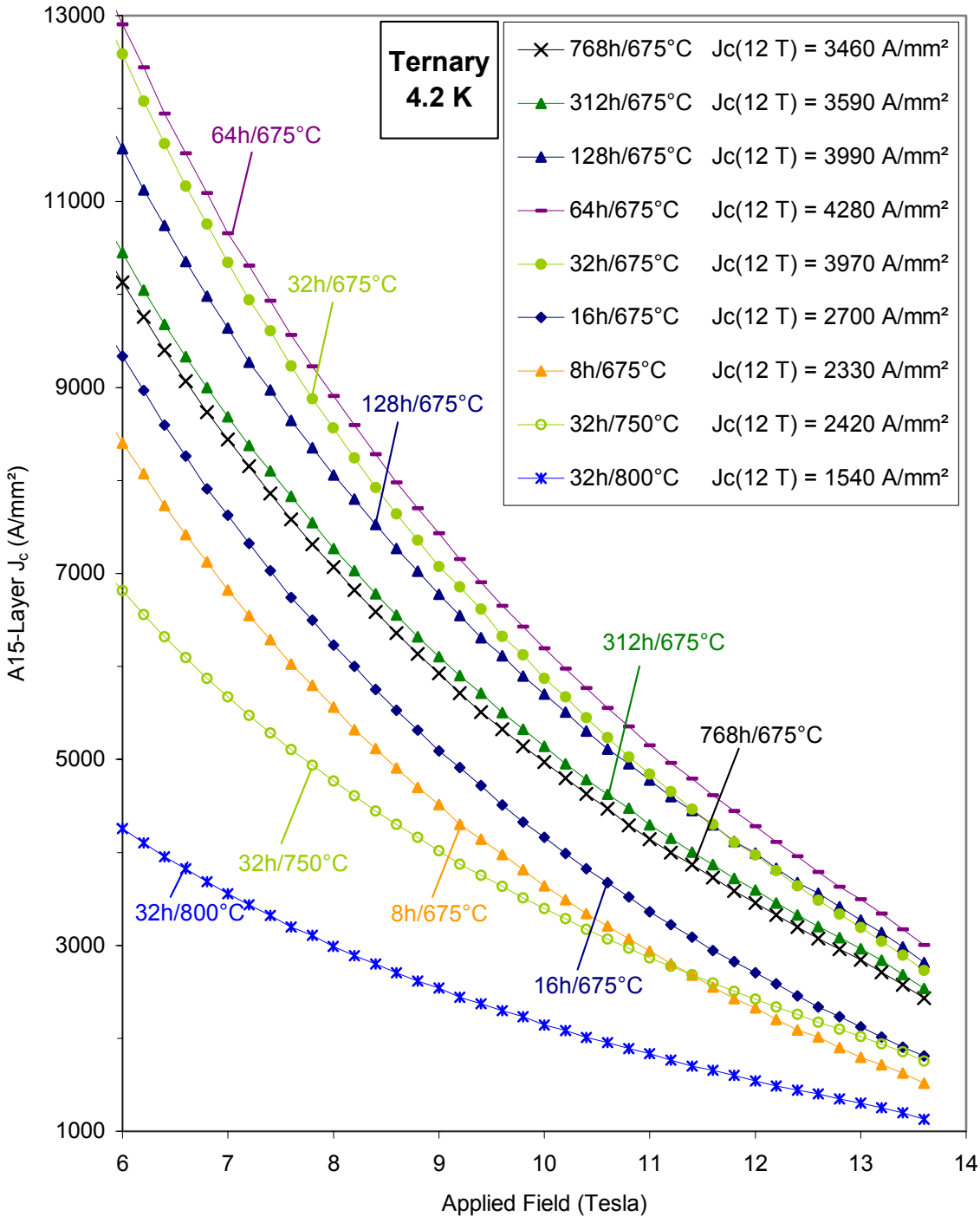

Figure 4.6. A15-Layer J_c, derived from magnetization measurements at 4.2 K of the ternary wire, for various heat treatment reactions. A15-Layer J_c (12 T) increases monotonically with increasing time through 64 hours at 675°C. A15-Layer J_c (12 T) diminishes for increasing times greater than 128 hours, at 675°C, and for increasing temperatures greater than 750°C.

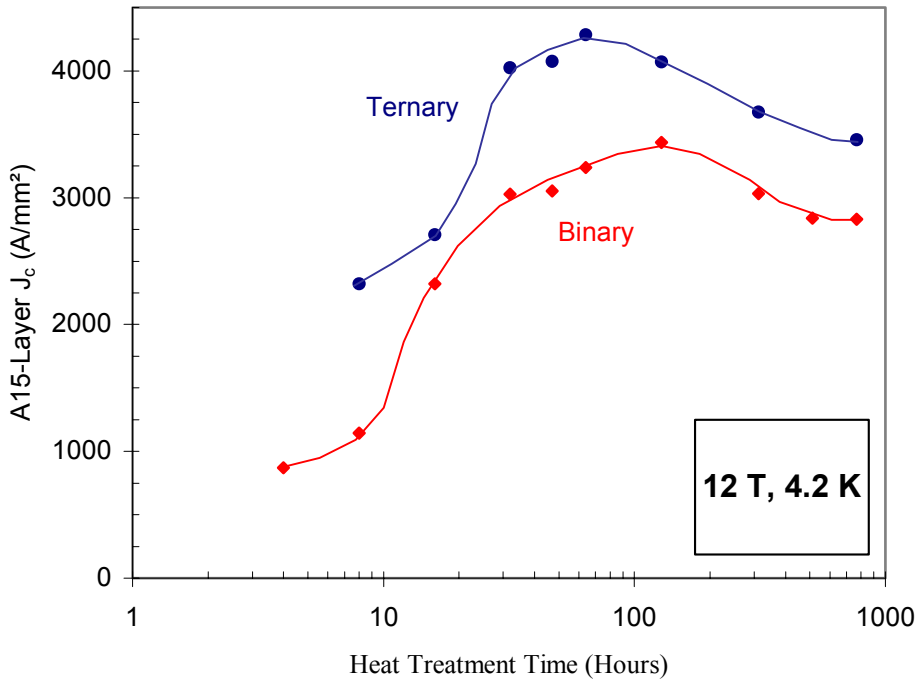

Figure 4.7. A15-Layer J_c values, derived from magnetization measurements at 12 T, 4.2 K, for binary and ternary wire versus heat treatment time at 675°C. The measurements are those referred to in the legends of Figure 4.6 and Figure 4.7.

We observe, as did Veringa et al. [53], the formation of large (>500 nm) A15 grains on the inside of the A15 layer, adjacent to the core after 32h/675°C and 16h/675°C for the binary and ternary wire, respectively. The exact contribution of these grains to Δm is unclear, however it is suspected that the grains do not offer any substantial contribution to flux pinning compared to the fine grains occupying the majority of the A15 layer where the grain size is orders of magnitude smaller (Figure 2.2 and Figure 2.3). For this reason, the larger grained A15 region was excluded from the calculation of A15-layer J_c.

4.3 Flux Pinning

Bulk flux pinning (F_p) forces as a function of applied field for the binary and ternary strands are depicted in Figure 4.8 - Figure 4.15. F_p curves were calculated from the non-Cu,

package, J_c values (Figure 4.8 - Figure 4.11) and the A15-layer J_c values (Figure 4.12 - Figure 4.15) given in section 3.4, where $F_p = J_c \times B$. As a result, several of the trends evident from the Kramer plots and J_c curves (derived from magnetization measurements) are also apparent in the flux pinning curves. For example, how $F_{p\text{-}max}$ and F_p (12 T, 4.2 K) change as a function of reaction time, at 675°C, illustrated in Figure 4.16 and Figure 4.17, respectively. In fact, the shape of the curves, depicting flux pinning data, in Figure 4.17 are very similar to the $J_c(B)$ curves in Figure 4.4 and Figure 4.7.

For the binary strand, maximum values for non-Cu and A15-layer $F_{p\text{-}max}$ (4.2 K) were 29.5 GN/m³ and 69.2 GN/m³, respectively, after 128h/675°C. The ternary strand achieved maximum non-Cu and A15-layer $F_{p\text{-}max}$ (4.2 K) values of 31.3 GN/m³ and 78.9 GN/m³ after 128h/675°C and 64h/675°C, respectively. Most F_p data in the literature is derived from non-Cu J_c data, however the derivation of F_p from A15-layer J_c data is more representative of the true flux pinning in the superconductor. Both data sets are included in this study.

The legends of Figure 4.8 - Figure 4.15 indicate the field B_{max} at which $F_{p\text{-}max}$ occurs. For both the binary and ternary strands reacted at 675°C, the location of $F_{p\text{-}max}$ increases to higher fields with increasing reaction time, however this increase is less than 1.5 T over the entire range of heat treatments performed. For the binary strand, the 4h/675°C and 312h/675°C reactions produced $F_{p\text{-}max}$ values at 3.4 T and 4.2 T, respectively. The 32h/750°C heat treatment achieved an $F_{p\text{-}max}$ value at 4.8 T, 0.6 T higher than the maximum $F_{p\text{-}max}$ field at 675°C. For the ternary strand, the 8h/675°C and 128h/675°C reactions achieved $F_{p\text{-}max}$ values at 4.2 T and 5.2 T, respectively. However, the locations of $F_{p\text{-}max}$ for reactions of 32h/750°C and 64h/800°C were 4.8 T and 5.0 T, respectively; not any greater than the maximum observed at 675°C.

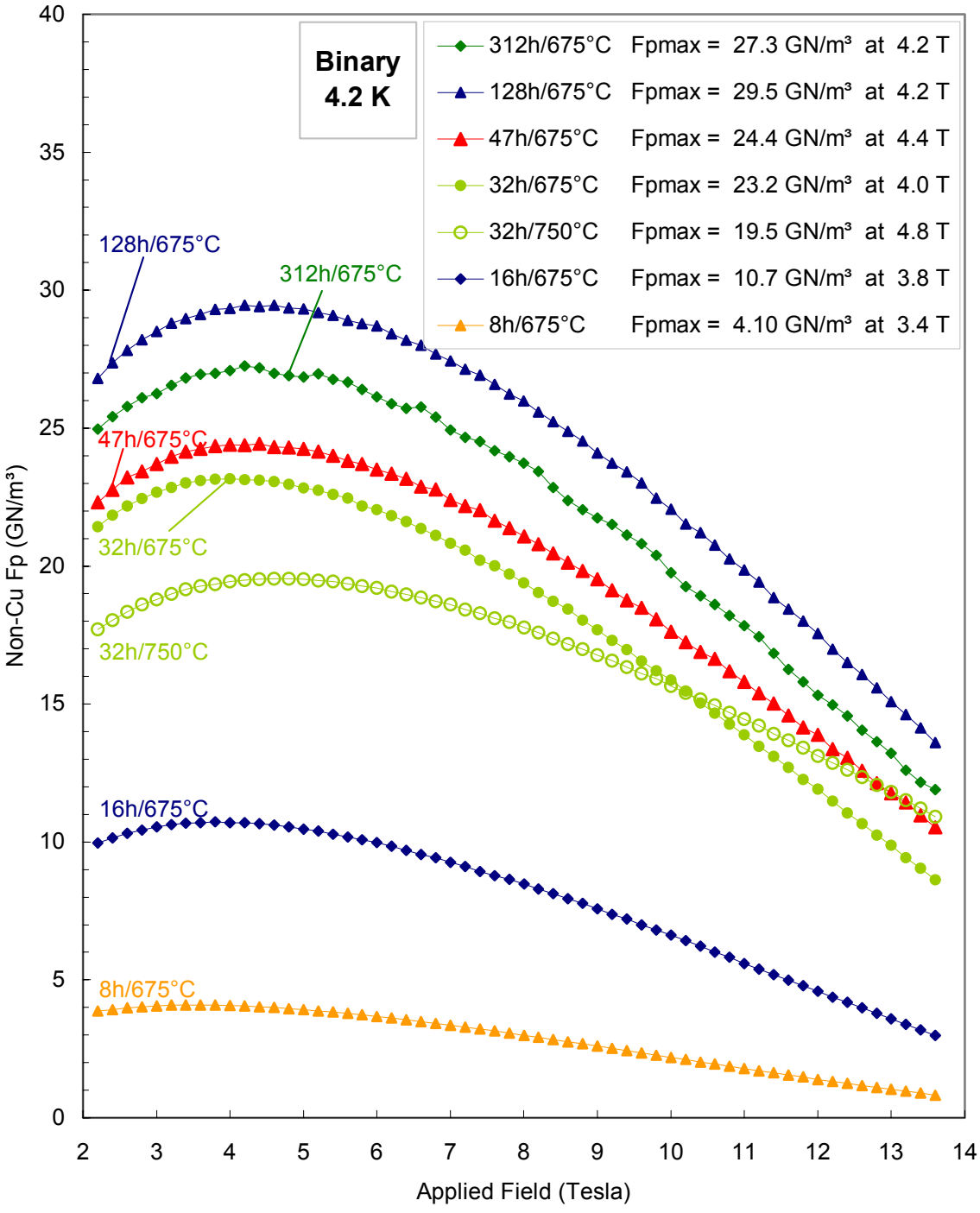

Figure 4.8. Flux pinning curves of the binary strand, obtained at 4.2 K, for various heat treatments. F_p was calculated from the non-Cu J_c values ($J_{c\ non\text{-}Cu} \cdot B$) of the strand, which were derived from magnetization measurements.

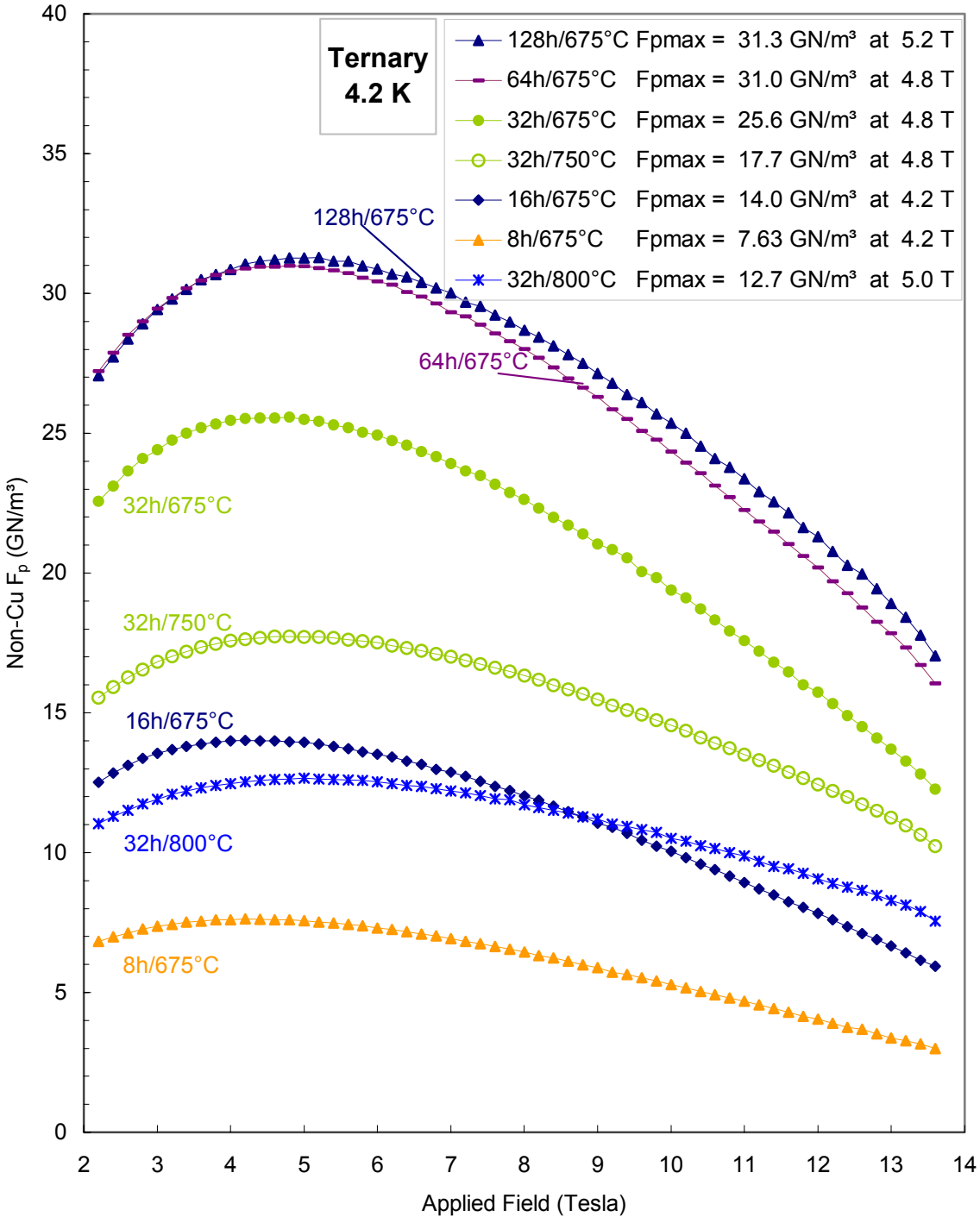

Figure 4.9. Flux pinning curves of the ternary strand, obtained at 4.2 K, for various heat treatments. F_p was calculated from the non-Cu J_c values ($J_{c\ non\text{-}Cu} \cdot B$) of the strand, which were derived from magnetization measurements.

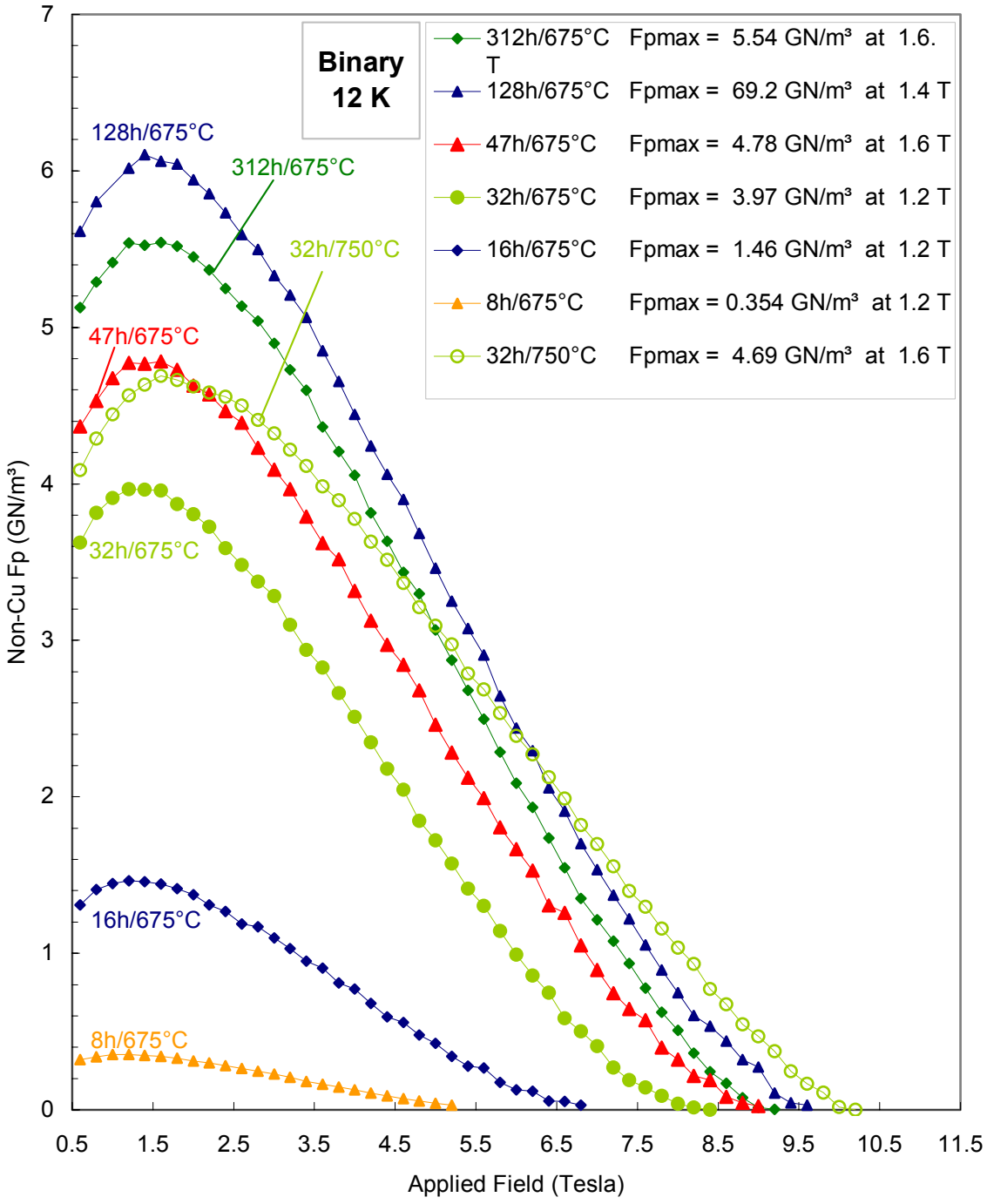

Figure 4.10. Flux pinning curves of the binary strand, obtained at 12 K, for various heat treatments. F_p was calculated from the non-Cu J_c values ($J_{c\ non\text{-}Cu} \cdot B$) of the strand, which were derived from magnetization measurements.

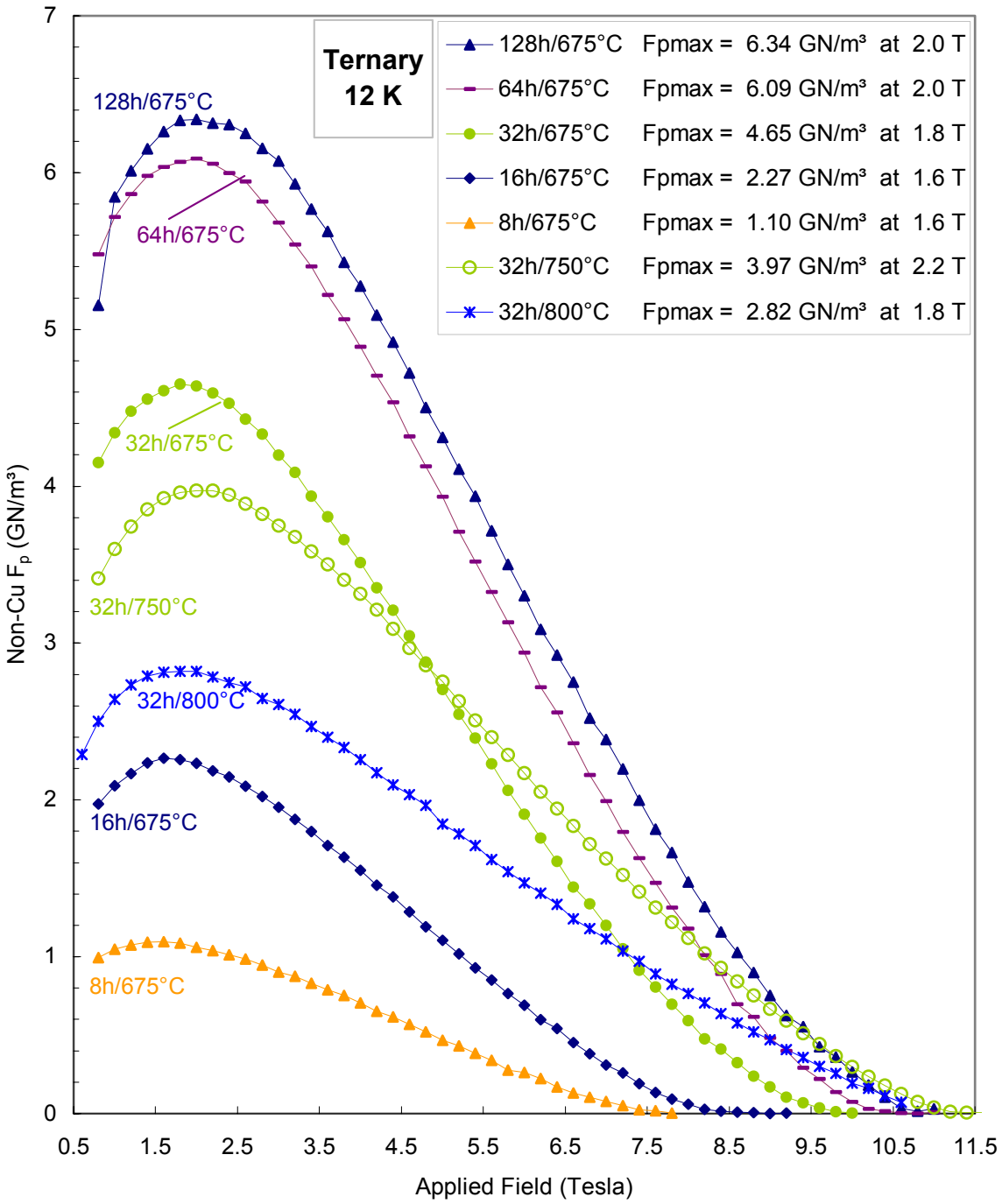

Figure 4.11. Flux pinning curves of the ternary strand, obtained at 12 K, for various heat treatments. F_p was calculated from the non-Cu J_c values ($J_{c\ non\text{-}Cu} \cdot B$) of the strand, which were derived from magnetization measurements.

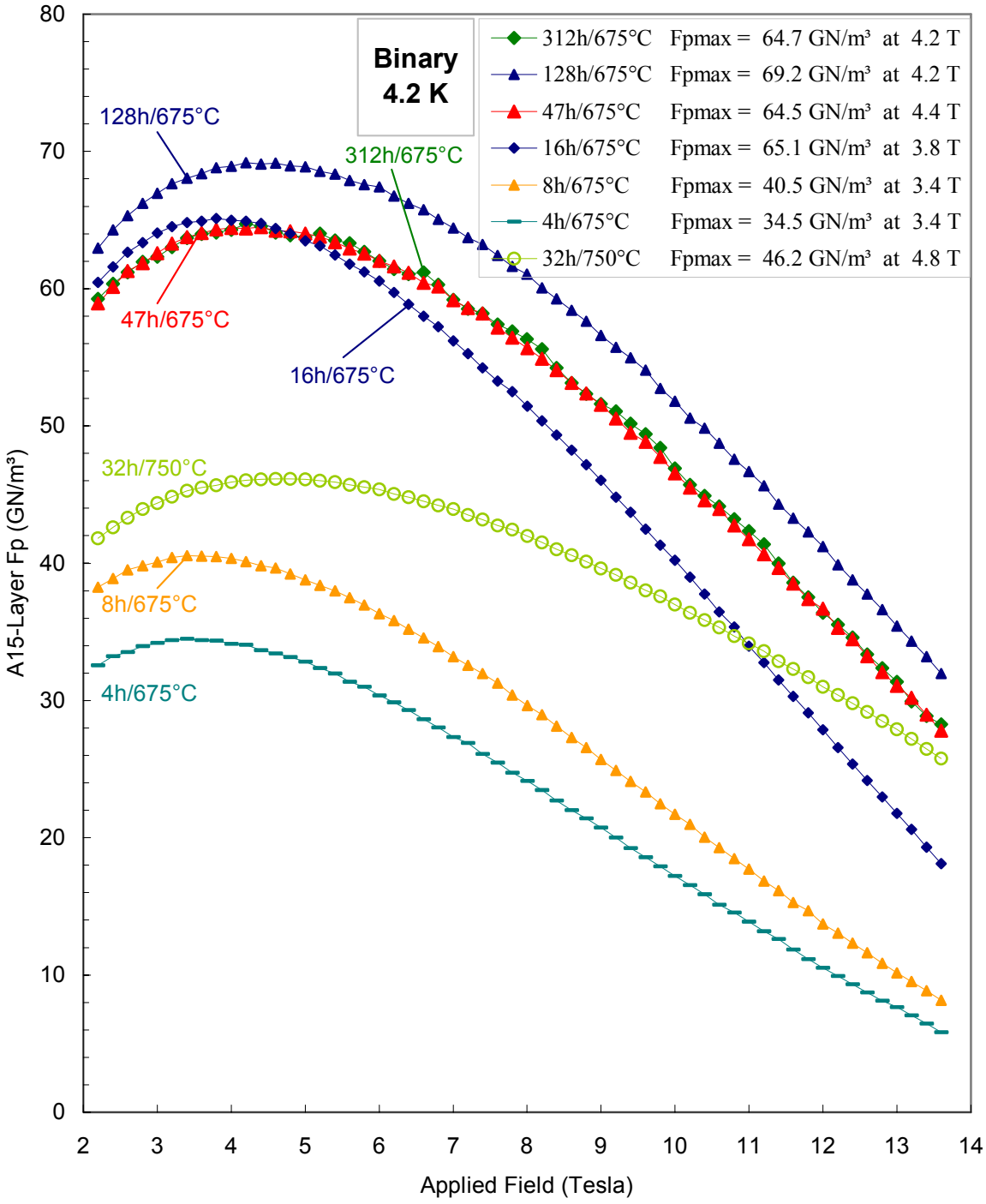

Figure 4.12. Flux pinning curves of the binary strand, obtained at 4.2 K, for various heat treatments. F_p was calculated from the A15-Layer J_c values ($J_{c\ A15} \cdot B$) of the strand, which were derived from magnetization measurements.

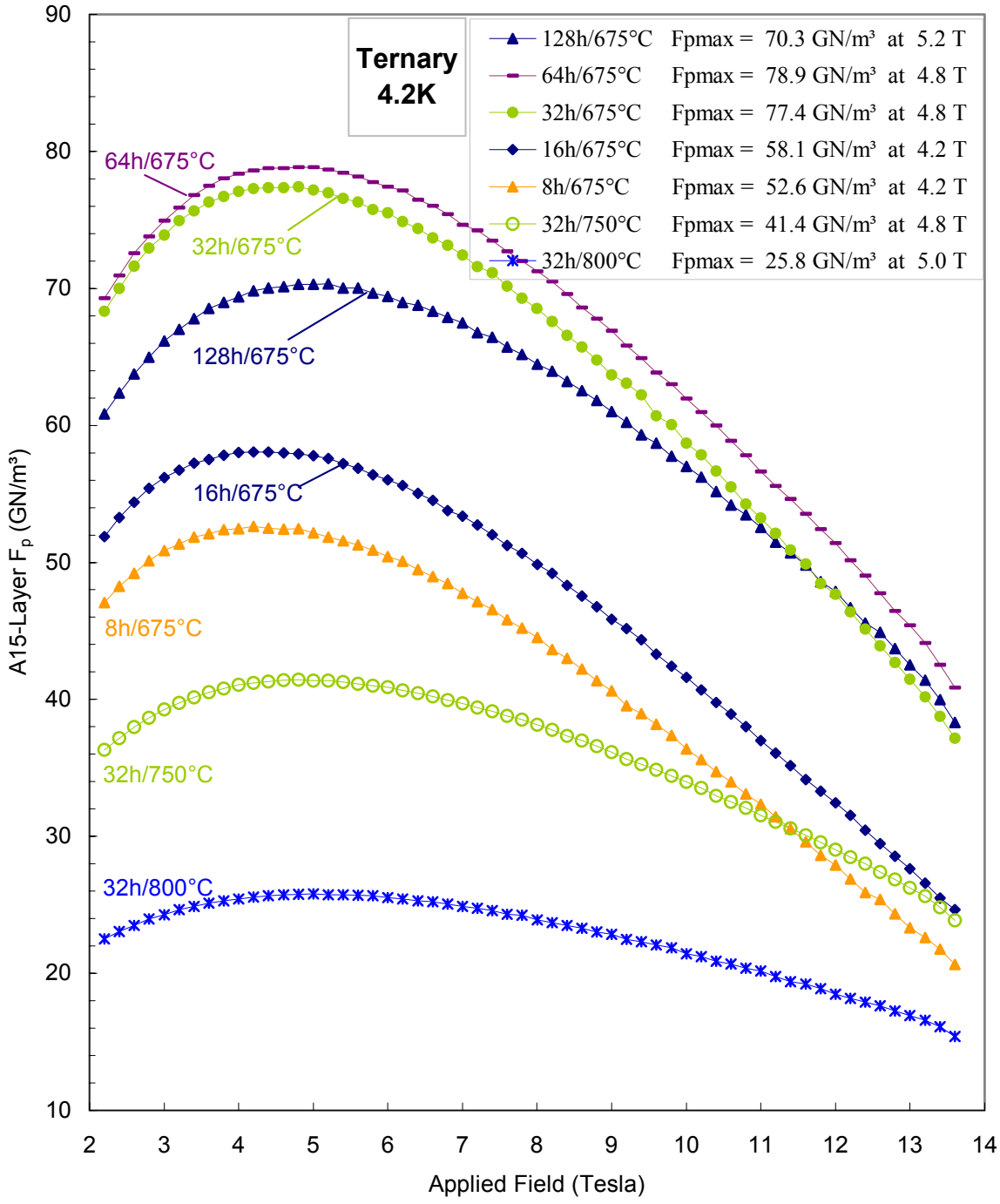

Figure 4.13. Flux pinning curves of the ternary strand, obtained at 4.2 K, for various heat treatments. F_p was calculated from the A15-layer J_c values ($J_{c\ A15} \cdot B$) of the strand, which were derived from magnetization measurements.

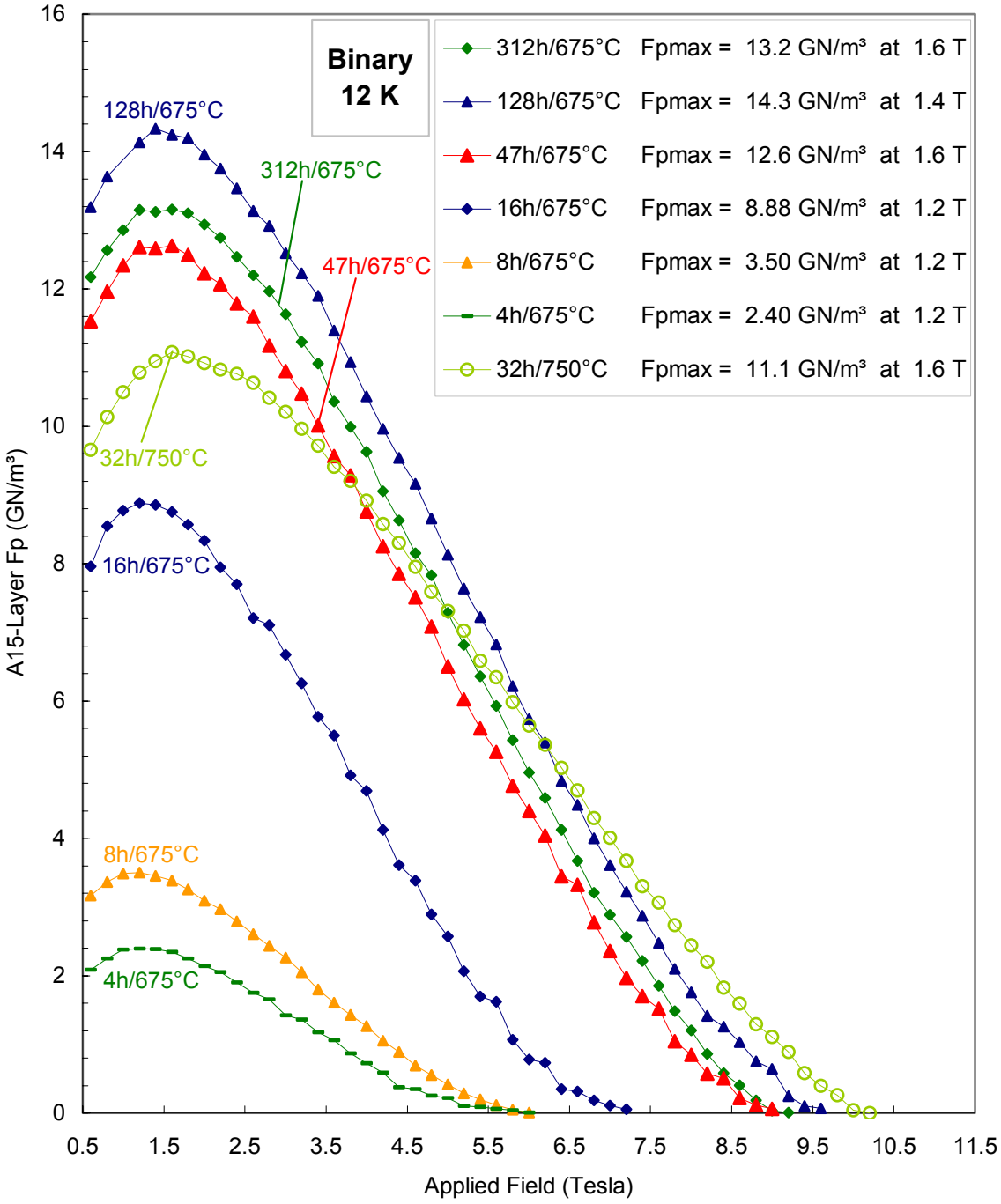

Figure 4.14. Flux pinning curves of the binary strand, obtained at 12 K, for various heat treatments. F_p was calculated from the A15-layer J_c values ($J_{c\ A15} \cdot B$) of the strand, which were derived from magnetization measurements.

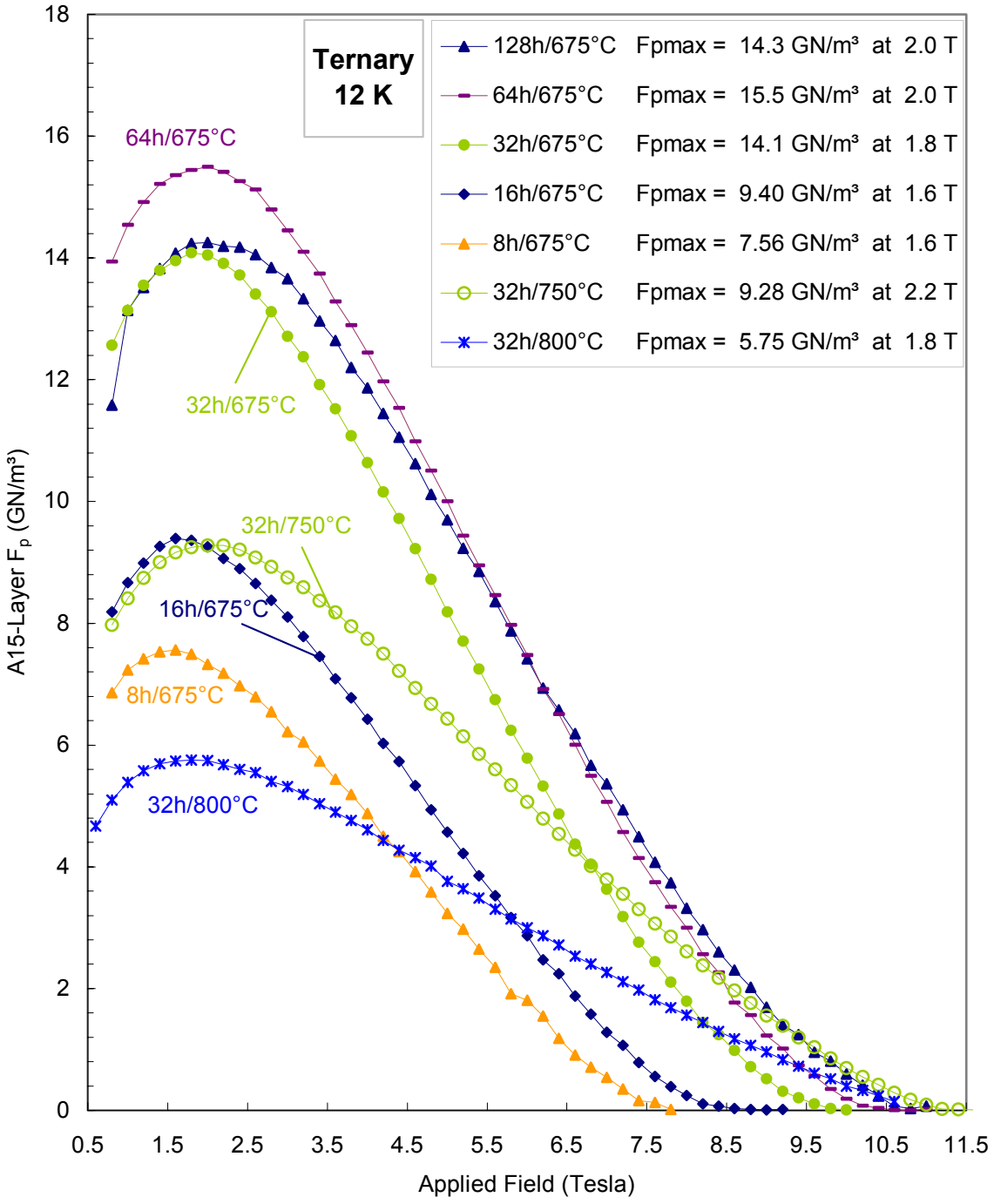

Figure 4.15. Flux pinning curves of the ternary strand, obtained at 12 K, for various heat treatments. F_p was calculated from the A15-layer J_c values ($J_{c\ A15} \cdot B$) of the strand, which were derived from magnetization measurements.

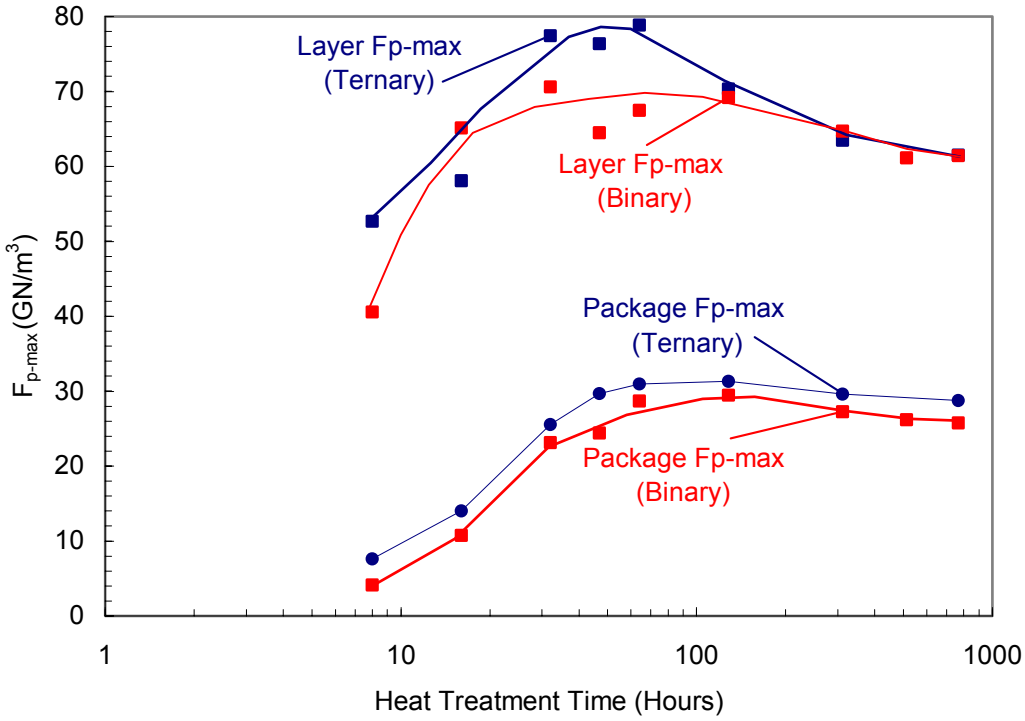

Figure 4.16. Maximum flux pinning values (4.2 K) as a function of reaction time for binary and ternary strand heat treated at 675°C. $F_{p\text{-}max}$ values calculated from both layer-J_c and non-Cu, package J_c measurements are shown. The values plotted are those referred to in the legends of Figure 4.8, Figure 4.9, Figure 4.12 and Figure 4.13.

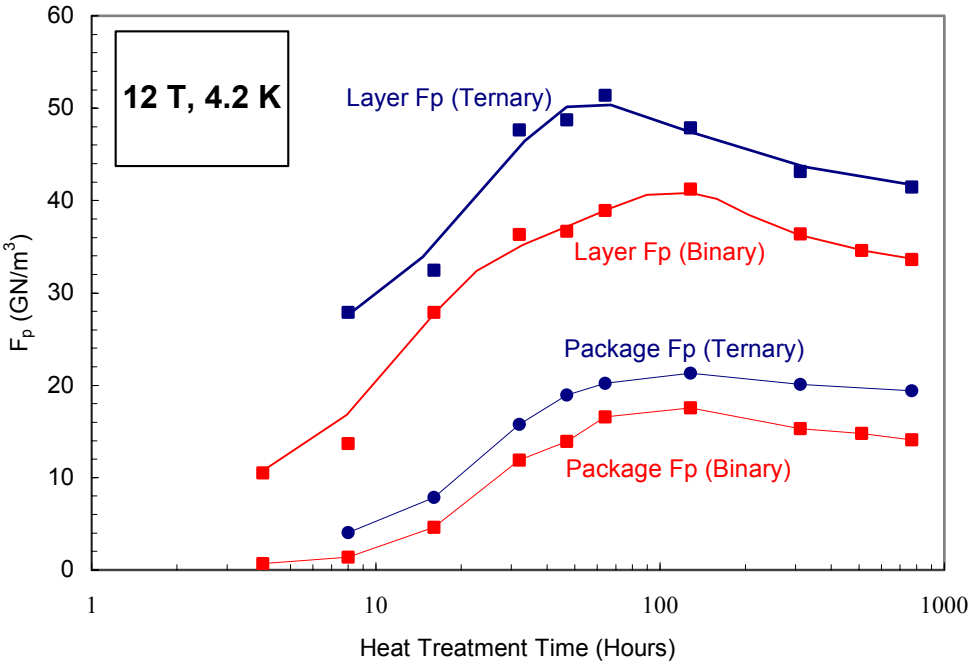

Figure 4.17. Flux pinning values (12 T, 4.2 K) as a function of reaction time for binary and ternary strand heat treated at 675°C. F_p values calculated from both layer-J_c and non-Cu, package J_c measurements are shown. The values plotted are those shown at 12 T in Figure 4.8, Figure 4.9, Figure 4.12 and Figure 4.13.

4.4 Elementary Pinning Force

Elementary pinning force (Q_{GB}) values for the binary and ternary strand are plotted in Figure 4.18 as a function of reaction time at 675°C. Q_{GB} is calculated by the following equation:

$$Q_{GB} = \left(\frac{1}{\eta}\right)\left(\frac{F_p}{GB_{l/A}}\right), \tag{4.6}$$

where η is the efficiency factor, assumed to be 1/3 for the equiaxed grains found in this study and $GB_{l/A}$ is the grain boundary length per area (Table 2.2 and Table 2.3). Thus, Q_{GB} is a measure of the effective pinning of a grain boundary in the A15 layer. For the binary and ternary wire, $Q_{GB\text{-}max}$ and Q_{GB} (12 T, 4.2 K) increase with reaction time at 675°C through

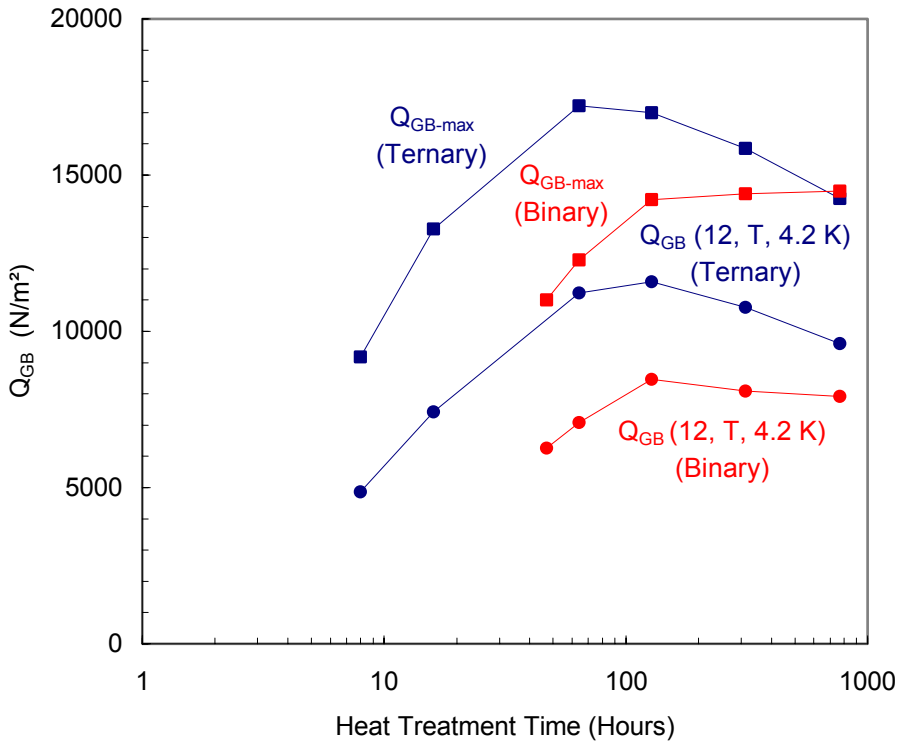

Figure 4.18. Elementary flux pinning (Q_{GB}) values versus reaction time for binary and ternary strand heat treated at 675°C. $Q_{GB\text{-}max}$ and Q_{GB} (12 T, 4.2 K) were calculated from the A15-layer $F_{p\text{-}max}$ and A15-layer F_p (12 T, 4.2 K) values, respectively.

Table 4.1

$Q_{GB\text{-}max}$ and Q_{GB} (12 T, 4.2 K) for Various Binary Wire Reactions

Temperature	Time (Hours)	$Q_{GB\text{-}max}$ (N/m²)	Q_{GB} (12 T, 4.2 K) (N/m²)
675°C	47	11000	6300
	64	12300	7100
	128	14200	8500
	312	14400	8100
	768	14500	7900
750°C	32	19400	13000

approximately 128 hours. Maximum $Q_{GB\text{-}max}$ values of 14,500 N/m² and 17,200 N/m² were achieved for the binary and ternary conductor at 675°C, respectively. For times greater than 128 hours Q_{GB} is fairly uniform in the binary strand. By contrast, significant declines are observed as reaction time is extended beyond 128 hours in the ternary strand. In addition to the values given in Figure 4.18, Table 4.1 and Table 4.2 also list Q_{GB} values obtained for temperatures greater than 675°C. Increases in Q_{GB} are observed for both the binary and ternary at 750°C compared to reactions at 675°C. As reaction temperature is increased further to 800°C the ternary exhibits a decrease in Q_{GB}.

Table 4.2

$Q_{GB\text{-}max}$ and Q_{GB} (12 T, 4.2 K) for Various Ternary Wire Reactions

Temperature	Time (Hours)	$Q_{GB\text{-}max}$ (N/m²)	Q_{GB} (12 T, 4.2 K) (N/m²)
675°C	8	9200	4900
	16	13300	7400
	64	17200	11200
	128	17000	11600
	312	15800	10800
	768	14200	9600
750°C	16	23500	16600
	32	18200	12700
	64	14000	9600
800°C	16	16100	11700
	32	15300	10900

4.5 Summary

Non-Cu and A15-layer J_c values were derived from the magnetization measurements presented in section 3.3. Non-Cu J_c (12 T, 4.2 K) for the binary and ternary strand reacted at 675°C increases monotonically with reaction time through 128 hours, attaining values of 1,460 A/mm² and 1,775 A/mm², respectively. A15-layer J_c (12 T, 4.2 K) increases monotonically with reaction time through 128 hours in the binary (3440 A/mm²) and 64 hours in the ternary (4280 A/mm²). Significant decreases in non-Cu and A15-layer J_c were observed for reactions at temperatures of 750°C and greater. The lone transport non-Cu J_c measurement performed on a wires reacted in this study measured ~20% higher than the magnetization derived J_c value (2160 A/mm² and 1,680 A/mm², respectively), and it is believed that this underestimation arose from the non-uniform thickness of the Nb_3Sn layers.

The F_p curves exhibited similar trends as those presented in the $J_c(B)$ plots. For reactions at 675°C, F_p increased monotonically with reaction time before diminishing slightly at longer times greater than 128 hours, and F_p is reduced significantly with increasing reaction temperature above 675°C. A ~1 T shift in the F_p curves to higher fields was observed in both composites for increasing reaction times at 675°C.

The elementary pinning force (Q_{GB}) was calculated from the F_p data presented in section 4.3 and the grain boundary density data presented in section 2.3. For the binary and ternary strand reacted at 675°C, Q_{GB} (12 T, 4.2 K) increases monotonically through 128 hours and declines by ~5% (binary) and ~15% (ternary) after 768 hours. Additional increases in Q_{GB} of ~35% for reactions at 750°C were observed in both composites compared to the maximum values obtained at 675°C.

J_c, F_p and Q_{GB} for both composites all exhibit declines after longer reaction times at 675°C. These declines coincide with observance of over reaction of the Nb barrier resulting in Sn breakthrough and Nb_3Sn grain size increases of ~20% in the binary and ~5% in the ternary for reaction times of 128 hours through 768 hours at 675°C (Table 2.2 and Table 2.3).

5 Discussion

5.1 Initial Nb_3Sn Formation

High–Sn content A15 is produced very rapidly during the formation of Nb_3Sn as evidenced by H_{c2} values of 11.3 T and 12.5 T (12 K) observed after 4h/675°C reactions in the binary and ternary composites, respectively (Figure 3.15). This result agrees with those of Hawes et al. [33], in which they were able to confirm the presence of high-T_c A15, after 4h/675°C, through both EDX and inductive critical temperature measurements. Considering that H_{c2} values of 12.9 T (binary) and 13.4 T (ternary) were obtained for the 47h/675°C reactions, the H_{c2} values observed after only four hours of reaction are remarkably high. Due to the nature of the magnetization measurement, H_{c2} values are representative of the highest H_{c2} material in the wire because they are characterized by the field at which the highest H_{c2} material loses its diamagnetic superconducting properties. By contrast, H^*_{Kramer} values are defined by the field at which no macroscopic bulk current can be detected, a property therefore determined by the connectivity of the sample, and thus at least partially by the average quality A15 material.

The A15 layer is effectively composed of numerous shells of variable composition. The high Sn-content shells are located in the innermost regions of the A15 layer and the low Sn-content shells are located in the outermost regions. As observed by Hawes et al. and also in the T_c plots for the samples in this study, extending the reaction time flattens the composition and T_c gradient across the A15 layer and diminishes the difference in Sn-content between each of these shells. The derived H^*_{Kramer} is thus an integrated average of the moment in each shell of variable composition. H^*_{Kramer} is relatively low (5.9 T and 7.1 T (12 K) in the

binary and ternary, respectively) after 4h/675°C as compared to values of 10.0 T (binary, Figure 3.13) and 11.2 T (ternary, Figure 3.14) observed after a more complete reaction of 128h/675°C.

Like H^*_{Kramer}, the T_c values given in this study are also representative of the "average" quality Nb_3Sn phase, as they are characterized by the midpoint of the critical temperature transition. Thus, low T_c values of 13.9 K (binary) and 15.3 K (ternary) observed after 4h/675°C (Figure 3.5) show that, although high-T_c A15 is present during the early stages of reaction, the high quality A15 is far overshadowed by the amount of lower-T_c A15.

The superior primary superconducting properties (T_c, H^*_{Kramer} and H_{c2}) observed in the ternary as compared to the binary composite, during the initial stages of Nb_3Sn formation, result from a convolution of faster reaction kinetics and enhanced magnetic field properties for the Ta-doped ternary. Figure 2.5, Figure 2.6 and Figure 2.7 show that the formation of Nb_3Sn occurs earlier in the ternary compared to the binary composite and this coincides with the T_c advantage observed in the ternary for reactions less than 64 hours at 675°C (Figure 3.5). Figure 3.15 illustrates that the ternary H^*_{Kramer} and H_{c2} advantage exists over a complete range of reactions. While Ta additions do improve magnetic field properties in Nb_3Sn [26], the enhanced reaction kinetics must be attributed to a further difference between the two wires other than the ternary addition, since Ta has been found not to have an effect on the Nb_3Sn growth kinetics [54]. Potential differences, such as higher Sn concentration in the core, can only be hypothesized, as only limited compositional measurements were performed in observance of the proprietary status of the strands.

5.2 Effect of A15 Reaction on Primary Superconducting Properties

As in the study of T_c and the Sn gradient by Hawes et al. [33], the primary superconducting properties (T_c, H* and H_{c2}) improve markedly by extending the Nb_3Sn reaction towards completion so that the filaments become more compositionally uniform. For reactions at 675°C, all three properties increased monotonically through at least 128 hours of reaction. Furthermore, as reaction temperature was increased to 750°C, increases in T_c, H* and H_{c2}, compared to the maximum values obtained at 675°C, were observed in both composites. The most remarkable was the 26.7 T (4.2 K) H^*_{Kramer} measurement, obtained in the ternary composite after 32h/750°C, a value not until now reported in multifilamentary conductors [16,36,55]. Increases in the primary superconducting properties were not observed for heat treatments performed at 800°C and greater.

The increase in compositional homogeneity with increasing reaction is perhaps best illustrated by the relationship between H_{c2} and H^*_{Kramer}. As discussed earlier, due to the nature of the magnetization measurement, H_{c2} values are representative of only the highest H_{c2} A15 material while H^*_{Kramer} values average in a less understandable manner the A15 of the whole filament. Thus, as the compositional homogeneity across the thickness of a filament increases, so too does the ratio of H^*_{Kramer} to H_{c2} (Figure 3.15). For reactions of 4h/675°C and 47h/675°C, H^*_{Kramer} : H_{c2} increases from 0.5 to 0.7 in the binary and from 0.6 to 0.8 in the ternary.

For longer reaction times, greater than 312 hours at 675°C, marginal declines were measured in the primary superconducting properties. These declines coincide with the onset of Sn poisoning of the Cu matrix (Figure 5.1). Sn poisoning of the Cu occurs when localized regions of the entire thickness of the Nb tube are converted to A15, bringing the A15 into

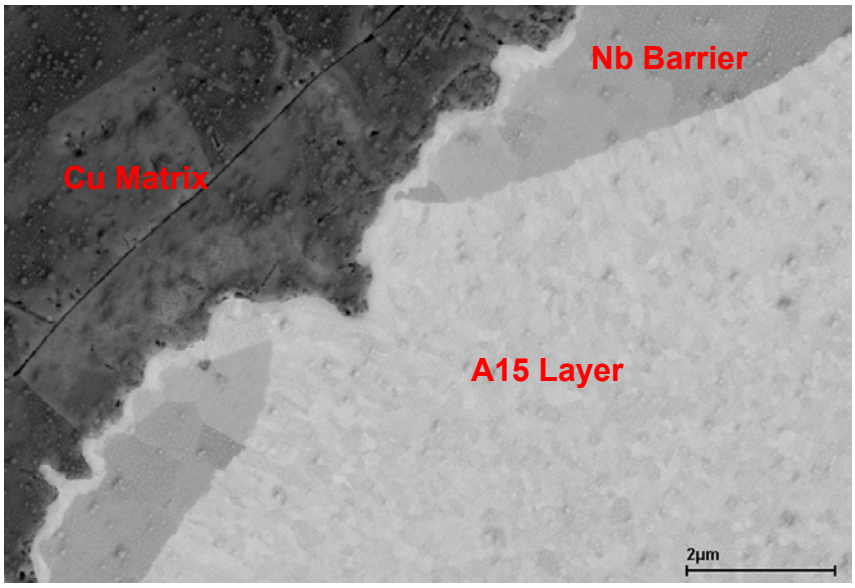

Figure 5.1. Backscatter FESEM micrograph of the ternary composite after 512h/675°C. The image shows over reaction of the Nb barrier resulting in Sn poisoning of the Cu matrix. A15 formation can be seen on the external side of the Nb barrier.

contact with the Cu. This reduces the effectiveness of Cu as a stabilizer, and should also deplete the A15 layer of Sn, thus reducing T_c, H* and H_{c2}. While suppression of the primary properties was observed for the longer reaction times at 675°C, Sn poisoning of the Cu was also observed in the 32h/750°C binary reaction, yet H^*_{Kramer} measured 25.9 T, the highest value observed in this study for the binary strand. Perhaps Sn can be fed into the A15 layer from the core in such a way that the primary filament properties improve, even as it is leaking into and poisoning the Cu on the far side of the diffusion barrier. Composition measurements are needed to better understand the effect that Sn poisoning of the Cu matrix has on the Sn composition gradient in the A15 layer.

5.3 The Compromise Between Primary Properties and Flux Pinning

Similar to the trend observed with the primary superconducting properties, for reactions at 675°C, non-Cu J_c and A15-layer J_c (derived from magnetization) increase monotonically

with reaction time through 128 hours (Figure 4.4 and Figure 4.7), with the only exception being the A15-layer J_c in the ternary strand, which maximizes at 64 hours. However, while the best primary superconducting values are realized for heat treatments performed at 750°C, this higher temperature produces significant declines in J_c. Non-Cu and A15-layer J_c (12 T, 4.2 K), after a reaction of 32h/750°C, fell ~25% in the binary composite and ~40% in the ternary composite from the maximum values achieved at 675°C. This result illustrates the compromise that must be considered when optimizing Nb_3Sn, namely that it is not yet possible to simultaneously optimize the primary properties of $T_c \propto H_{c2}$ and J_c when J_c depends on having a sub-200 nm grain size. This compromise has been observed many times, for example by Marken et al. [45], when employing heat treatments above 750°C in order to drive the reaction of excess-Sn bronze composite to complete stoichiometric conversion of the A15 layer. As in this study, such heat treatments did succeed in raising T_c, H* and H_{c2} but also so increased the grain size that the flux pinning properties of the Nb_3Sn layer were strongly reduced. The grain size of the Nb_3Sn layer for both composites in this study increased by greater than 70% from the J_c maximizing heat treatments performed at 675°C (~150 nm) to the 32h/750°C (~260 nm) reaction. The relationship observed between flux pinning and grain size in this study agrees remarkably well with data from previous Nb_3Sn studies [56]. This comparison is shown in Appendix D.

As seen with the primary superconducting properties, slight declines in A15-layer and non-Cu J_c were observed for reaction times longer than 128 hours at 675°C, coinciding with Sn leakage into the Cu matrix. However, increases in grain size for the binary (~20%) and ternary (~5%) were observed for reactions of 128 hours through 768 hours at 675°C. It is

unclear whether the decrease in J_c is primarily due to the increase in grain size, the potential loss of Sn content in the A15 layer, or a convolution of both.

In an effort to measure the effective pinning force of a grain boundary, elementary pinning force (Q_{GB}) values were calculated for various reactions in this study (Figure 4.18). For the binary and ternary strand reacted at 675°C, Q_{GB} (12 T, 4.2 K) increases monotonically through 128 hours and declines by ~5% (binary) and ~15% (ternary) after 768 hours. Additional increases in Q_{GB} of ~35% for reactions at 750°C were observed in both composites compared to the maximum values obtained at 675°C. The initial goal was to correlate Q_{GB} to the Cu composition in the grain boundaries as measured through scanning Auger microscopy (SAM), and investigate whether grain boundary flux pinning changes as a function of grain boundary Cu composition. Compositional measurements proved too difficult with our current SAM system; however, an upgraded system has been acquired and it is hoped that these measurements will be attainable in the future. Without additional compositional information, it is difficult to fully explain the trends observed in the Q_{GB} data.

5.4 Prospects for Improving the Non-Cu J_c

Small advantages in T_c and H* appear to be available in the PIT conductors studied here, as compared to the best, very high-J_c internal-Sn Nb_3Sn conductors. In a recent study by Naus [35] of the best Nb-2 wt.%Ti internal-Sn conductor possessing a non-Cu J_c (12 T, 4.2 K) of 2,900 A/mm², H* was measured as 25.5 T (4.2 K) and midpoint T_c was measured as 16.6 K. By comparison, the 128h/675°C ternary reaction investigated in this study achieved an H* of 25.7 T (4.2 K) and a T_c of 17.1 K; however, non-Cu J_c (12 T, 4.2 K) as measured by transport is believed to be only ~2,290 A/mm² (Table 5.1). Thus, non-Cu J_c in

Table 5.1

Comparison of Properties in PIT and Internal-Sn Conductor

Conductor	Non-Cu J_c (12 T, 4.2 K)	H^*_{Kramer} (4.2 K)	T_c (Midpoint)
Powder-in-Tube Ternary – 128h/675°C	2,300 A/mm² †	25.9 T	17.1 K
Internal-Sn	2,900 A/mm²	25.5 T	16.6 K

† This non-Cu J_c value was increased by a factor of 1.29 from the magnetization value reported in this study (1,780 A/mm²) because the 64h/675°C reaction measured in transport by Barzi et al. [42] obtained 2,160 A/mm² while we measured 1,680 A/mm² via magnetization for the same reaction, as shown in Table 5.2 and discussed in section 4.2. The 128h/675°C ternary reaction was chosen for comparison to the internal-Sn conductor since it achieved the highest non-Cu J_c value.

the PIT conductor appears to be underachieving its true potential as indicated by its almost identical primary superconducting properties when compared to the best internal-Sn conductor.

An important reason why the internal-Sn conductor design achieves a significant advantage in non-Cu J_c is that it contains a higher fraction of A15 within the non-Cu area. Internal-Sn conductors have achieved A15/non-Cu areas of ~60%, whereas these PIT conductors, receiving the manufacturer's recommended heat treatment (64h/675°C), have achieved ~50%. However, since ~20% of the A15 area in the PIT strand is composed of coarse-grained A15, only ~40% of the non-Cu region (80% of the A15 layer) is believed to contribute to J_c (the internal-Sn conductor does not contain a coarse-grained Nb_3Sn region). The remainder of the filament is composed of the $NbSn_2$ + Sn + Cu sleeve core (~25%) and unreacted Nb (~25%).

To properly compare the PIT architecture to the internal-Sn design, we thus pose the question of what would the A15/non-Cu area in the PIT have to be to obtain a non-Cu J_c value of 2,900 A/mm². Table 5.2 shows J_c and filament area values obtained for the 64h/675°C reaction, the highest yielding A15-layer J_c reaction in this study. The non-Cu J_c as measured by transport (non-Cu $J_{c\ (trans.)}$) is 1.29 times greater than the value obtained via

Table 5.2

J_c and filament area in 64h/675°C PIT strand. Magnetization values are as measured in this thesis, while the transport value was measured by Barzi et al. [42]. The disparity between the magnetization and transport measurement is explained in section 4.2. The transport value is believed to be more accurate than the magnetization value.

Critical Current Density (A/mm²)			Filament Area (μm²)	
$Layer_{mag.}$	$Non\text{-}Cu_{mag.}$	$Non\text{-}Cu_{trans.}$	Fine-Grained A15-Layer	Non-Cu
4,280	1,680	2,160 [42]	935	2,380

magnetization (non-Cu $J_{c\ (mag.)}$). Assuming that this proportionality, arising from the non-radial symmetry of the A15 layers, is correct, the fine-grain layer $J_{c\ (trans.)}$ is

$$fine-grain\ layer\ J_{c\ (trans.)} = \frac{non-Cu\ J_{c\ (trans.)} \cdot non-Cu\ Area}{fine-grain\ A15\ Area} = 5{,}500\ A/mm^2 . \quad (5.1)$$

Assuming that the A15-layer $J_{c\ (trans.)}$ value does not diminish with increasing fine-grain A15 fraction, the fine-grain A15 area required to obtain a transport J_c of 2,900 A/mm² can be calculated as follows:

$$required\ A15\ Area = \left(\frac{non-Cu\ J_{c\ (trans.)} \cdot non-Cu\ Area}{fine-grain\ layer\ J_{c\ (trans.)}} \right) = 1{,}260 \mu m^2 . \quad (5.2)$$

Therefore, the A15/non-Cu area required to obtain a transport non-Cu J_c of 2,900 A/mm² is

$$A15/non-Cu\ Area = \left(\frac{required\ A15\ Area}{non-Cu\ Area} \right) = \left(\frac{1{,}260 \mu m^2}{2{,}380 \mu m^2} \right) = 53\% . \quad (5.3)$$

There does appear to be an adequate supply of Sn and unreacted Nb in the present compositions to facilitate the increase in A15/non-Cu from 40% to 53%; however, over reaction of the Nb barrier occurs when the fine-grain A15 layer exceeds 45% of the total filament area. Therefore, assuming 25% of the filament area is composed of $NbSn_2$ + Sn + Cu sleeve core and 10% is composed of large-grain A15, >20% of the non-Cu area must be composed of unreacted Nb to prevent barrier breakthrough of the hexagonal filaments.

A few potential solutions exist for improving the A15/non-Cu area in the PIT conductor in an effort to enhance non-Cu J_c. One is to replace hexagonal Nb filament tubes with circular ones. This would allow for a greater percentage of the Nb tube to be reacted prior to Sn breakthrough and thus make more efficient use of the unreacted Nb as a diffusion barrier. Since the A15 layer is circular, the hexagonal configuration always results in excess unreacted Nb, which does little for barrier breakthrough protection. Another solution would be to reduce the filament core size by increasing the radial thickness of the tube and providing more area for A15 reaction. The drawback of a smaller core is that the Sn composition in the core may have to be increased in order to avoid lowering the Sn content of the A15. Lindenhovius [57] has also observed that wire drawing becomes increasingly difficult as free Sn in the core is increased. An additional complication is that the present work (section 2.3) shows that the connection which permits diffusing Sn to pass between the core and the A15 layer is interrupted near the outer regions of the core, immediately to the inside of the large-grain Nb_3Sn layer where void space appears to be present (Figure 2.5 and Figure 2.6). Significant Sn is left behind even after substantial reaction, as shown by energy dispersive spectroscopy (EDS) on the ternary strand reaction of 64h/675°C, for which measurements of 5.7at.%Sn and 2.9at.%Sn were obtained in the core center and in the outer most regions of the core, respectively. The significant residual Sn content of the core suggests how important it is to maintain Sn diffusion paths between the core and the Nb_3Sn layer. If this could be done, it probably would not be necessary to increase the Sn content in the core if the core size is reduced. The ramifications of circular filaments and smaller cores are currently being investigated as a means to enhance the cabling properties of the PIT

strand [57]; however, it appears that the changes, if successful, would have the combined effect of improving non-Cu J_c as well.

6 Conclusion

A large spectrum of Nb_3Sn reactions were performed on pure and tantalum-doped niobium, Nb_3Sn PIT conductors in order to understand the relationships between microstructure, superconducting properties and flux pinning in the A15 phase. High-Sn content Nb_3Sn formation occurs very rapidly in binary and ternary PIT composites as evidenced by high H_{c2} values (>11 T at 12 K) observed at 4h/675°C. As the Nb_3Sn reaction is extended towards completion and compositional uniformity of the A15 layer increases, the primary superconducting properties (T_c, H* and H_{c2}) improve markedly. All three properties increased monotonically through at least 128 hours of reaction at 675°C, and additional benefits in T_c, H* and H_{c2} were observed for 750°C reactions. The most significant of these was the 26.7 T (4.2 K) H^*_{Kramer} measurement, obtained in the ternary composite after 32h/750°C. J_c also increases monotonically with reaction through 128 hours at 675°C, however significant declines (~25% in binary and ~40% in ternary) are observed when reaction temperature is increased to 750°C. Thus, it is not yet possible to simultaneously optimize the primary properties and flux pinning in PIT conductors when high J_c demands grains of order 200 nm or less. Correlations between over-reaction of the Nb barrier, resulting in Sn-poisoning of the Cu matrix, and diminished H^*_{Kramer}, H_{c2} and flux pinning properties for reaction times longer than 128h/675°C were observed. Additional compositional measurements of the A15 layer are needed to better understand the effect that Sn leakage has on A15 layer composition and to fully understand the trends observed in the

elementary pinning force data. Similar primary superconducting properties were observed in the PIT conductor studied here, as compared to the best, very high-J_c internal-Sn Nb_3Sn conductors. The significantly lower non-Cu J_c measured in the PIT is primarily attributed to the lower fraction of A15 within the non-Cu area. While the necessary increase in A15/non-Cu area required to produce a similar non-Cu J_c is not attainable in the current PIT design, significant enhancements in non-Cu J_c may result from circular Nb tubes and a smaller core size. The ramifications of these changes are currently being investigated.

7 References

1. R. M. Scanlan, D. R. Dietderich and H. C. Higley, "Conductor Development for High Field Dipole Magnets," *IEEE Trans. Appl. Supercond*., **10** (1), pp. 288-293 (2000).
2. R. A. Lundy, "State of the Energy Doubler," *IEEE Trans. Mag.*, **MAG-17** pp. 709-712, (1981).
3. R. Mienke, "Superconducting Magnet System for HERA," *IEEE Trans. Mag.*, **MAG-27** pp. 1728-1734, (1991).
4. R. Perin, "The Superconducting Magnet System for the LHC," *IEEE Trans. Mag.*, **MAG-27** pp. 1735-1742, (1991).
5. L. D. Cooley, P. J. Lee and D. C. Larbalestier, IOP Handbook Review, submitted for publication.
6. H. Hillmann and K. J. Best, "New Measurements of Critical Data of Optimized NbTi Superconductors," *IEEE Trans. Mag.*, **MAG-13** pp. 1568-1570, (1977).
7. J. A. Parrell, Low Temperature Superconducting Workshop, Napa, CA (2001).
8. A.C. Rose-Innes and E.H. Rhoderick, Introduction to Superconductivity, Pergamon Press, Oxford (1978).
9. J. E. Kunzler, E. Buehler, L. Hsu & J. Wernick, "Superconductivity in Nb_3Sn at High Current Density in a Magnetic Field of 88 KGauss. *Phys. Rev. Letts.*, **6**, pp. 89-91 (1961).
10. W.H. Warnes, "Principles of Superconductivity," ASM International Metals Handbook Vol. 2, 10^{th} ed., pp.1030-1042, 1990.
11. D. B. Smathers, "A15 Superconductors," *Metals Handbook*, 10^{th} ed., **2**, American Society for Metals, 1060-1076 (1990).
12. B. T. Matthias, "Superconductivity and Valence Electrons/Atom" Phys. Rev., **97**, pp. 74-76 (1955).
13. A. M. Clogsten and V. Jaccarino, Phys. Rev., **121**, pp. 1357-1362 (1961).
14. J. P. Charlesworth, I. Macphail and P. E. Madsen, "Experimental Work on the Niobium-Tin Constitution Diagram and Related Studies," *J. Mat. Sci.*, **5**, pp. 580-603 (1970).
15. R. Mailfert, B. W. Batterman and J. J. Hanak, Phys. Lett., **24A**, pp. 315-316 (1967).
16. H. Devantay, J. L. Jorda, M. Decroux, J. Muller and R. Flukiger, "The Physical and Structural Properties of Superconducting A15-type Nb-Sn Alloys," *J. Mat. Sci*, **16**, pp. 2145-2153 (1981).
17. J. Ekin, "Strain Effects in Superconducting Compounds," *Adv. Cryo. Eng.*, **30**, pp. 823-836 (1984).
18. D. O. Welch, "Alteration of Superconducting Properties of A15 Compounds and Elementary Composite Superconductors by Nonhydrostatic Elastic Strain," *Adv. Cryo. Eng.*, **26**, pp. 48-65, (1980).
19. R. Flukiger, R. Isernhagen, W. Goldacker and W. Specking, "Long-Range Atomic Order, Crstallographical Changes and Strain Sensitivity of J_c in Wires Based on Nb_3Sn and Other A15 Compounds," *Adv. Cryo. Eng.,* **30**, pp. 851-858, (1984).

20. R. M. Scanlan, W. A. Feitz and E. F. Koch, "Flux Pinning Centers in Superconducting Nb_3Sn," *J. Appl. Phys.*, **46** (5), pp. 2244-2249 (1974).
21. M. Suenaga, in Superconductor Materials Science-Metallurgy, Fabrication and Applications, S. Foner and B. Schwartz, Ed., Plenum Press, pp. 201-274 (1980).
22. S. Ochiai and L. Osamura, "Influence of Grain Size and Upper Critical Field on Global Pinning Force of Bronze-Processed Nb_3Sn Compound," Acta Metall. **34** (12), pp. 2425-2433, (1986).
23. C.E. Bruzek, P. Sulten, E. Sirot, C. Kohler, P. Mocaer, F. Peltier and G. Grunblatt, "Effect of Heat Treatments on Superconducting Properties of Nb_3Sn Strands Developed at GEC ALSTHOM," *IEEE Trans. Appl. Supercond.*, **7** (2), pp. 1041-1044 (2001).
24. H. Sekine, Y. Iijima, K. Itoh and K. Tachikawa, "Improvements in Current-Carrying of Nb_3Sn Composites in High Fields Through Titanium Addition to the Matrix," *IEEE Trans. Mag.,* **19** (3), pp. 1429-1432, (1983).
25. K. Togano, T. Asano and T. Takeuchi, "Effects of Mg Additon to the Cu-Sn Matrix In the Composite Processed Nb_3Sn with Nb-Ti Alloy Cores," *J. Less-Common Met.*, **68** pp. 15-22, (1979).
26. M. Suenaga, D. O. Welch, R. L. Sabatini, O. F. Kammerer and S. Okuda, "Superconducting Critical Temperatures, Critical Magnet Fields, Lattice Parameters, and Chemical Compositions of "Bulk" Pure and Alloyed Nb_3Sn Produced by the Bronze Process," *J. Appl. Phys.,* **59** (3), pp. 840-853, (1986).
27. S. Foner, E. J. McNiff, G. M. Ozeryansky and R. E. Schwall, "High Field Properties of Multifilamentary $(Nb\text{-}4at\%Ta)_3Sn$," *IEEE Trans. Mag.,* **23** (2) pp. 984-987, (1983).
28. S. Gauss and R. Flukiger, "Powder Metallurgical Alternative for the Processing of $(Nb\text{-}Ta)_3Sn$ Multifilamentary Wires, Starting From Elementary Nb and Ta Powder," *IEEE Trans. Mag.,* **23** (2), pp. 657-660, (1987).
29. I. W. Wu, D. R. Dietderich, J. T. Holthuis, W. V. Hassenzahl and J. W. Morris, Jr., "The Influence of Magnesium Addition to the Bronze on the Critical Current of Bronze-Processed Multifilamentary Nb_3Sn Conductors," *IEEE Trans. Mag.,* **19** (3), pp. 1437-1440, (1983).
30. G. LeFranc and A. Müller, "Effect of Copper Additions to Superconducting Niobium-Tin Sinter Material," ," *J. Less-Common Met.*, **45** pp. 339-342, (1976).
31. J. D. Livingston, "Grain Size in A-15 Reaction Layers," *Phys. Stat. Sol. A*, **44**, pp. 295-301 (1977).
32. M. Suenaga and W. Jansen, "Chemical Compositions at and Near the Grain Boundaries in Bronze-Processed Superconducting Nb_3Sn," *Appl. Phys. Lett.* **43** (8), pp. 791-793 (1983).
33. C. D. Hawes, "Investigations of the Inhomogeneity of a Powder-In-Tube Nb_3Sn Conductor," Masters Thesis, University of Wisconsin-Madison (2000).
34. A. R. Kaufman and J. J. Picket, "Multifilament Superconducting Wire," *Bull. Am. Phys. Soc.*, **15** pp. 838 (1970).
35. M. T. Naus, "Characterization of Nb_3Sn Internal-Sn Composites," PhD. Thesis, University of Wisconsin-Madison (2002).

36. V. Abacherli, B. Seeber, E. Walker, and R. Flukiger, "Development of (Nb, Ta)$_3$Sn Multifilamentary Superconductors Using Osprey Bronze With High Tin Content," *IEEE Trans. Appl. Supercond*., **11** (1), pp. 3667-3670 (2001).
37. M. Field, R. Hentges, J. Parrell, Y. Zhang and S. Hong, "Progess with Nb_3Sn Conductors at Oxford Instruments, Superconducting Technology," *IEEE Trans. Appl. Supercond*., **11** (1), pp. 3692-3693 (2001).
38. A. Vorobieva, A. Shikov, A. Silaev, E. Dergunova, V. Lomaev, M. Nasibulin, K. Mareev and S. Kuznetsov, "Study of Nb_3Sn with Enhanced Characteristics for ITER," *IEEE Trans. Appl. Supercond*., **11** (1), pp. 3588-3590 (2001).
39. Y. Hashimoto, K. Yoshizaki and M. Tanaka, "Processing and Properties of Superconducting Nb_3Sn Filamentary Wires," *Proc. Of the 5th International Cryogenic Engineering Conference*, Kyoto, Japan pp. 332-335 (1974).
40. J. C. McKinnell, R. Hentges, J. Tatu., Y. Z. Zhang and S. Hong, "Fully Bonded Internal-Tin, Niobium-Tin (Nb_3Sn) Conductor Development at Oxford Superconducting Technology," *IEEE Trans. Appl. Supercond*., **7** (2), pp. 1360-1363 (2001).
41. W. K. McDonald, C. W. Curtis, R. M. Scanlan, D. C. Larbalestier, K. Marken and D. B. Smathers, "Manufacture and Evaluation of Nb_3Sn Conductors Fabricated By the MJR Method," *IEEE Trans. Mag*., **MAG-19** (3), pp. 1124-1127 (1983).
42. E. Barzi, P. J. Limon, R. Yamada and A. V. Zlobin, "Study of Nb_3Sn Strands for Fermilab's High Field Dipole Models," *IEEE Trans. Appl. Supercond*., **11** (1) pp. 3595-3598 (2001).
43. E. M. Hornsveld, J. D. Elen, C. A. M. van Beijnen and P. Hoogendam, "Development of ECN-Type Niobium-Tin Wire," in *Adv. Cryo. Eng.*, **34** pp. 493-498 (1987).
44. H. Ten Kate, H. Weijers, and J. van Oort, "Critical Current Degredation in Nb_3Sn cables Under Transverse Pressure," *IEEE Trans. Appl. Supercond*., **3** (1), pp.1334-1337 (1993).
45. K. R. Marken, S. J. Kwon, P. J. Lee and D. C. Larbalestier, "Characterization Studies of Fully Reacted High Bronze-to-Niobium Ratio Filamentary Nb_3Sn Composite," *Adv. Cryo. Eng.*, **32** pp. 967-975 (1986).
46. T. Wong and C. V. Renaud, "Ti and Ta Additons to Nb_3Sn by the Powder in Tube Process," *IEEE Trans. Appl. Super*., **11** (1), pp.3584-3587 (2001).
47. P. J. Lee and D. C. Larbalestier, "Compositional and Microstructural Profiles across Nb_3Sn Filaments Produced by Different Fabrication Methods," *IEEE Trans. Appl. Supercond*., **11** (1), pp. 3671-3674 (2001).
48. E. J. Kramer, "Scaling Laws for Flux Pinning in Hard Superconductors," *J. Appl. Phys.,* **44** (3), pp. 1360-1370 (1973).
49. C. M. Fischer, P. J. Lee and D. C. Larbalestier, "Irreversibility Field and Critical Current Density as a Function of Heat Treatment Time and Temperature for a Pure Niobium Powder-in-Tube Nb_3Sn Conductor," *Adv. Cryo. Eng.*, **48B** pp. 1008-1015 (2002).
50. M. Suenaga, A. K. Ghosh, Y. Xu and D. O. Welch, "Irreversibility Temperatures of Nb_3Sn and NbTi," *Phys. Rev. Lett*, **66** (13), pp. 1777-1780 (1991).

51. R. R. Hake, “Paramagnetic Superconductivity in Extreme Type-II Superconductors,” *Phys. Rev.*, **158** (2) pp. 356-376 (1967).
52. J. E. Evetts and P. H. Kes, Magnetic and Superconducting Materials, pp. 95-102 (1992).
53. H. Veringa, P. Hoogendam and A. C. A. van Wees, “Growth Kinetics and Characterization of Superconducting Properties of Multifilament Materials Made by the ECN Powder Method,” *IEEE Trans. Magnetics*, **19** (3), pp. 773 –776 (1983).
54. J. D. Livingston, “Effect of Ta Additions to Bronze-Processed Nb_3Sn Superconductors,” *IEEE Trans. Mag.*, **MAG-14** (5), pp. 611-613 (1978).
55. T. Miyazaki, Y. Murakami, T. Hase, M. Shimada, K. Itoh, T. Kiyoshi, T. Takeuchi K. Inoue and H. Wada, “Development of Nb_3Sn Superconductors for a 1 GHz NMR Magnet,” *IEEE Trans. Appl. Supercond.*, **9** (2), pp. 2505-2508 (1999).
56. L. A. Bonney, T. C. Willis and D. C. Larbalestier “Dependence of Critical Current Density on Microstructure in the $SnMo_6S_8$ Chevrel Phase Superconductor,” *J. Appl. Phys.*, **77** (12), pp. 6377-6387 (1995).
57. Personal communication, Jan H. Lindenhovius, ShapeMetal Innovations, Holland.

Appendix A – Image Analysis of PIT Filament Dimensions

Various regions of PIT filaments were characterized through computer image analysis of backscattered SEM images. A typical PIT filament is illustrated in Figure A.1. For each heat treatment reaction, approximately five filaments were analyzed. The regions of primary interest were the small-grain A15 layer and the unreacted Nb. As a result, 3 interfaces were identified; the interface between the Cu and Nb layers, the interface between the Nb and the small-grain A15 layers and the interface between the small-grain A15 and the large-grain

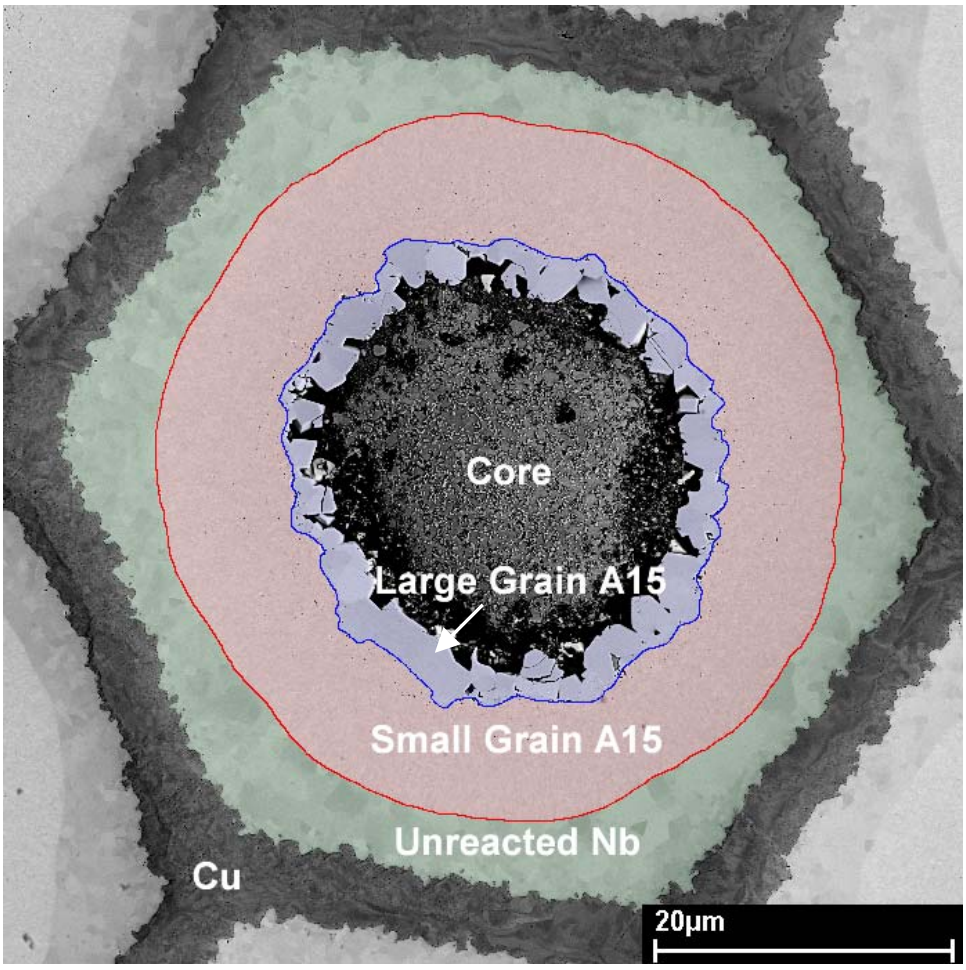

Figure A.1. The various regions of a PIT filament that were identified through image analysis. These regions were the unreacted Nb (green), the small-grain A15 (red) and the large-grain A15 (purple). The image in this figure was artificially colored to depict the various regions more clearly.

A15 layers. The image contrast between the unreacted Nb and the stabilizing Cu was great enough such that the Cu-Nb interface could be identified through image thresholding in the computer software. The interfaces marking the inner and outer boundaries of the A15 layer had to be identified visually and traced manually with a mouse as image contrast was not suitable for thresholding. The cross-sectional areas of the Nb and small-grain A15 layers were calculated from these interfaces. The 3 interfaces are essentially concentric circles and their effective circular radii were used to characterize their position relative to the center of the filament core. These radial dimensions were used in calculating J_c; the method for which is discussed in section 4.1.

Appendix B – Kramer Extrapolations on Ternary Strand Reacted at Elevated Reaction Temperatures

Table B.1

Two-Step, Elevated Temperature Reactions

850°C	16h/750°C + 24h/850°C
900°C	16h/750°C + 24h/900°C
950°C	16h/750°C + 24h/950°C
1000°C	16h/750°C + 24h/1000°C

B = Binary
T = Ternary

Two-step, elevated temperature reactions were performed to facilitate heat treatments at temperatures greater than 850°C without causing melting of the tube constituents. The initial, lower temperature reaction at 750°C was instituted to transform the $NbSn_2$ powder into Nb_6Sn_5 and finally Nb_3Sn prior to the start of the elevated-temperature reaction. $NbSn_2$ and Nb_6Sn_5 have melting points of approximately 850°C and 930°C, respectively. As a result, large amounts of Sn leakage occurred from the ends of the heat treated specimens when the initial, lower temperature reaction was not performed. While noticeable improvements were observed for the two-step reactions, it is unclear whether the heat treatments completely inhibited Sn leakage from the ends of the reacted specimens.

Linearity does not exist in the 4.2 K, Kramer curves measured for the two-step extensive heat treatments, as illustrated in Figure B.1, and thus H^*_{Kramer} is not valid for these reactions. It can be seen from the figure that as reaction temperature increases, the worse the Kramer function fits the data. The hysteretic loops (not shown) for all the reactions in Figure B.1 clearly prove that H* is greater than 14 T, as hysteretic loop closure does not exist below 14 T. However, this is not clearly evident from the Kramer curves, which appear to point to H^*_{Kramer} values <14 T.

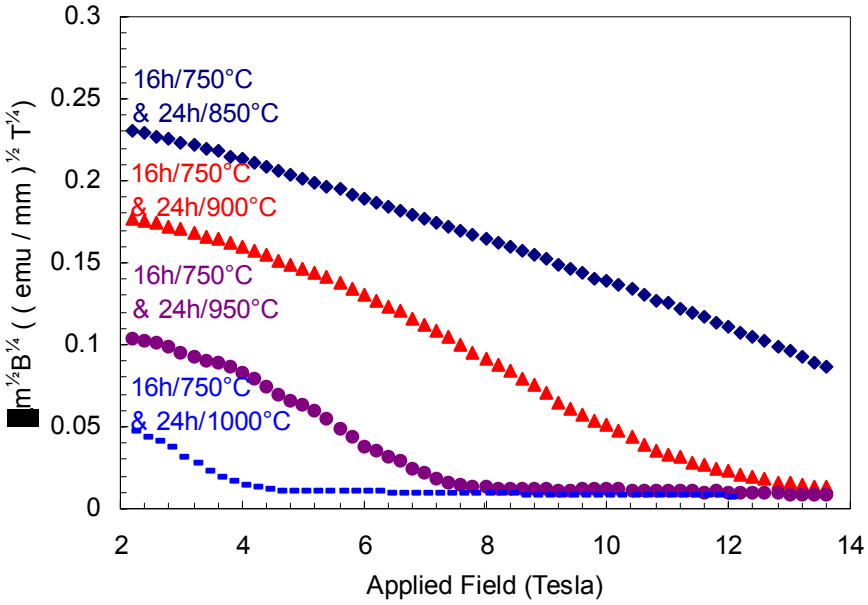

Figure B.1 Kramer plots, derived from magnetization curves of the ternary wire measured at 4.2K, for the two-step elevated heat treatments. For each reaction, the initial heat treatment is 16h/750°C followed by a 24 hour reaction at temperatures ranging from 850 to 1000°C. The magnetic moments are normalized to sample length. As heat treatment temperature is increased, the worse the Kramer function fits the data. It is known from the hysteretic loops that H* is greater than 14 T for all of the reactions, as loop closure doesn't occur prior to 14 T; however H^*_{Kramer} values greater than 14 T are not clearly evident from the Kramer extrapolations.

Despite the poor Kramer fits to the two-step extensive heat treatments, it is evident from magnetization measurements performed at 12 K that the irreversibility fields in these samples are not as high as those measured in the 750°C heat treatments. The hysteretic loop closures for two-step, extensive heat treatment ternary reactions (Table B.1) are significantly lower than those measured for reactions at 750°C, or even the longer heat treatment times at 675°C (Table 3.2). Thus, the two-step reactions exhibit marked declines in H*.

Table B.2

H^*_{LC} (12 K) for Two-Step, Extensive Heat Treatments in Ternary Strand

Two-Step Heat Treatment	H^*_{LC} (Tesla)
16h/750°C & 24h/850°C	9.7
16h/750°C & 24h/900°C	8.8
16h/750°C & 24h/950°C	6.1
16h/750°C & 24h/1000°C	7.0

Appendix C – Voltage Criterion for Magnetization Derived J_c

An important parameter in critical current measurements is the voltage criterion, which characterizes the dissipation threshold that defines the critical state. A typical voltage criterion used in transport measurements for Nb_3Sn is 10 μV/m. The voltage criterion for the magnetization derived critical current is a function of the magnetometer ramp rate as illustrated by the following equations. The ramp rate employed for the magnetization measurements in this study was 0.6 T/min.

$$\frac{dB}{dT} = 0.6\frac{T}{\min} = 10\frac{mT}{\sec} \tag{C.1}$$

$$\frac{V}{m} = \frac{N}{C} \tag{C.2}$$

Combining Eq. C.1 and Eq. C.2 yields

$$\frac{T}{\sec} = \frac{N}{A \cdot m} = \frac{V}{m^2}. \tag{C.3}$$

Since the PIT samples were oriented parallel to the applied magnetic field, circulating currents flowed circumferentially within the Nb_3Sn layers of each filament. Therefore the length of the path of circulating current can be approximated as the average circumference of the Nb_3Sn layer, which was determined to be ~125 μm. Thus, the voltage criterion employed for the magnetization measurements in this study was,

$$\frac{V}{m} = \left(1 \text{ X } 10^{-2}\frac{T}{\sec}\right) \cdot \left(125 \text{ X } 10^{-6} \ m\right) = 1.25\frac{\mu V}{m}. \tag{C.4}$$

This voltage criterion (1.25 μV/m) is smaller than the typical criterion used in transport measurements (10 μV/m), and from a voltage criterion standpoint the magnetization derived

J_c values are underestimates of transport J_c values. However this understatement is small except close to the irreversibility field. Under most circumstances the V-I response of the conductor can be written as $V \propto I^n$ where n is ~10 at 90% H* and rapidly rises to 50-60 below this.

Appendix D – Comparison of F_p Versus Grain Size Data

It is well established that the pinning force (F_p) in Nb_3Sn is strongly dependent on grain size. F_p versus grain size data observed in this study is compared to data obtained in previous studies, and Figure D.1 and Figure D.2 show that the respective data agree remarkably well.

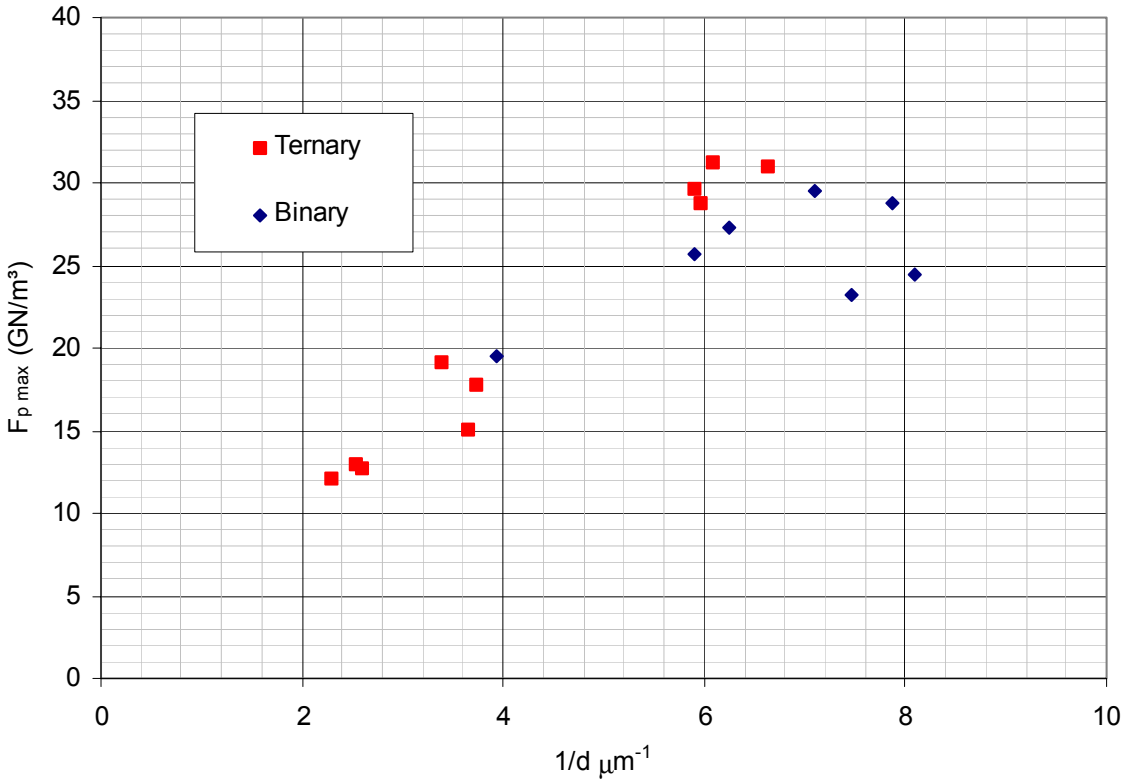

Figure D.1. F_p max (4.2 K) versus grain size for the binary and ternary composites examined in this study. The F_p (J_c x B) data were obtained from non-Cu J_c values, which were derived from magnetization measurements.

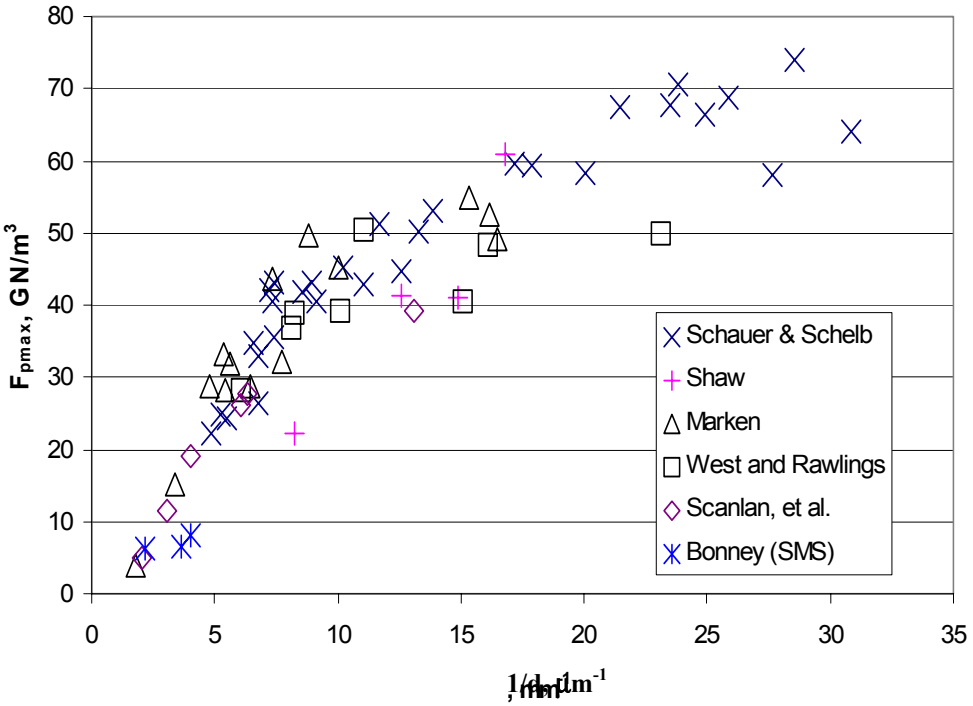

Figure D.2. F_p max (4.2 K) versus grain size for Nb3Sn and SnMo6S8 [56].